Contact Mechanics of Elastic-Plastic Layered Media With Smooth and Rough Surfaces

by

Ning Ye

B.S. (University of Science and Technology of China) 1994
M.S. (Institute of Mechanics, Chinese Academy of Sciences) 1997

A dissertation submitted in partial satisfaction of the

requirements for the degree of

Doctor of Philosophy
in

Engineering–Mechanical Engineering

in the

GRADUATE DIVISION

of the

UNIVERSITY OF CALIFORNIA, BERKELEY

Committee in charge:

Professor Kyriakos Komvopoulos, Chair
Professor David B. Bogy
Professor Robert O. Ritchie

Spring 2002

The dissertation of Ning Ye is approved:

Chair Date

Date

Date

University of California, Berkeley

Spring 2002

Contact Mechanics of Elastic-Plastic Layered Media With Smooth and Rough Surfaces

Copyright 2002

by

Ning Ye

Abstract

Contact Mechanics of Elastic-Plastic Layered Media With Smooth and Rough Surfaces

by

Ning Ye

Doctor of Philosophy in Engineering–Mechanical Engineering

University of California, Berkeley

Professor Kyriakos Komvopoulos, Chair

A contact mechanics analysis of elastic-plastic layered media was performed to study contact between rough surfaces, thermal-mechanical sliding contact, sliding on layered media with surface layers under residual stress, and valid hardness measurement of layered media. The work included both analytical and finite element studies.

Using a finite element model of a rigid sphere in normal contact with a semi-infinite elastic-plastic homogeneous medium, constitutive relations were obtained for the mean contact pressure and real contact area in terms of representative strain. This contact model was extended to layered media by modifying the constitutive equation of the homogeneous medium to include the effects of the mechanical properties of the layer and substrate materials and the layer thickness. Insight was obtained about the evolution of elastic, elastic-plastic, and fully-plastic deformation at the rough contact interface in terms of the maximum local surface interference, and the dependence of the contact load and real contact area of rough surfaces on fractal parameters and the layer thickness.

An elastic-plastic contact analysis, based on a finite element model and real surface topographies, was performed to elucidate deformation at the head-disk interface. The study illustrated the significance of the thickness, mechanical properties, and residual stress of the layer on the development of plasticity and likelihood of cracking in the layer and the substrate media.

The coupled effects of surface mechanical and thermal (frictional) loadings on the deformation of layered media were examined using a three-dimensional finite model of an elastic sphere sliding over an elastic-plastic layered medium. Friction traction and thermal loading were shown to enhance stress intensification and plasticity, especially in the case of relatively thin layers of low thermal conductivity.

Moreover, a three-dimensional finite element model was developed to simulate a rigid spherical asperity indenting and sliding on an elastic-plastic layered medium exhibiting varying magnitudes of residual stress in the top layer for two different coefficients of friction. The optimal residual stress to minimize the possibility of yielding and cracking was shown to be between zero and –0.5 times the peak contact pressure, the exact value depending on the type of contact (normal or sliding), coefficient of friction, and deformation mode of the layer.

Hardness of elastic-plastic layered media was evaluated in the context of finite element simulation results. The critical interference distance, below which substrate effects can be neglected, was determined by considering the variation of the equivalent hardness with the interference distance. The minimum interference distance, above which the occurrence of sufficient plasticity leads to the determination of the real hardness of the material, was determined from the contact constitutive model mentioned earlier and a

relation between hardness, yield strength, and elastic modulus for a homogeneous half-space. A new scheme of hardness measurement for thin-film media was proposed and validated by finite element simulation results for an elastic-perfectly plastic layered medium.

The findings of this dissertation provide new information about the effect of surface topography, thermal loading, friction traction, and thickness, mechanical properties, and residual stress of the top layer on the deformation behavior of layered media. The results are of particular relevance to thin-film media and interface topographies used in computer hard disk drives. However, most of the analytical and finite element models can be extended to other type of contact interfaces with slight modifications.

Professor Kyriakos Komvopoulos

Dissertation Chair

TABLE OF CONTENTS

LIST OF FIGURES

Chapter 2

Chapter 3

Chapter 4

Chapter 5

Chapter 6

ACKNOWLEDGEMENTS

My most sincere gratefulness goes to my research advisor, Professor Kyriakos Komvopoulos, for his encouragement, guidance, enthusiasm, moral and intellectual support, without which this dissertation is never possible. I will benefit from what I have learned from him throughout my career.

I greatly appreciate Professor David B. Bogy and Professor Robert O. Ritchie for serving on my dissertation committee; Professor C. K. Hari Dharan, Professor Robert O. Ritchie, Professor George C. Johnson, and Professor Lisa A. Pruitt for serving on my qualifying exam committee. Their invaluable help has made my academic progress at Berkeley much smoother. I am grateful to Professor Panayiotis Papadopoulos, Professor George C. Johnson, and Professor David J. Steigmann for their help on my initial financial support at Berkeley.

I would also like to thank my fellow students in the lab, Dr. Wentao Yan, Dr. Wei Lu, Dujiang Wan, Zhong-Qing Gong, Jian Yang, Rui Xu, Phil Mai, and Sophia Kim, who have offered their friendship and insightful discussion on research or course work.

This dissertation is dedicated to my family. I truly hope that this is my first step to fulfill the wishes of my parents, sister and parents-in-law. I feel deeply indebted to my wife Shiying for her patience, support, and love.

This dissertation research was supported by the Surface Engineering and Tribology Program of the National Science Foundation, National Storage Industry Consortium (NSIC) Extremely High Density Recording (EHDR) Program, and Computer Mechanics Laboratory at the University of California, Berkeley.

CHAPTER 1

INTRODUCTION

Contact mechanics, an essential part of solid mechanics, deals with the stresses and deformation within two bodies loaded together. It is a powerful tool for investigation of basic problems in tribology, which is the science of the mechanisms of friction, lubrication, and wear of interacting surfaces that are in relative motion. The history of contact mechanics dates back to Hertz (1882), when he started working on the problem of elastic contact. Within the last century, contact mechanics has grown together with the modern industry. Its application can be found in many icons of the modern civilization, railways, automobile, and all engineering machineries having components with interacting surfaces such as gears, bearings or cams. The contact stresses between interacting bodies are often high and may cause failure either by yielding, fracture, or contact fatigue. When a load is applied to two contacting bodies, the contact area usually increases, and friction force often arises to resist relative motion. Therefore, contact problems are typically nonlinear. To enhance the tribological performance of many engineering components, hard overcoats have been widely used as a protective layer. The presence of a surface layer strongly affects the stress/strain fields and makes them differ from those of homogeneous media. Contact problems in layered media are much more difficult to analyze than in homogeneous media and oftentimes exact analytical solutions are not possible, especially for elastic-plastic materials. The importance of contact mechanics of layered media in engineering applications and its complicated nature have drawn great interest from both engineers and scientists.

One well-known fact is that engineering surfaces are rough. Traditional approaches to characterize rough surfaces using statistical parameters possess the drawbacks associated with scale dependent parameters and non-uniqueness. However, most engineering surfaces exhibit random and multi-scale surface topography features. This requires using fractal geometry, which can provide scale independent description of rough surfaces. When two rough surfaces are loaded together, the load is distributed among multiple contacting asperities. Understanding the mutual relationship of load, real contact area, subsurface stress/strain field, and surface topography is important in many engineering applications, such as computer hard disk drives and microelectromechanical systems.

When two surfaces slide against each other, mechanical energy is dissipated as frictional heat. Many failures are caused by the combined effects of thermal and mechanical traction at sliding interfaces of components used in a wide range of engineering applications, such as face seals, bearings, automotive brake systems, electric motor brushes, computer head-disk interface, and electrical switches. Oftentimes, the thermal and mechanical tractions are coupled; hence, the temperature and stress fields cannot be determined independently. This is one of the most challenging types of problems in contact mechanics.

Numerous experimental studies have shown the existence of residual stresses in components stemming from the manufacturing process used to fabricate many engineering applications, such as thermal quenching, shot peening, ion implantation, and energetic particle bombardment during film growth. Since residual stresses can be close to the yield strength of surface layer material, to ensure the reliability of thin films it is

critical to fully understand the effect of residual stresses on subsurface stress/strain filed during normal and sliding contact.

The mechanical properties of thin layers in layered media are usually determined from indentation tests. Hardness is one of the most important mechanical properties of thin surface layers, especially those used in tribological applications. As surface layer thickness becomes thinner and thinner, in order to avoid the substrate effect on hardness measurements, smaller interference distances (indentation or contact depths) must be obtained. However, the real material hardness cannot be deduced until a certain interference distance is reached. Therefore, it is of great importance to understand the relationship between hardness and interference distance, and to develop a theoretical treatment for valid hardness measurement.

Closed-form solutions are usually not possible to obtain for elastic-plastic contact problems in layered media, especially when other important but complex aspects, such as surface topography, residual stresses in the top layer, and coupling between thermal and mechanical tractions are taken into account. However, numerical techniques, such as the finite element method, provide the means to analyze complex contact problems of this kind. Among all the available numerical techniques, the finite element method is the most widely used since it can deal with complicated geometries, layered media, and coupled electrical, thermal, and mechanical effects.

The main objective of this dissertation was to provide a comprehensive contact analysis of elastic-plastic layered media using the finite element method, with particular emphasis on: contact between rough surfaces, thermal-mechanical sliding contact, sliding on layered media with surface layers under residual stress, and valid hardness

measurement of thin-film layered media. The contents of Chapter 2 to 7 are summarized in the following paragraphs.

Chapter 2 introduces a three-dimensional contact analysis of elastic-plastic layered media with fractal surface topographies. Three-dimensional rough surfaces are generated using a modified two-variable Weierstrass-Mandelbrot function with fractal parameters determined from real surface images. The number and size of truncated asperities are assumed to follow power-law relations. A finite element model of a rigid sphere in normal contact with a semi-infinite elastic-plastic homogeneous medium is used to obtain a constitutive relation between the mean contact pressure, real contact area, and corresponding representative strain. The contact model is then extended to layered media by modifying the constitutive equation of the homogeneous medium to include the effects of the mechanical properties of the layer and substrate materials and the layer thickness. Finite element simulations of an elastic-plastic layered medium indented by a rigid sphere are used to validate the correctness of the modified contact model. Numerical results for the contact load and real contact area are presented for real surface topographies resembling those of magnetic recording heads and smooth rigid disks. The model yields insight into the evolution of elastic, elastic-plastic, and fully plastic deformation at the contact interface in terms of the maximum local surface interference. The dependence of the contact load and real contact area on the fractal parameters and the carbon overcoat thickness is interpreted in light of simulation results obtained for a tri-pad picoslider in contact with a smooth thin-film hard disk.

Chapter 3 presents an elastic-plastic contact analysis based on a finite element model and real surface topographies performed to elucidate the evolution of deformation

at the head-disk interface. The topographies of the head and disk surfaces are represented by an equivalent profile generated using a modified two-variable Weierstrass-Mandelbrot function, with fractal parameters determined from images of head and disk surfaces. A region of the equivalent rough surface profile is selected for analysis based on topography scale considerations and contact simulation results. The evolution of plasticity and the likelihood of cracking in the overcoat and the magnetic layer are interpreted in light of results for the subsurface von Mises equivalent stress, equivalent plastic strain, and maximum first principal stress. The finite element model provides insight into the elastic-plastic deformation behavior of the layered medium in terms of the thickness, mechanical properties, and residual stress in the carbon overcoat.

In Chapter 4, the coupled effects of mechanical and thermal surface traction on the deformation of layered media are analyzed with the finite element method. A three-dimensional model of an elastic spherical asperity sliding over an elastic-plastic layered medium is developed and validated by comparisons of finite element results with analytical and numerical solutions for the surface stresses and temperature distribution on an elastic homogeneous half-space. The evolution of deformation in the layered medium due to thermomechanical surface traction is interpreted in light of the dependence of temperature, von Mises equivalent stress, first principal stress, and equivalent plastic strain on the layer thickness, Peclet number, and sliding distance. The propensity for plastic flow and microcracking in the layered medium is discussed in terms of the layer thickness and thermal properties, sliding speed, medium compliance, and normal load. It is shown that friction and thermal traction promote stress intensification and plasticity, especially in the case of relatively thin layers of low thermal conductivity.

Chapter 5 describes a finite element analysis of deformation of layered media under normal and sliding contact traction with residual stress in the top layer. A three-dimensional finite element model of a rigid spherical asperity indenting and sliding on an elastic-plastic layered medium is developed and validated. A series of finite element simulations are performed at varying magnitudes of residual stress in the top layer and with two different coefficients of friction. The effect of residual stress and coefficient of friction on plastic flow and microcracking in the layered medium is discussed in the context of simulation results. The optimal value of residual stress normalized by maximum contact pressure is shown to be between –0.5 and 0; however, the exact value depends upon the type of contact (normal or sliding), coefficient of friction, and the deformation mode of the overcoat.

Chapter 6 presents an analysis of hardness measurement of layered media. For hardness measurement of layered media, a critical value of interference distance, below which the substrate effect can be neglected, between the sphere and the layered medium is obtained from Bhattacharya and Nix's equation of equivalent hardness variation with interference distance. Subsequently, finite element model is developed to simulate indentation of elastic-plastic homogeneous and layered media by a rigid sphere. From the finite element simulation results on homogeneous media, a relationship between hardness, yield strength, and elastic modulus is obtained. This relationship in conjunction with a contact constitutive model developed in Chapter 2 is used to derive a minimum interference distance, above which sufficient plasticity can be induced and the real hardness of a material can be reached. A new scheme of hardness measurement on thin-

film media is proposed and validated by finite element simulation results for a layered medium.

Chapter 7 concludes the dissertation by summarizing the main findings of the work presented in Chapters 2-6.

CHAPTER 2

THREE-DIMENSIONAL CONTACT ANALYSIS OF ELASTIC-PLASTIC LAYERED MEDIA WITH FRACTAL SURFACE TOPOGRAPHIES

2.1 Introduction

Understanding of contact between rough surfaces is important in many engineering fields and has direct implications on the product performance of various leading-edge technologies, such as computer hard disk drives and microelectromechanical systems. In order to obtain analytical solutions for the subsurface stress and strain fields, the contact pressure and real contact area must be determined first. Although various analytical methods for obtaining such information have been reported (Aleksandrov et al., 1966; Alblas and Kuipers, 1970; Pao et al., 1971; Ling and Lai, 1980), these methods are fairly complex and programming is often inhibited by convergence problems.

In view of advances in sophisticated numerical methods, such as the finite element method, and remarkable enhancements in computational capabilities, such shortcomings were overcome in more recent contact mechanics studies. Johnson (1985) analyzed the indentation response of elastic-plastic solids and reported the successive occurrence of elastic, elastic-plastic, and fully plastic deformation with increasing indentation depth. Mesarovic and Fleck (1999) obtained deformation maps for strain-hardening homogeneous media indented by a rigid sphere and showed that the fully plastic region comprises two regimes: a similarity regime for small contact sizes and a finite-deformation plasticity regime for large contact sizes. Finite

element simulations of indented layered media by Kennedy and Ling (1974a), Van der Zwaag and Field (1982), Komvopoulos (1988, 1989), and Tian and Saka (1991) have shown a pronounced effect of the layer thickness and mechanical properties on the deformation behavior. Results from a three-dimensional finite element analysis of a rigid sphere indenting or sliding over an elastic-plastic layered medium performed by Kral and Komvopoulos (1996) have illustrated the effects of the layer material properties, coefficient of friction, and normal load on the sliding and residual stress fields and the forward plastic flow at the contact region.

Although significant insight into the mechanics of contacting solids has been obtained from the aforementioned analytical and numerical studies, the information obtained can only be related to the macroscopic deformation behavior because of the assumed ideally smooth surfaces. However, real surface topographies comprise geometrical features spanning a wide range of length scales, i.e., a similar topography is obtained after arbitrary magnification. Knowledge of the local deformation behavior at surface summits (asperity microcontacts) where actual contact occurs is of great importance to the durability of many engineering devices. One of the primitive contact models that accounts for roughness effects is attributed to Greenwood and Williamson (1966) who developed an asperity deformation criterion based on a probabilistic mathematical model of the surface height distribution. It was assumed that the asperity heights follow a normal distribution function, while the radii of curvature and lateral distribution of the asperities are invariant. Larsson et al. (1999) examined theoretically the initial flattening of rough surfaces and reported a linear contact area-load relation for a perfectly plastic material and an exponential asperity height distribution, and a nonlinear contact pressure-area relation for a normal asperity height distribution and strain hardening material behavior.

However, most engineering surfaces exhibit random and multi-scale topographies that can be characterized by fractal geometry (Mandelbrot, 1983; Borodich and Onishchenko, 1999). The advantages of using fractal geometry for surface description include scale invariance (i.e., independence of the measurements on the instrument resolution and the sample length) and self-affinity (i.e., as the magnification increases finer details of surface features similar to the original profile emerge). These important properties of fractal geometry make it appropriate for characterizing engineering surfaces over a wide range of length scales. The paper that, presumably, brought fractals to the attention of the engineering community is that of Majumdar and Tien (1990) who examined the roughness of steel surfaces and a textured magnetic thin-film disk and observed statistically similar surface images at various magnifications. It was reported that the surface roughness could be characterized by a Weierstrass-Mandelbrot (W-M) fractal function (Borodich and Onishchenko, 1999; Berry and Lewis, 1980) One of the first contact analysis to use a fractal description for the surface topography is that of Majumdar and Bhushan (1991). They obtained a relation for the real contact area and estimated the critical asperity size demarcating the transition from elastic to fully plastic asperity deformation. It was shown that small asperities deform plastically while large asperities deform elastically, a radically different result from what is predicted from the model of Greenwood and Williamson (1966). Blackmore and Zhou (1998a, 1998b) introduced a fractal-based functional model for anisotropic rough surfaces and argued that a very extensive class of engineering surfaces possesses surface height distributions that depend in significant ways on fundamental fractal parameters.

Ciavarella et al. (2000) considered normal contact between an elastic half-space and a rigid fractal surface, whose profile was defined by a Weierstrass series, and observed that, at

large wavelength numbers, the contact area exhibited limiting power-law fractal behavior. Wang and Komvopoulos (1994a, 1994b, 1995) developed a fractal contact theory for the temperature rise on elastic-plastic rough surfaces sliding in the slow and fast speed regimes and showed that a continuous transition from elastic to fully plastic deformation (i.e., elastic-plastic deformation) occurs at asperity microcontacts. It was also indicated that the elastic-plastic regime could be significantly broad, depending on the material properties and fractal dimensions of the sliding surfaces (Wang and Komvopoulos, 1994b). More recently, Yan and Komvopoulos (1998) introduced a three-dimensional fractal mechanics theory for elastic-plastic surfaces in normal contact and obtained numerical results for the average contact pressure and real contact area in terms of the mean surface separation distance.

Despite important information about contact deformation at smooth and rough surfaces obtained from the previous studies, a comprehensive contact analysis of elastic-plastic layered media exhibiting rough surface topographies (characterized by fractal geometry) has not been performed yet. Thus, the main objective of the present study was to bridge the gap between contact mechanics applicable to a single asperity microcontact and interactions occurring at multi-scale contact interfaces of layered media possessing realistic surface topographies. To accomplish this goal, a finite element model was developed in order to obtain relations between the mean contact pressure and real contact area for a single spherical asperity indenting an elastic-plastic homogeneous medium in terms of a representative strain, which is a function of the surface interference distance and the mechanical properties of the medium. The constitutive model was extended to layered media to account for the mechanical properties of the layer and substrate materials and the effect of the layer thickness. For multi-scale surface description,

three-dimensional fractal geometry was used to characterize the surface topography. The effects of the fractal parameters and layer thickness on the contact load and real contact area are interpreted in light of results obtained for a tri-pad picoslider in contact with a smooth thin-film disk.

2.2 Surface Modeling

The topographies of engineering surfaces have been traditionally quantified in terms of the height variance, slope, and curvature of surface summits. The values of these parameters depend on the instrument resolution and the sample length. However, a realistic multi-scale roughness description can only be accomplished by using scale-independent parameters, such as the scale-invariant parameters used in fractal geometry (Mandelbrot, 1983; Borodich and Onishchenko, 1999). A three-dimensional fractal surface topography can be generated using a modified (truncated) two-variable W-M function (Mandelbrot, 1983; Borodich and Onishchenko, 1999) that can be written as (Yan and Komvopoulos, 1998)

$$z(x,y) = L\left(\frac{G}{L}\right)^{D-2}\left(\frac{\ln g}{M}\right)^{1/2}\sum_{m=1}^{M}\sum_{n=0}^{n_{\max}} g^{(D-3)n}\left\{\cos f_{m,n} - \cos\left[\frac{2\pi g^{n}\left(x^2+y^2\right)^{1/2}}{L}\cos\left(\tan^{-1}\left(\frac{y}{x}\right)-\frac{\pi m}{M}\right)+f_{m,n}\right]\right\}, \quad (2.1)$$

where L is the sample length, G is the fractal roughness, D is the fractal dimension ($2 < D < 3$), g ($g > 1$) is a scaling parameter, M is the number of superposed ridges used to construct the surfaces, n is a frequency index, with $n_{\max} = \text{int}\left[\log(L/L_s)/\log g\right]$ representing the upper limit of n, where L_s is the cut-off length, and $f_{m,n}$ is a random phase. The scaling parameter g controls the density of frequencies in the surface profile. Based on surface flatness and frequency distribution density considerations, g = 1.5 (Yan and Komvopoulos, 1998). For a

truncated series (i.e., starting at $n = 0$ rather than $n = -\infty$ (Eq. (2.1)), the scaling property is approximate, i.e., scaling is satisfied only to within a small additive term (Ausloos, M., and Berman, D. H., 1985). Thus, the surface function given by Eq. (2.1) possesses a scale-invariant (fractal) behavior (Berry and Lewis, 1980) only within a finite range of length scales, outside of which, the surface topography can be represented by a deterministic function (Wang and Komvopoulos, 1994b). In practice, the smallest length corresponds to the instrument resolution and the upper length to the length of the profile. Because frequencies outside the range determined by the lower and upper wavelengths do not contribute to the observed profile, self-similarity is satisfied at all scales only approximately (Russ, 1994). The fractal roughness G is a height scaling parameter independent of frequency (within the scale range that fractal power-law behavior is observable). The magnitude of the fractal dimension D determines the contribution of high and low frequency components in the surface function $z(x,y)$. Thus, high values of D indicate that high-frequency components are more dominant than low-frequency components in the surface topography profile. The surface height function given by Eq. (2.1) is continuous, non-differentiable, scale-invariant (in the range determined by the upper and lower wavelengths used in the truncated series), and self-affine (asymptotically self-affine according to the analysis of Blackmore and Zhou (1998a, 1998b)). The latter implies that as the surface is repeatedly magnified, more and more surface features appear and the magnified image shows a close resemblance to that of the original surface obtained at a different scale. These properties make the function given by Eq. (2.1) suitable for constructing surfaces possessing topographies closely resembling the actual surfaces from which the fractal parameters D and G were determined experimentally.

2.3 Elastic-Plastic Constitutive Model

A system of two contacting rough surfaces can be replaced by an equivalent system of a flat deformable surface with an effective elastic modulus $E^* = \left[\left(1-n_1^2\right)/E_1 + \left(1-n_2^2\right)/E_2\right]^{-1}$, where n_1, n_2, and E_1, E_2 are the Poisson's ratios and elastic moduli of the two interacting surfaces, respectively, and a rigid rough surface with a power spectrum equal to the sum of the power spectra of the two original surfaces. It is assumed that surface contact comprises numerous spherical asperity microcontacts, which are sufficiently apart from each other in order for asperity interactions to be neglected as secondary. This is a reasonable assumption for the relatively small interference distances (or light contact loads) considered in this study. Based on these assumptions and knowledge of the mean contact pressure and real contact area at asperity microcontacts, the total contact load and real contact area can be obtained using an integration procedure. It is necessary, therefore, to derive a constitutive model for a single asperity microcontact.

In a previous study (Yan and Komvopoulos, 1998), the stress-strain behavior of asperities was assumed to be either purely elastic or fully plastic, i.e., the intermediate range of elastic-plastic deformation was not considered. Hertz theory can be used to analyze contact of elastically deformed asperities. For fully plastic microcontacts where the plastic zone is not contained by elastic material, the mean contact pressure is equal to the material hardness. However, as the interference distance at an asperity microcontact increases, a gradual transition from elastic to fully plastic deformation occurs. In this regime, the plastic zone is small and fully contained by surrounding elastic material and the overall deformation behavior is elastic-plastic

(Johnson, 1985; Mesarovic and Fleck, 1999). Therefore, to accurately determine the contact force between two approaching surfaces, the stress-strain constitutive relation and the real contact area corresponding to the elastic-plastic deformation regime should be incorporated into the previous elastic-fully plastic contact model (Yan and Komvopoulos, 1998).

A constitutive relation was obtained from a finite element model of a rigid sphere in normal contact with an elastic-perfectly plastic homogeneous half-space modeled by axisymmetric eight-node quadratic elements. The finite element mesh consisted of 5395 elements comprising 16622 nodes. The simulations were performed in 12 steps of 80 increments each. The typical computational time on an IBM RS6000 (580 model) workstation was about 18000 CPU seconds. The multi-purpose code ABAQUS was used to perform the finite element simulations. The mean contact pressure, p_m, and real contact area, a, were obtained in terms of the interference distance between the rigid sphere and the surface of the deformable medium, d. Figures 2.1 (a) and 2.1(b) show the normalized mean contact pressure, p_m / s_Y, and the truncated-to-real contact area ratio, a'/a, versus the representative strain, $E^* d / s_Y r'$, where s_Y is the yield strength of the deformable medium and r' is the radius of the truncated contact area a'. The representative strain is different from that used by Johnson (1985) to describe the evolution of deformation in an elastic-perfectly plastic material indented by a sphere, defined as $E^* r / s_Y R$, where r is the radius of the real contact area and R is the radius of curvature of the rigid sphere. However, because the radius of the real contact area is not known from the geometric truncation, the interference and truncated radius were used to determine the representative strain. Elastic, elastic-plastic, and fully plastic deformation regimes

are distinguished in Fig. 2.1. Increasing the surface interference (or representative strain) yields a continuous increase of the mean contact pressure accompanied by a decrease of the contact area ratio. Figure 2.2 shows a comparison between results obtained with the present finite element model and the classical Hertz theory for an elastic half-space indented by a rigid sphere. The favorable comparison of the results of the two methods illustrates the suitability of the finite element model (for the present analysis involving only global variables, such as the contact pressure and contact area) and the correctness of the assumed boundary conditions.

The simulation results shown in Fig. 2.1 were used to derive relations for the mean contact pressure and contact area in terms of the local interference and elastic-plastic material properties. Thus, from curve fitting, the following constitutive relations were obtained.

For elastic deformation ($E^*d / \sigma_Y r' < 1.78$),

$$\frac{p_m}{\sigma_Y} = \frac{4\sqrt{2}}{3\pi}\left(\frac{E^* d}{\sigma_Y r'}\right), \qquad \frac{a'}{a} = 2 \tag{2.2}$$

For elastic-plastic deformation ($1.78 \le E^*d / \sigma_Y r' < 21$),

$$\frac{p_m}{\sigma_Y} = 0.70 \ln\left(\frac{E^* d}{\sigma_Y r'}\right) + 0.66, \quad \frac{a'}{a} = 0.05\left[\ln\left(\frac{E^* d}{\sigma_Y r'}\right)\right]^2 - 0.57 \ln\left(\frac{E^* d}{\sigma_Y r'}\right) + 2.41. \tag{2.3}$$

For fully plastic deformation ($21 \le E^*d / \sigma_Y r' \le 400$),

$$\frac{p_m}{\sigma_Y} = 2.9, \qquad \frac{a'}{a} = 0.05\left[\ln\left(\frac{E^* d}{\sigma_Y r'}\right)\right]^2 - 0.57 \ln\left(\frac{E^* d}{\sigma_Y r'}\right) + 2.41. \tag{2.4}$$

For fully plastic deformation ($400 < E^*d / \sigma_Y r'$),

$$\frac{p_m}{\sigma_Y} = 2.9, \qquad \frac{a'}{a} = 0.71 \tag{2.5}$$

Results for the mean contact pressure and contact radius obtained from Eqs. (2.2)-(2.5) were found to be in good agreement with finite elements results reported by Mesarovic and Fleck (1999) for elastic-plastic homogeneous solids indented by a rigid sphere. In particular, the deformation regime defined by Eq. (2.5) is consistent with the plastic similarity regime reported by Mesarovic and Fleck (1999).

The constitutive relations given by Eqs. (2.2)-(2.5) are for a homogeneous elastic-plastic half-space. However, it is possible to extend the present contact model to layered media by appropriately modifying the above relations to include the effects of the mechanical properties of the layer and substrate materials and the layer thickness. This was accomplished by introducing the equivalent material properties in the constitutive relations given by Eqs. (2.2)-(2.5). Assuming that the yield strength is equal to one-third of the material hardness (Tabor, 1970), the equivalent yield strength of a layered medium, $s_{Y,e}$, can be expressed as (Bhattacharya and Nix, 1988)

$$s_{Y,e} = s_{Y,s} + \left(s_{Y,l} - s_{Y,s}\right)\exp\left[-\left(\frac{d}{h}\right)\left(\frac{E_s}{E_l}\right)^{1/2}\right], \tag{2.6}$$

where h is the overcoat thickness, E is the elastic modulus, and subscripts l and s denote the layer and substrate material properties, respectively. The equivalent effective elastic modulus of a layered medium, E_e^*, is given by (King, 1987)

$$E_e^* = \left[\left(1 - e^{-a\,h/r\sqrt{p}}\right)\frac{1-n_l^2}{E_l} + e^{-a\,h/r\sqrt{p}}\,\frac{1-n_s^2}{E_s} + \frac{1-n_i^2}{E_i}\right]^{-1}, \tag{2.7}$$

where a is a geometrical factor that depends on the indenter shape and can be determined numerically, n is the Poisson's ratio, and subscript i denotes the indenter material. It is noted

that only the elastic properties of the indenting surface are included in Eq. (2.7), i.e., plastic deformation is confined only in the layered medium (Eq. (2.6)). Based on Eqs. (2.6) and (2.7), the nondimensional representative strain for a layered medium, $E_e^* d / s_{Y,e} r'$, can be obtained as a function of the known mechanical properties of the indenter, layer, and substrate materials, layer thickness, and surface interference distance.

To validate the modified contact model, finite element simulation results for an elastic-plastic layered medium indented by a rigid sphere were contrasted with results obtained from the contact model (Eqs. (2.2)-(2.5)), using Eqs. (2.6) and (2.7) to account for the effects of the layer (overcoat) thickness and material properties. The finite element mesh, shown in Fig. 2.3, consists of 12063 axisymmetric eight-node isoparametric elements comprising 34337 nodes. The nodes of the left vertical boundary were fixed against displacement in the horizontal direction, whereas the nodes of the bottom boundary were fixed against displacement in the vertical direction. Simulations were performed for an overcoat thickness h = 2, 5, and 10 nm. The elastic modulus and yield strength of the overcoat material were set equal to 114 and 5.67 GPa and those of the substrate material equal to 130 and 2.67 GPa, respectively. To account for geometric nonlinearities resulting from large displacements, an updated Lagrangian formulation was adopted in the finite element analysis. The typical computational time for a simulation on a Pentium III 550 computer was approximately 40000 CPU seconds.

Figure 2.4 shows the normalized mean pressure as a function of the modified representative strain. The symbols represent finite element data corresponding to different overcoat thickness values. The solid curve is the solution obtained from the modified contact

model (Eqs. (2.2)-(2.7)). The figure shows that the results are in excellent agreement. In addition to the mean contact pressure, it is also necessary to verify whether the prediction of the real contact area was accurate. Figure 2.5 shows a comparison between results for the normalized contact radius obtained from the modified contact model, r_{CM}/R (with equivalent material properties given by Eqs. (2.6) and (2.7)) and the contact radius determined from the finite element analysis of the indented elastic-plastic layered medium, r_L/R, where R is the radius of the rigid sphere. The best-fit line to the data yields a correlation factor of 0.9992. The error between analytical and numerical results is less than 5%. In view of Figs. 2.4 and 2.5, it may be concluded that the contact constitutive model originally developed for homogenous media can be extended to layered media by introducing the equivalent material properties of the layered medium. The constitutive relations for the mean contact pressure and real contact area, reflecting a continuous transition from elastic to fully plastic deformation, were used in the three-dimensional contact analysis of rough surfaces characterized by fractal geometry described in the following section.

2.4 Surface Contact Model

As mentioned previously, the equivalent contact model of two rough surfaces comprises an elastic-plastic medium in contact with a rigid rough surface. The mechanical properties of the medium and the topography (described by fractal geometry) of the rough surface are equivalent to those of the contacting surfaces. As the rough surface approaches the deformable medium, asperity microcontacts are established over the simulated apparent contact area. Depending on the local surface interference and asperity radius, elastic, elastic-plastic, or fully plastic

deformation may occur at asperity microcontacts. Following an analytical procedure similar to that detailed elsewhere (Yan and Komvopoulos, 1998), the total contact load and real contact area at a given maximum surface interference distance, $d_{\max}$, was calculated from the total truncated contact area of the rough surface, S', given by,

$$S' = \int_{a'_S}^{a'_L} a' n(a') da', \tag{2.8}$$

where a' is the truncated area of a microcontact, a'_L and a'_S are the largest and smallest truncated microcontact areas, respectively, and $n(a')$ is the truncated asperity size distribution function. At a given surface interference, the number of microcontacts with truncated areas between a' and $a'+da'$ is given by $n(a')da'$. For a continuum description, the size of the smallest microcontact should be greater than the atomic dimensions; thus, the diameter of the smallest truncated area, a'_S, is assumed to be equal to six times the lattice dimension of the overcoat material.

The number of truncated asperities, N, with areas greater than a particular truncated area, a', is assumed to follow the power-law relation (Mandelbrot, 1983),

$$N(a') = \left(\frac{a'_L}{a'} \right)^{(D-1)/2}. \tag{2.9}$$

Consequently, the truncated asperity size distribution function can be expressed as (Yan and Komvopoulos, 1998)

$$n(a') = -\frac{dN(a')}{da'} = \frac{(D-1)}{2a'_L} \left(\frac{a'_L}{a'} \right)^{(D+1)/2}. \tag{2.10}$$

Substituting Eq. (2.10) into Eq. (2.8), the total truncated area of the fractal surface can be

written as

$$S' = \frac{D-1}{3-D}\left(a'_L - a'_L{}^{(D-1)/2}\, a'_S{}^{(3-D)/2}\right). \tag{2.11}$$

At a given surface interference, the total truncated contact area, S', can be obtained by numerical integration. Using a grid mesh of size equal to the diameter of the smallest truncated microcontact, a'_s, the number of surface points above the truncation plane was determined and the total truncated area was obtained as the apparent area multiplied by the ratio of the number of truncated surface points to the total number of grid points. From the obtained total truncated area, S', the truncated area of the largest microcontact, a'_L, was calculated from Eq. (2.11). Hence, a series of truncated asperities can be generated using Eq. (2.9). Figure 2.6 shows a comparison between analytical results (obtained from Eq. (2.11) for $a'_s = 0$) and numerical results for small surface interference distances, typical of those used in the surface contact simulations. The fair agreement between the results of the two methods suggests that the assumption of a power-law asperity distribution is reasonable.

The local interference, d_i, at the i^{th} asperity is given by (Yan and Komvopoulos, 1998)

$$d_i = 2G^{(D-2)}(\ln g)^{1/2}(2r_i')^{(3-D)}. \tag{2.12}$$

As discussed in the previous section, the representative strain at an asperity microcontact, $E^* d_i / s_Y r_i'$, in the case of a layered medium can be obtained in terms of the equivalent yield strength and equivalent (effective) elastic modulus given by Eqs. (2.6) and (2.7), respectively. However, because the equivalent elastic modulus is a function of the real contact radius, which is not known *a priori*, an iteration procedure was used to determine the equivalent elastic modulus and real contact radius from Eqs. (2.2)-(2.5) and (2.7). The initial

value of the real contact radius was assumed to be equal to the truncated radius. Using this iteration scheme for the calculation of the equivalent elastic modulus, the representative strain was found and a new value was obtained for the real contact radius. This iteration procedure was repeated until the change in the real contact radius approached a specified small tolerance value (e.g., 1%). Typically, six or seven iterations were required to obtain the equivalent elastic modulus and real contact radius. Subsequently, the mean contact pressure, $p_{m,i}$, and real contact area, a_i, at the ith asperity microcontact were determined from the appropriate constitutive relations (Eqs. (2.2)-(2.5)), depending on the deformation regime. The contact force at the i^{th} asperity, dL_i, is given by

$$dL_i = p_{m,i} a_i . \tag{2.13}$$

The total contact force, L, and total real contact area, A_r, were obtained by numerical integration,

$$L = \sum_{i=1}^{N(a'_s)} dL_i = \sum_{i=1}^{N(a'_s)} p_{m,i} a_i , \tag{2.14}$$

and

$$A_r = \sum_{i=1}^{N(a'_s)} a_i , \tag{2.15}$$

where $N(a'_s)$ is the total number of truncated asperities. The advantage of this analytical method is that it requires significantly less computational time than other numerical techniques requiring a large and very fine mesh, such as the finite element method.

2.5 Results and Discussion

Figure 2.7 shows a 1 μm x 1 μm fractal surface generated from Eq. (2.1) for D = 2.44,

$G = 9.46 \times 10^{-13}$ m, $M = 10$, $g = 1.5$, $L = 1$ μm, and L_s equal to six times the lattice dimension of carbon. Since the sample length, L, was chosen to be smaller than the upper limit of the sample length for fractal characterization (Wang and Komvopoulos, 1994b; Komvopoulos, 2000), the entire apparent contact area (Fig. 2.7) can be described by fractal geometry. The fractal parameters D and G were determined from a log-log plot of the structure function versus wavelength of a surface profile equivalent to those of a magnetic head and a smooth (rms ~0.2 nm) thin-film disk imaged with an atomic force microscope (Komvopoulos, 2000). The power spectrum of the equivalent surface, shown in Fig. 2.8, is equal to the sum of the power spectra of the head and the disk surfaces. Isotropic random surfaces are characterized by axially symmetric power spectra. With the exception of two orthogonal bands along the frequency axes, the power spectrum in Fig. 2.8 shows axial symmetry. As explained in a previous study (Yan and Komvopoulos, 1998), these artificial bands occur due to the unmatchness of the opposing boundaries of the simulated surface and can be removed using the simple technique proposed by Anguiano et al. (1994).

Contact simulations were performed for a hard disk coated with a carbon overcoat possessing an elastic modulus of 114 GPa and yield strength of 5.67 GPa in contact with a tri-pad picoslider coated with a carbon overcoat (Fig. 2.9). In view of the small surface interference distances examined, the elastic modulus of the picoslider surface was set equal to that of the carbon overcoat for simplicity. Contact was assumed to occur only at the trailing edge of the center-pad of the picoslider, which has an apparent contact area of 250 μm × 40 μm. The contact loads and corresponding real contact areas determined from simulations performed on 1 μm x 1 μm surface areas (such as that shown in Fig. 2.7) were multiplied by a

factor of 10^4 in order to convert them to picoslider data. These are obviously upper bound results since the picoslider may contact the disk surface at some angle, i.e., the actual apparent contact area may be a portion of the trailing edge of the picoslider's center-pad.

For the range of surface interferences considered in this study, the multi-layered disk medium can be simplified to a two-layered medium. This is because the stress and strain fields are confined within the carbon overcoat and the magnetic layer (Komvopoulos, 2000). To reveal the effects of the surface topography and overcoat thickness on the magnitude of the contact load and deformation behavior, results for the contact load and real contact area are presented for a homogeneous medium with carbon overcoat properties and different fractal parameters, followed by results for a layered medium with a carbon overcoat of varying thickness and surface topography identical to that of the homogeneous medium.

Figures 2.10(a) and 2.10(b) show the variation of the total contact load on the picoslider, L, and the real to apparent contact area ratio, A_r/A_a, with the maximum surface interference distance, $d_{\max}$. The elastic and plastic (including both elastic-plastic and fully plastic microcontacts) components of each parameter are also plotted in order to elucidate the dominant deformation mode as a function of the maximum interference distance. Both the elastic and the plastic components of the contact load and the real contact area increase rapidly with increasing surface interference at the head-disk interface. However, the contribution of the plastic component is secondary, except at very small surface interferences. This is expected because at small surface interferences (or low contact loads) actual contact occurs at the smaller (sharper) asperities residing on top of larger asperities. Because it is easier for the yield condition to be satisfied at the smaller microcontacts (Yan and Komvopoulos, 1998), the

resulting deformation behavior at small surface interferences is predominantly inelastic (i.e., elastic-plastic and fully plastic). Figure 2.10(b) shows that the real contact area is a very small fraction of the apparent contact area. Since the typical load on a picoslider (in the absence of high adhesion forces) is below 1 g, the corresponding real contact area is significantly less than 1% of the apparent contact area.

The significance of the fractal dimension D and fractal roughness G on the contact load and real contact area can be interpreted in light of the results shown in Figs. 2.11 and 2.12, respectively. For fixed fractal roughness and maximum surface interference, increasing the fractal dimension increases the contact load and the real contact area significantly (Fig. 2.11). This is expected because larger D values are associated with smoother (denser) surface profiles, which, obviously, exhibit a greater load bearing capacity due to the resulting larger real contact areas. A similar trend occurs when the fractal roughness G decreases and the fractal dimension D is fixed (Fig. 2.12). Since G is a height scaling parameter, higher G values correspond to rougher (less dense) surface topographies characterized by a lower load bearing capacity due to the smaller real contact areas produced. Roughening (texturing) for reducing intimate surface contact is a well-established technique used in various tribological systems to suppress the occurrence of high adhesion forces (stiction), such as in disk drives and microelectromechanical systems. A comparison of Figs. 2.11(c) and 2.12(c) shows that the effect of the fractal roughness G on the portion of the real contact area undergoing inelastic deformation, $A_{r,p}$, is relatively less pronounced than that of the fractal dimension D. It appears that the evolution of plasticity at the contact region reaches a maximum for a fractal roughness value of the order of $\sim 10^{-13}$ m (Fig. 2.12(c)).

To illustrate the effect of the substrate material (magnetic layer) on the magnitudes of the contact load and real contact area, results for a homogeneous half-space with carbon overcoat material properties and a layered medium with a carbon overcoat of thickness h = 2, 5, and 10 nm are contrasted in Figs. 2.13 and 2.14. The surface topography was generated from Eq. (2.1) using the parameters of the surface shown in Fig. 2.7. As expected, the effect of the underlying magnetic medium is insignificant at small surface interference distances (or light contact loads). In all cases, increasing the surface interference produces a pronounced increase in the contact load (Fig. 2.13(a)) and the inelastic portion of the real contact area (Fig. 2.13(b)). However, as the overcoat thickness increases from 2 to 10 nm the results for the layered medium gradually approach those of the homogeneous medium. This is because a stronger substrate effect is encountered with thinner overcoats and the elastic modulus of the magnetic medium (i.e., the substrate of the layered medium) is greater than that of the carbon overcoat. Since the deformation at the contact region is predominantly elastic, illustrated by the extremely small fraction of inelastically deformed asperity microcontacts (Fig. 2.13(b)) and by comparing the elastic and plastic contact load components, L_e and L_p, shown in Figs. 2.14(a) and 2.14(b), respectively, higher contact loads are obtained with the stiffer layered medium. Thus, a slightly higher contact load is produced with the 2-nm-thick overcoat due to the most pronounced effect of the stiffer substrate. Figure 2.14 indicates that the main difference in the contact load results for layered and homogeneous media is due to the dominance of elastic deformation, whereas differences between the results for overcoats of different thickness are attributed to the effect of the substrate material (magnetic medium), which depends on the overcoat thickness.

2.6 Conclusions

A three-dimensional contact model was developed for elastic-plastic layered media with rough surfaces characterized by fractal geometry. Numerical results were presented for the head-disk contact interface using realistic surface topographies, constructed from a truncated W-M function with fractal parameters obtained from a surface equivalent to those of a magnetic recording head and a smooth carbon-coated thin-film disk. Based on the obtained results and discussions, the following main conclusions can be drawn.

(1) Constitutive relations for the mean contact pressure and real contact area versus a representative strain parameter were derived from a finite element model of a rigid sphere indenting an elastic-plastic medium. The constitutive model accounts for elastic, elastic-plastic, and fully plastic deformation at asperity microcontacts.

(2) The representative strain in the constitutive model is a local deformation parameter that depends on the mechanical properties of the contacting surfaces, the local surface interference distance, and the contact radius of the truncated asperities.

(3) For a given surface topography of the head-disk interface, both the contact load and the real contact area at the trailing edge of the center-pad of a picoslider increase monotonically with increasing maximum surface interference distance.

(4) The contact load decreases with decreasing fractal dimension D and/or increasing fractal roughness G. This is due to the effect of fractal parameters on the load bearing surface area. The effect of the mechanical properties of the magnetic medium on the contact load and deformation behavior at the real contact area becomes more pronounced with decreasing overcoat thickness.

(5) For the surface interference range examined, the effect of the overcoat thickness on the

contact load and real contact area is relatively small and the dominant deformation mode at asperity microcontacts is elastic.

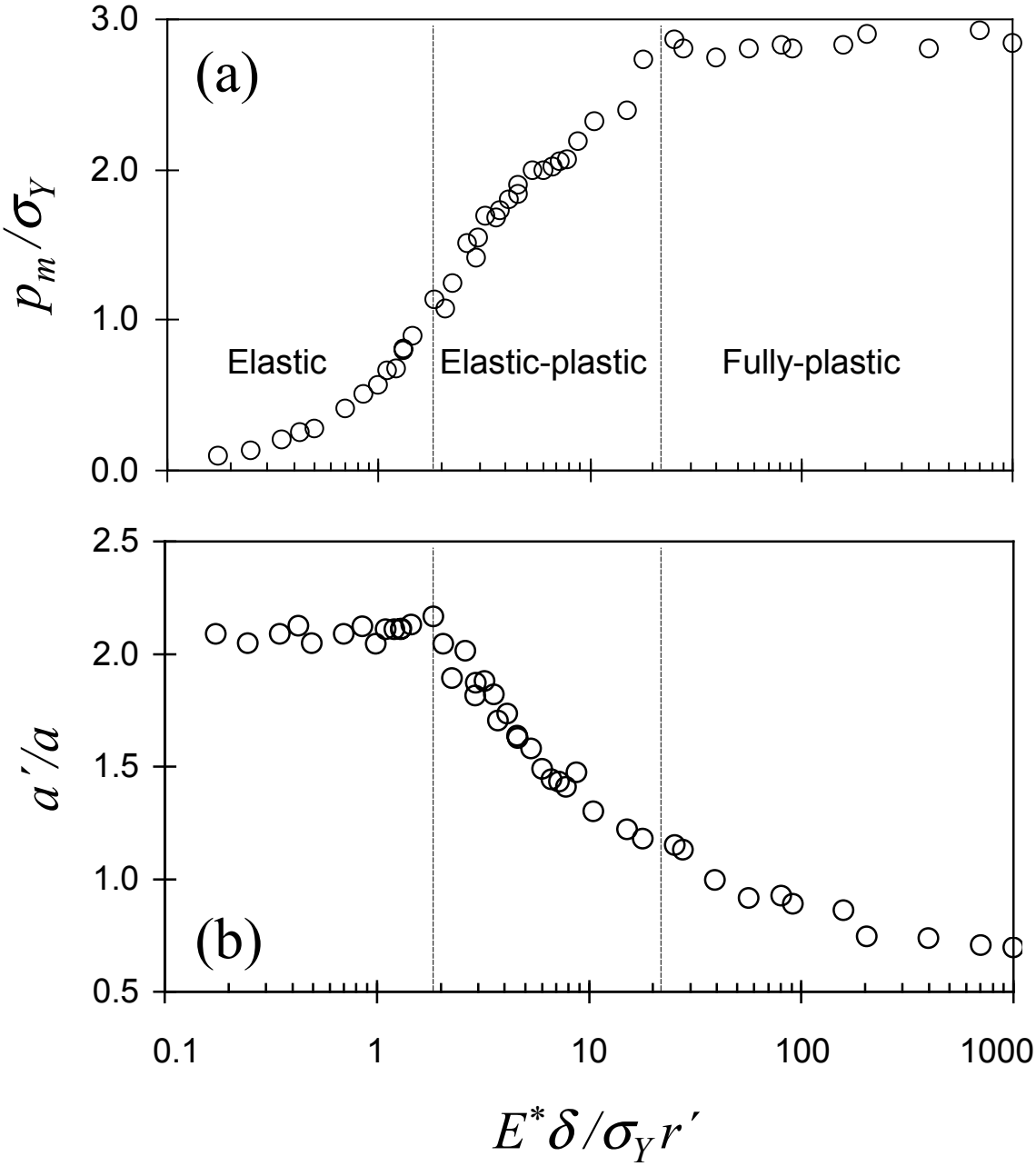

Figure 2.1 (a) Normalized mean contact pressure and (b) ratio of truncated to real contact areas versus representative strain.

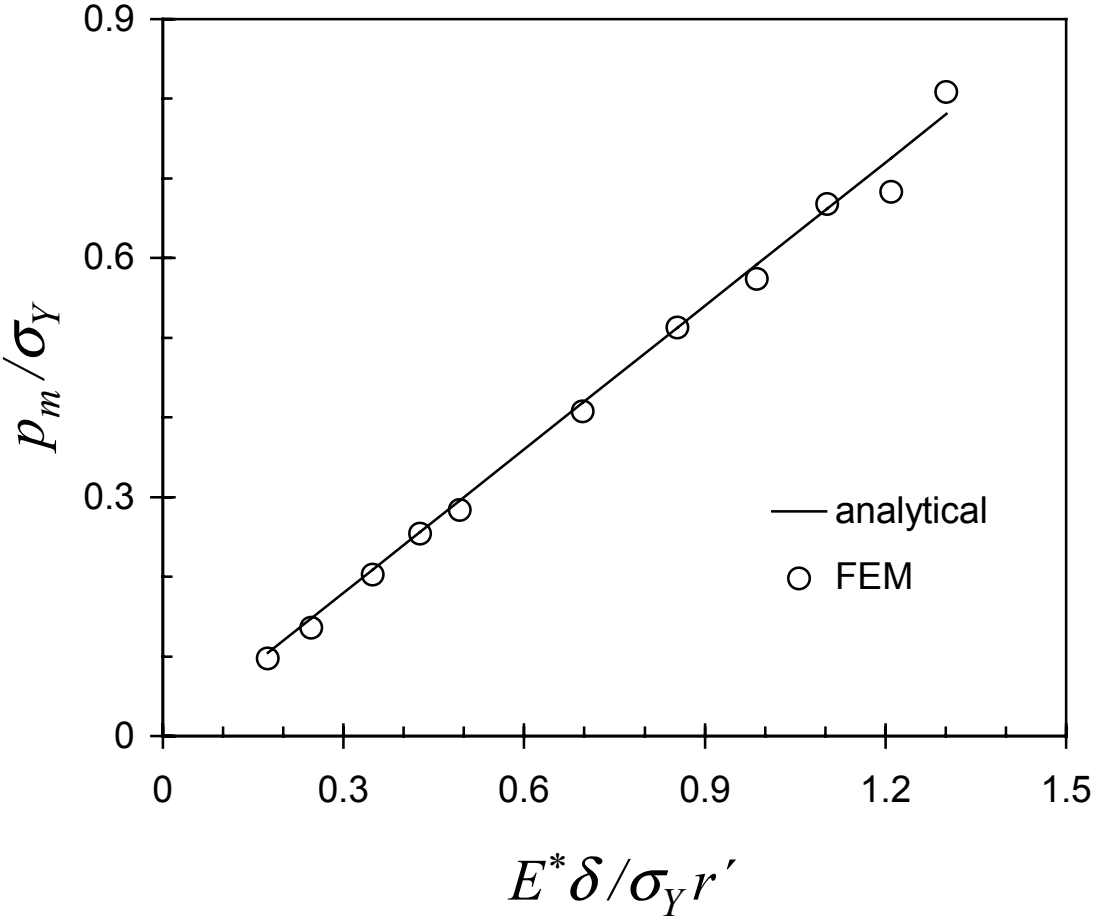

Figure 2.2 Comparison of analytical and finite element results for the normalized mean contact pressure versus representative strain for a homogeneous medium.

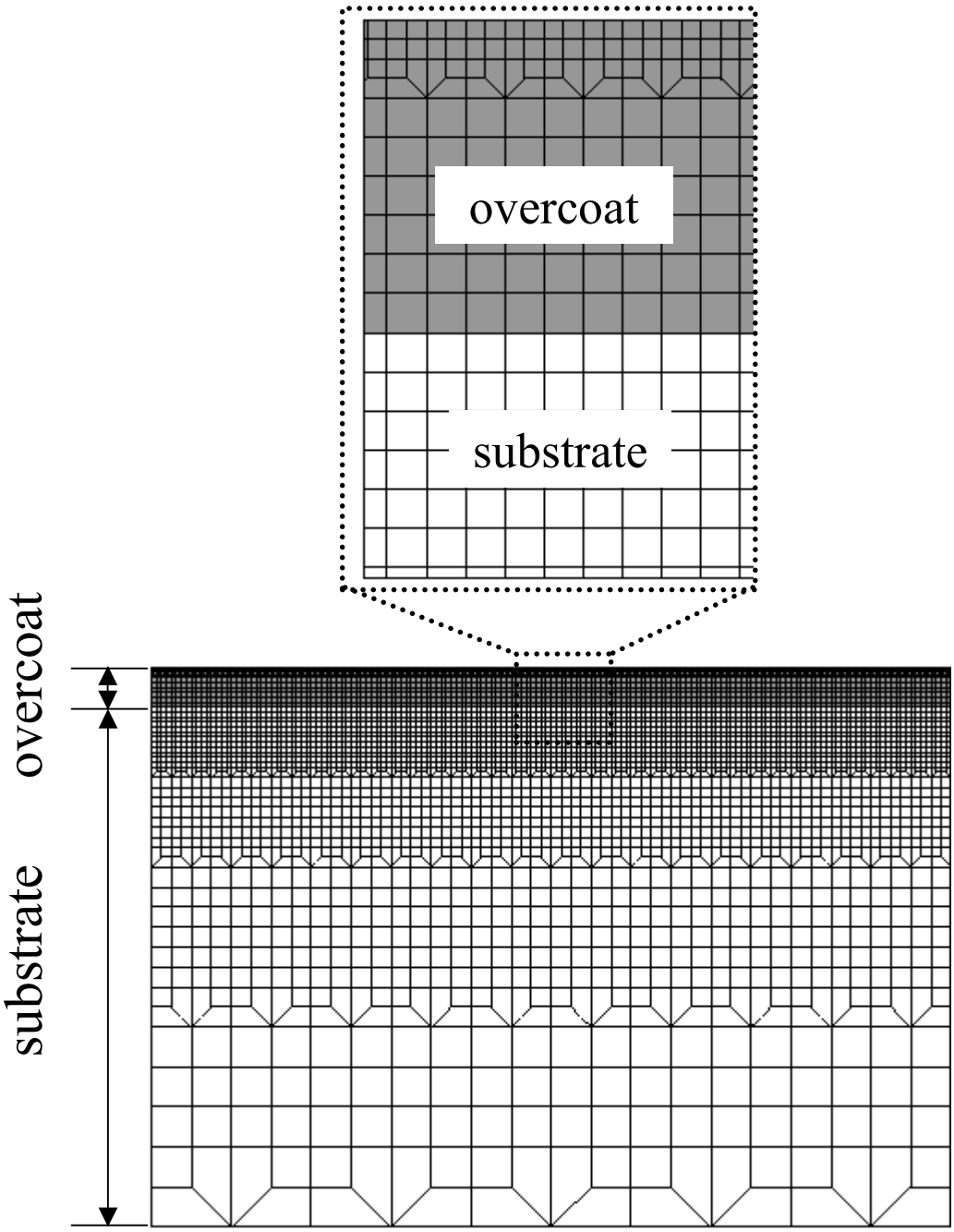

Figure 2.3 Finite element mesh of the layered medium.

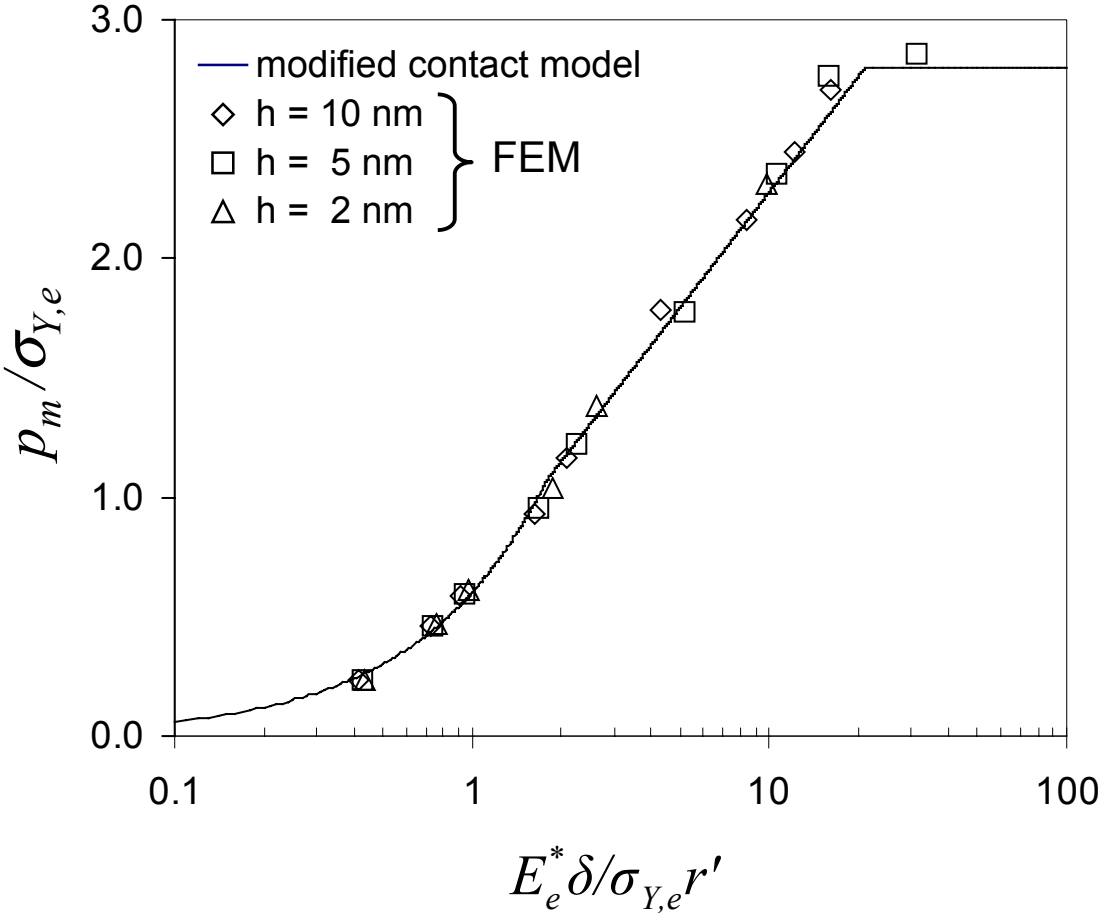

Figure 2.4 Normalized mean contact pressure versus representative strain for a layered medium with different layer thickness.

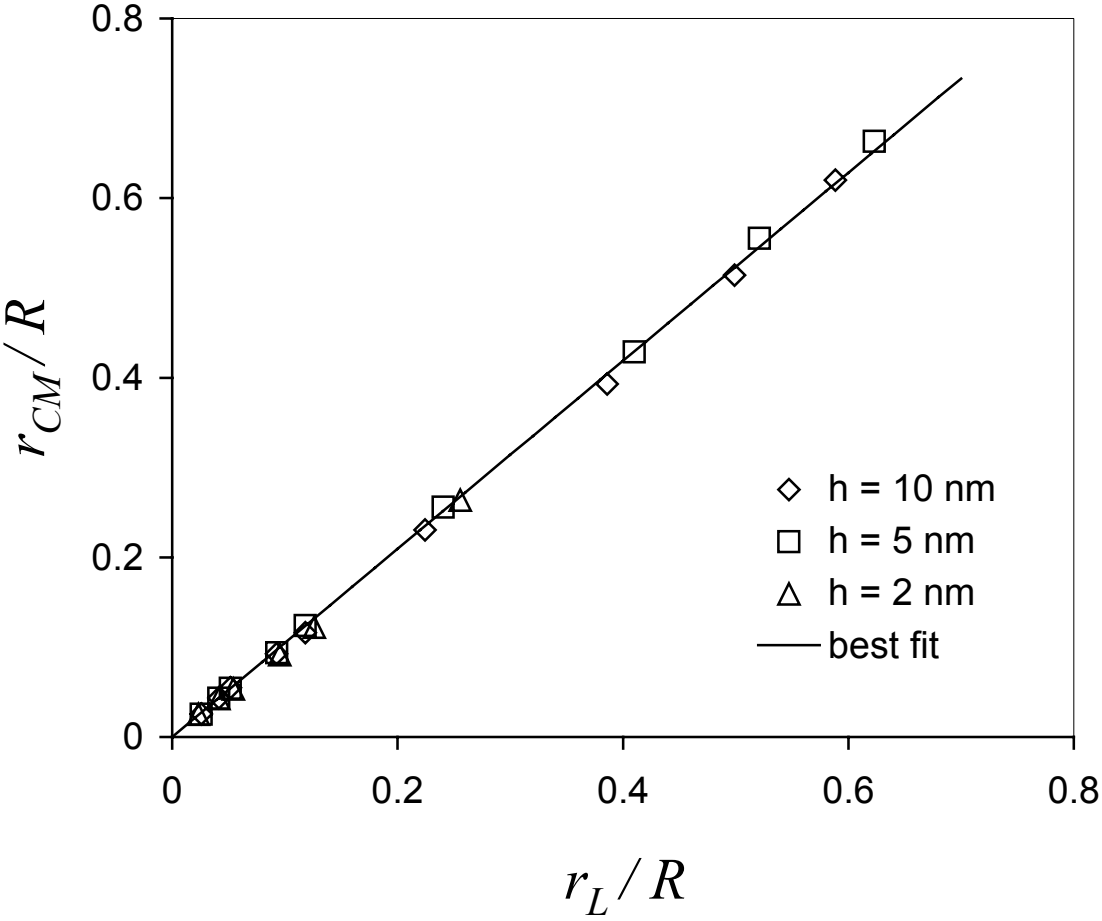

Figure 2.5 Normalized radius of real contact area for a layered medium with different layer thickness.

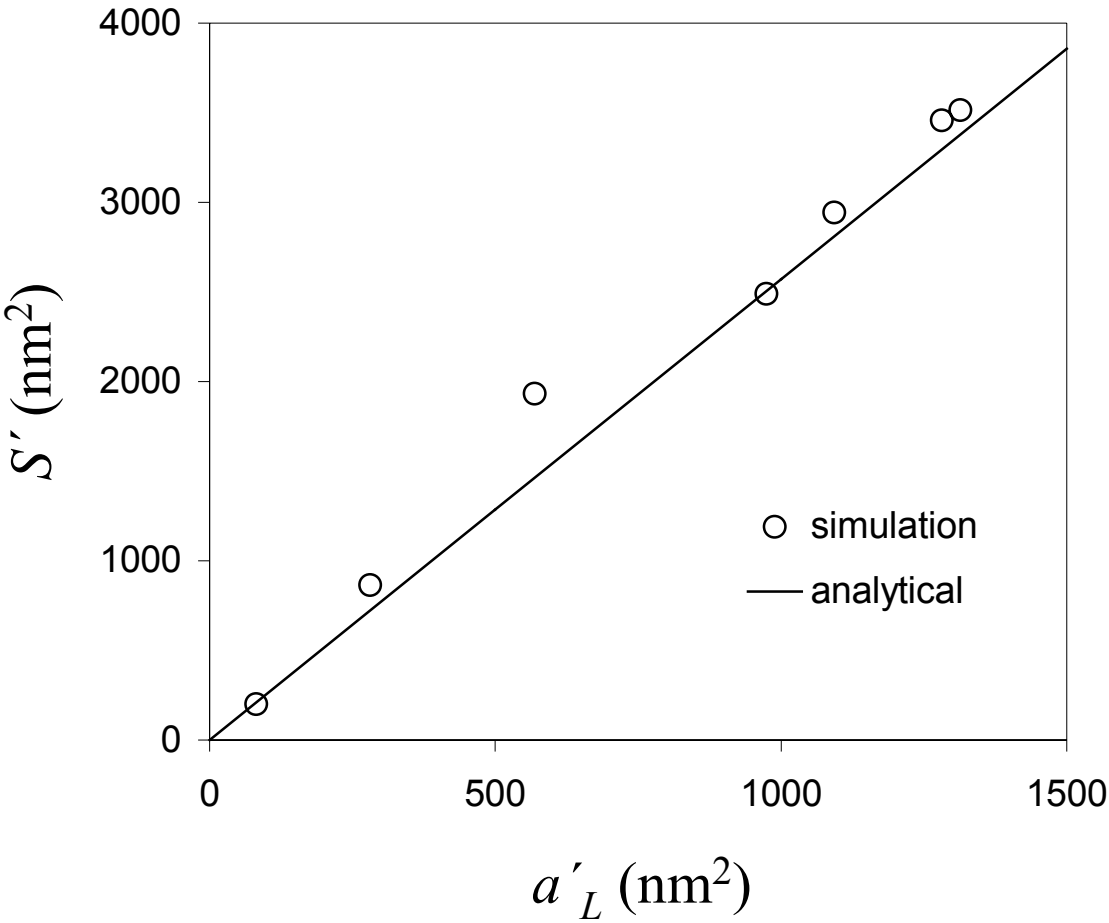

Figure 2.6 Comparison of analytical and simulation results for the truncated total contact area versus largest truncated microcontact area.

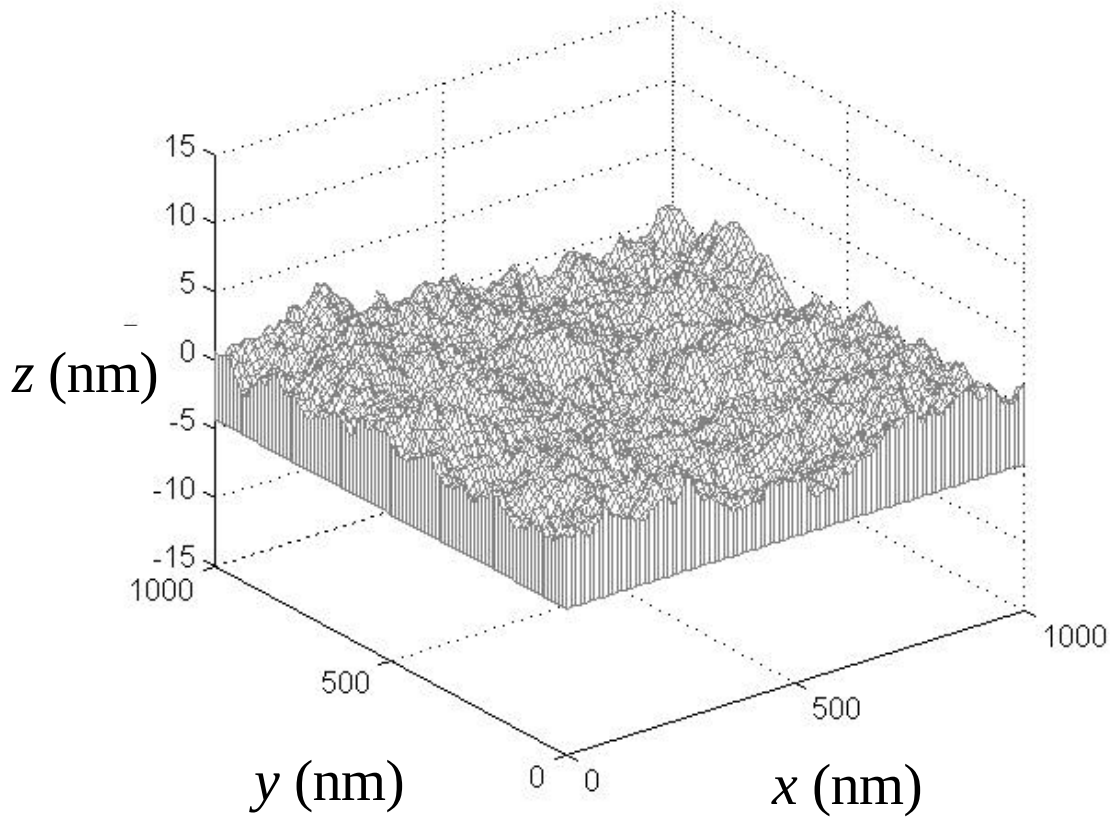

Figure 2.7 Simulated three-dimensional fractal surface equivalent to the head-disk interface (D = 2.44, $G = 9.46 \times 10^{-13}$ m, M = 10, g = 1.5, and L = 1 μm).

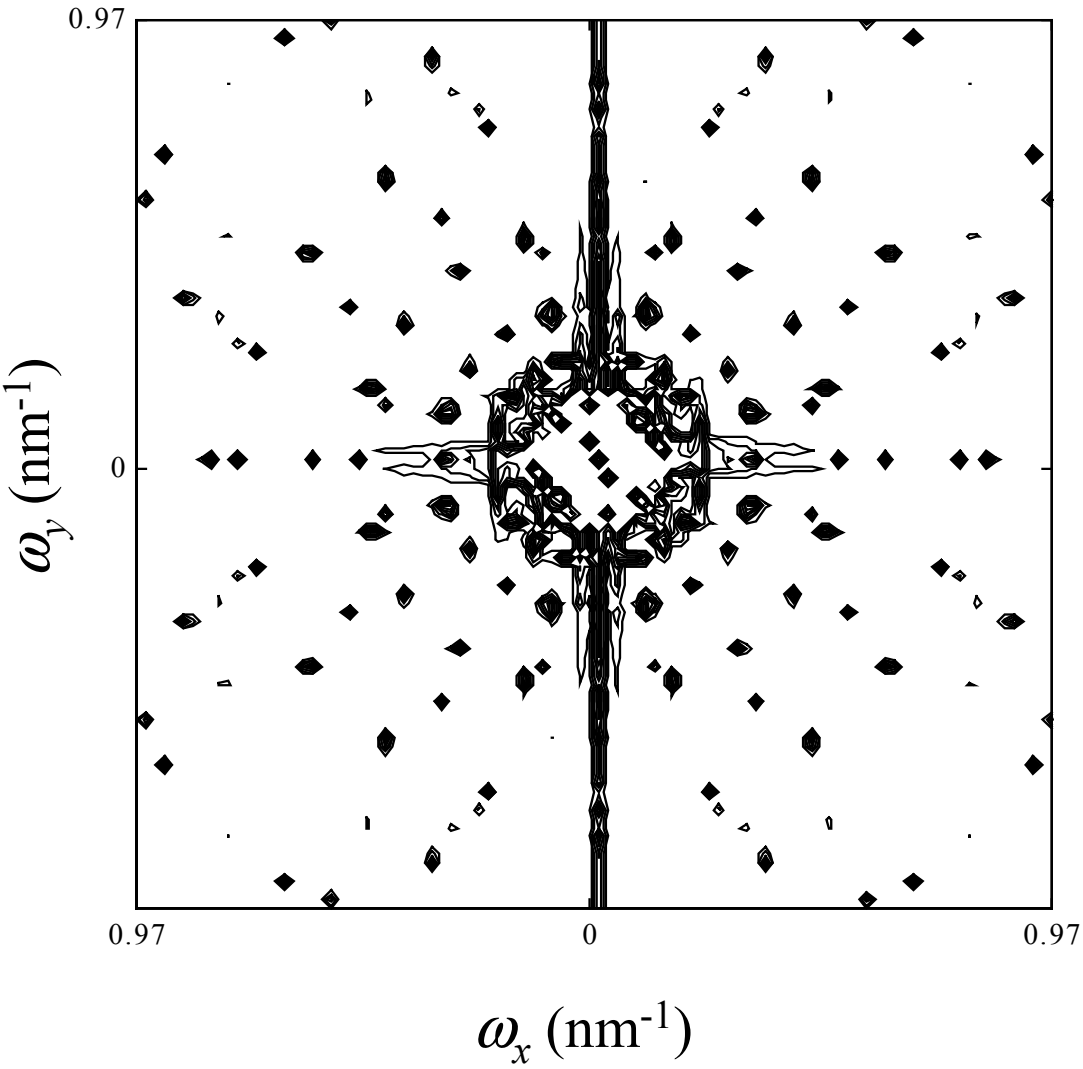

Figure 2.8 Power spectrum of the fractal surface shown in Fig. 2.7.

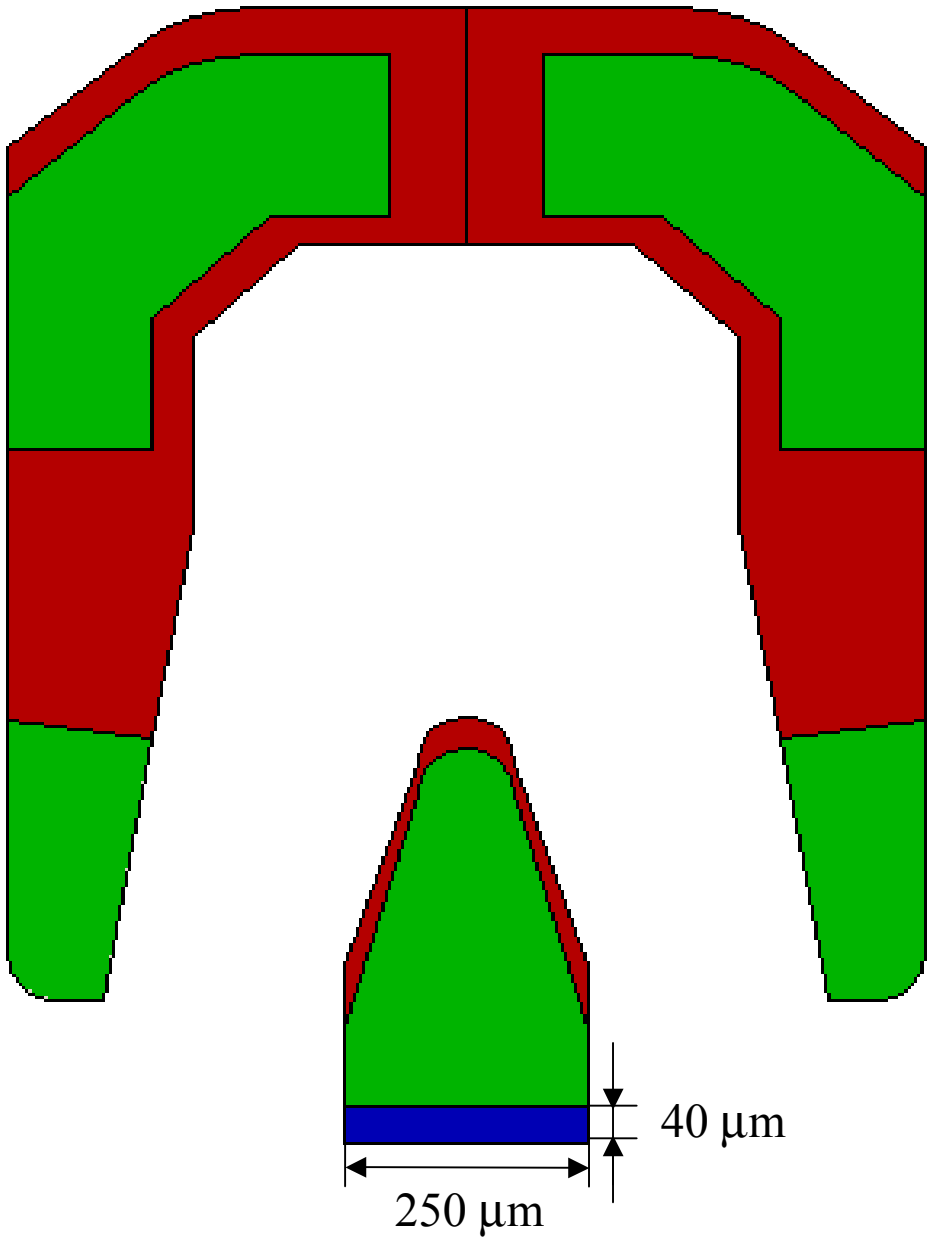

Figure 2.9 Schematic of a tri-pad picoslider showing the apparent contact area at the trailing edge of the center-pad used in the surface contact simulations.

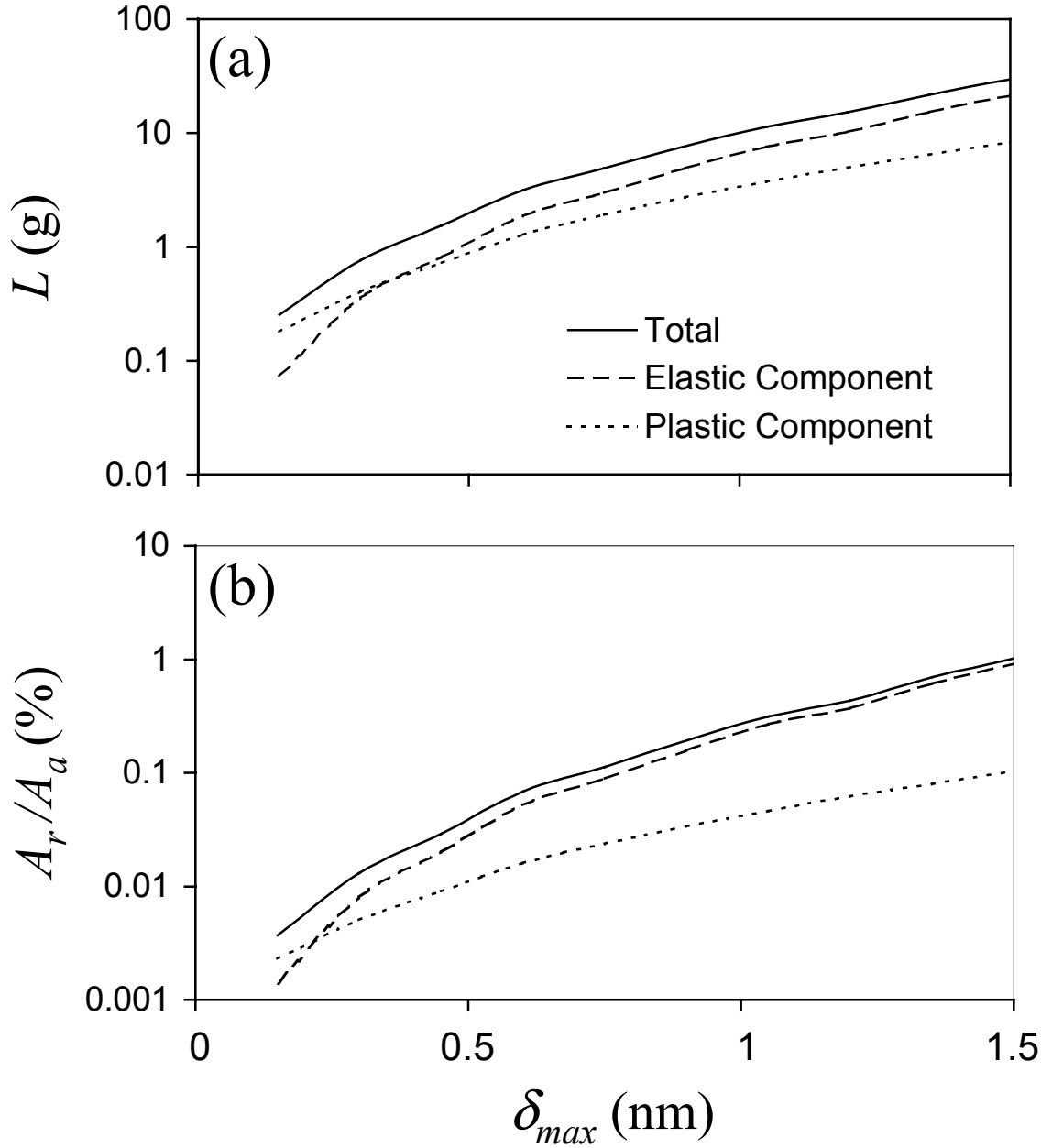

Figure 2.10 (a) Contact load and (b) ratio of real to apparent contact area versus maximum surface interference for a homogeneous medium with carbon overcoat material properties (D = 2.44, $G = 9.46 \times 10^{-13}$ m, M = 10, γ= 1.5, and L = 1 μm).

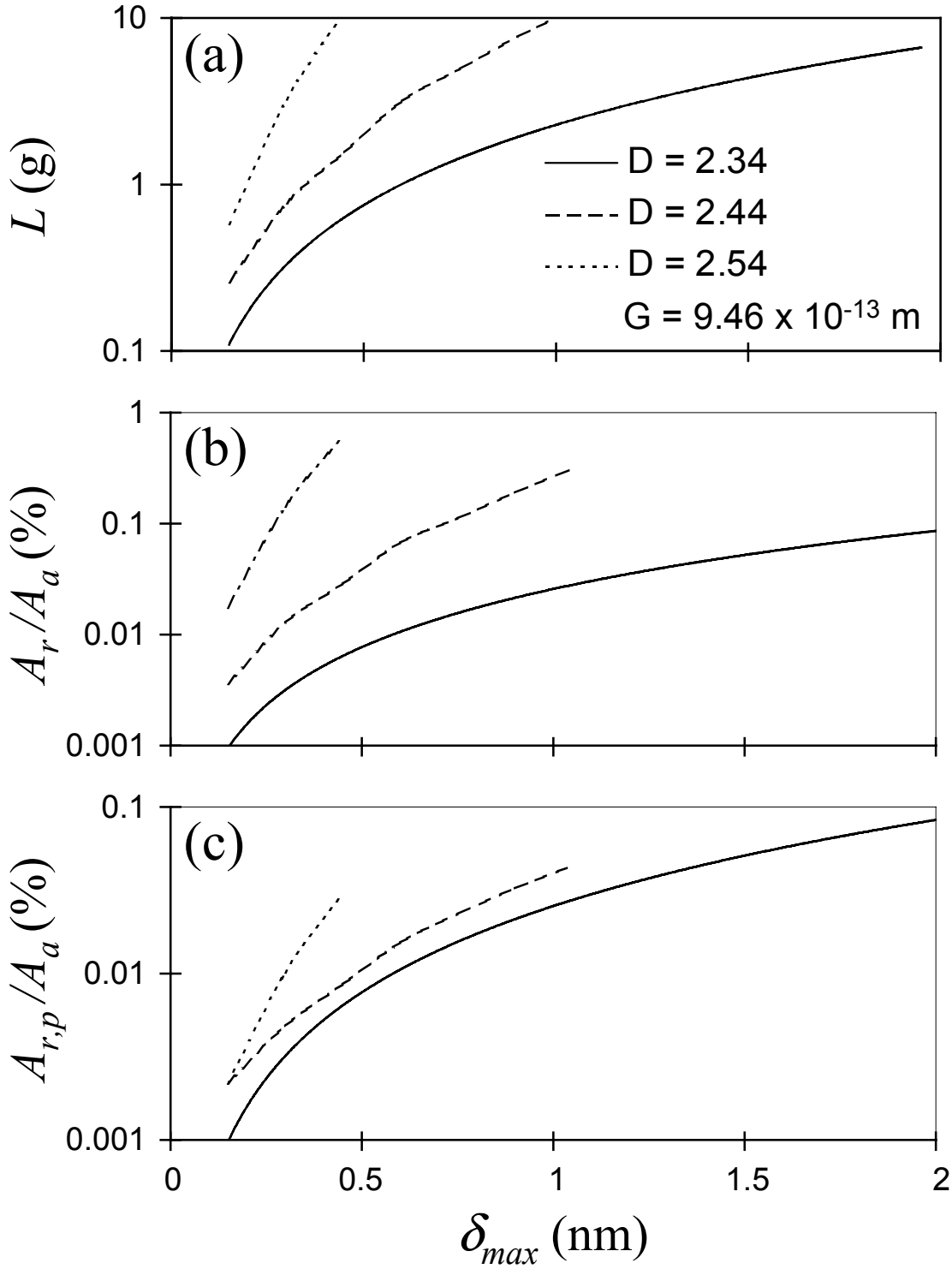

Figure 2.11 Effect of fractal dimension D on (a) contact load, (b) ratio of real to apparent contact area, and (c) ratio of inelastic portion of real contact area to apparent contact area versus maximum surface interference distance for a homogeneous medium with carbon overcoat material properties ($G = 9.46 \times 10^{-13}$ m, $M = 10$, $\gamma = 1.5$, and $L = 1$ μm).

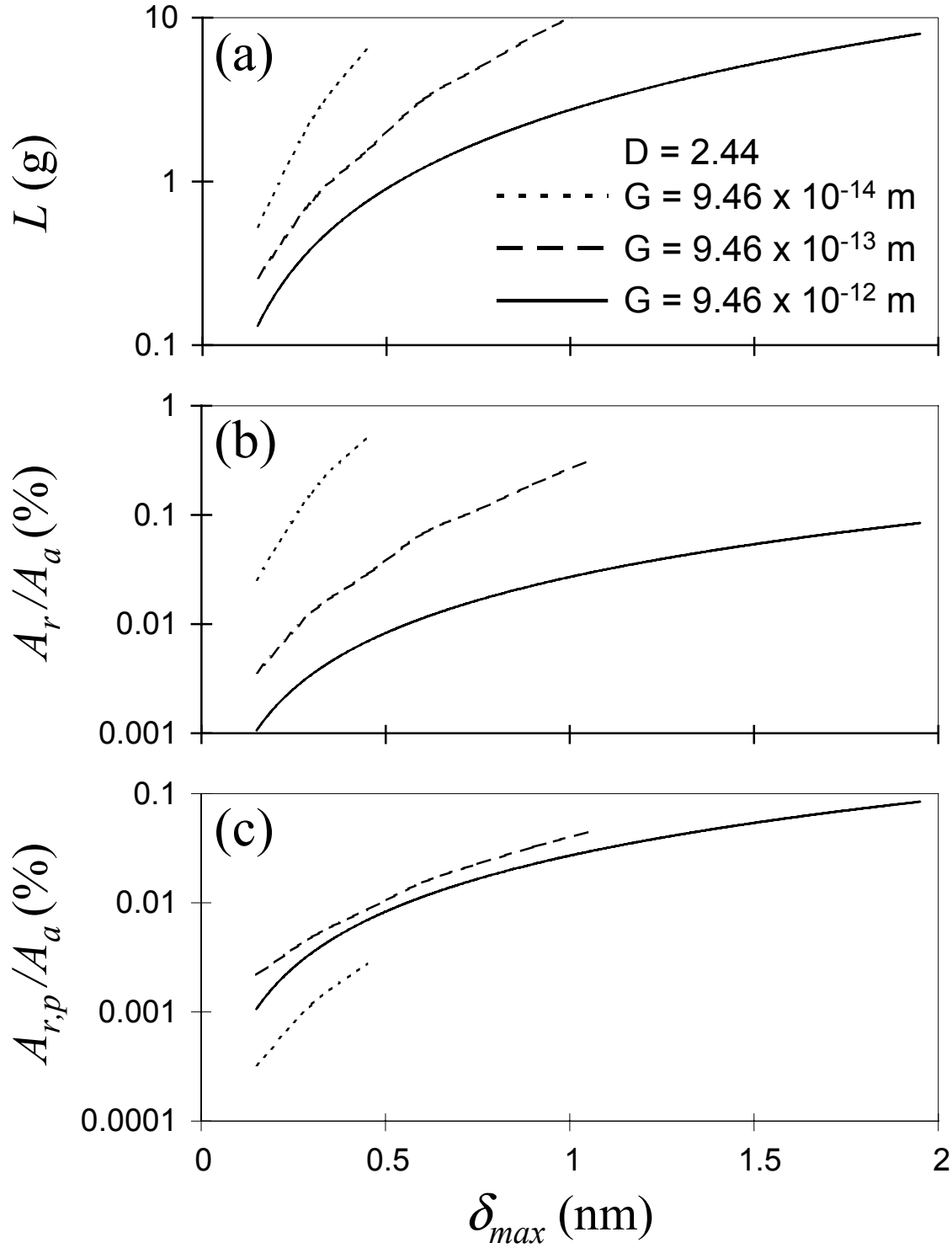

Figure 2.12 Effect of fractal roughness G on (a) contact load, (b) ratio of real to apparent contact area, and (c) ratio of inelastic portion of real contact area to apparent contact area versus maximum surface interference distance for a homogeneous medium with carbon overcoat material properties (D = 2.44, M = 10, γ= 1.5, and L = 1 μm).

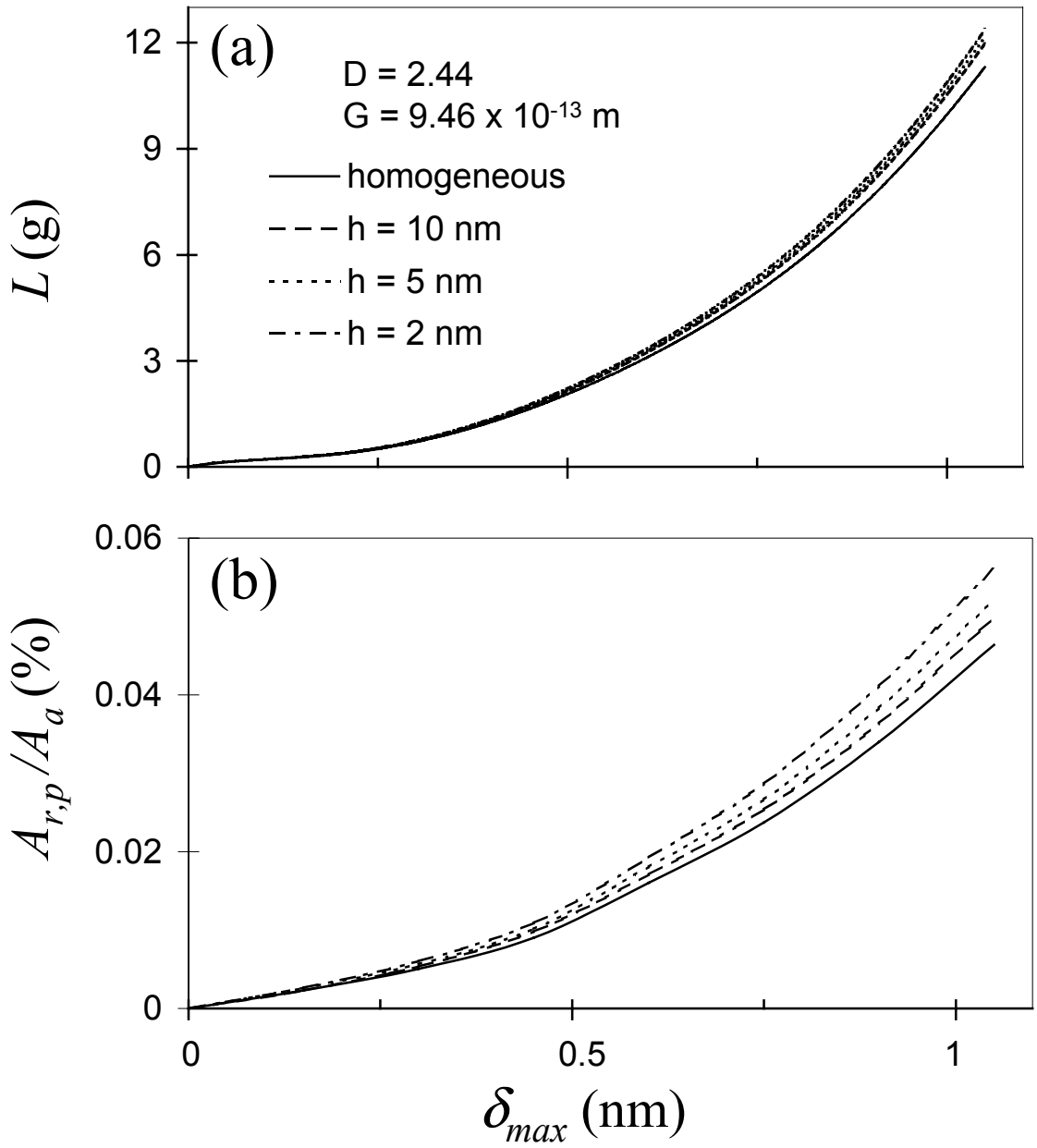

Figure 2.13 (a) Contact load and (b) ratio of inelastic portion of real contact area to apparent contact area versus maximum surface interference for a homogeneous medium with carbon overcoat material properties and a layered medium consisting of a carbon overcoat with thickness 2, 5, and 10 nm and a substrate with magnetic medium material properties (D = 2.44, G = 9.46 × 10^{-13} m, M = 10, γ= 1.5, and L = 1 μm).

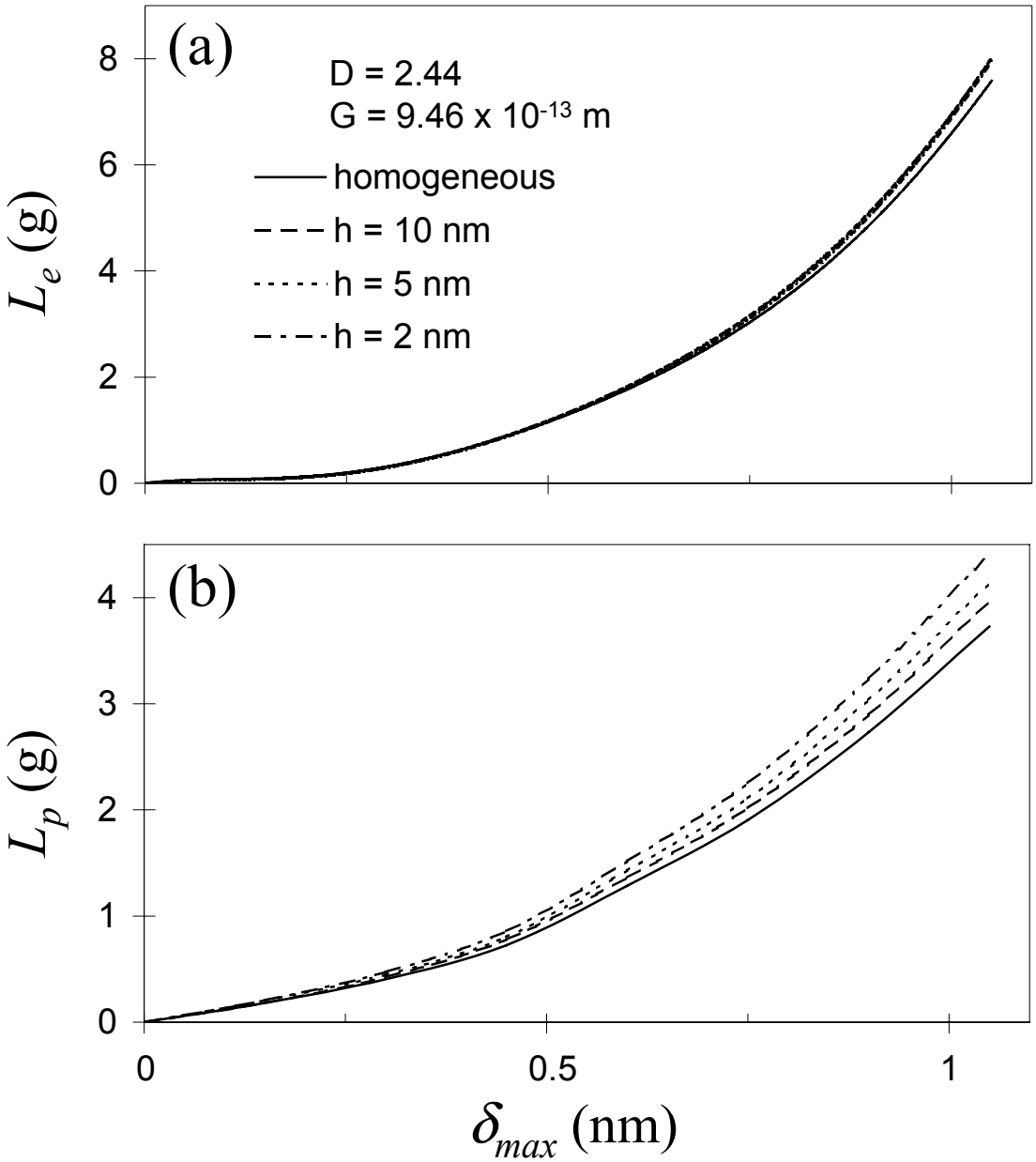

Figure 2.14 (a) Elastic and (b) plastic (including both elastic-plastic and fully plastic) contact load components versus maximum surface interference for a homogeneous medium with carbon overcoat material properties and a layered medium consisting of a carbon overcoat with thickness 2, 5, and 10 nm and a substrate with magnetic medium material properties (D = 2.44, G = 9.46 × 10^{-13} m, M = 10, γ= 1.5, and L = 1 μm).

CHAPTER 3

ELASTIC-PLASTIC FINITE ELEMENT ANALYSIS FOR THE HEAD-DISK INTERFACE WITH FRACTAL TOPOGRAPHY DESCRIPTION

3.1 Introduction

Intimate contact between asperities on countersurfaces at average distances of the order of the equivalent surface roughness controls the magnitudes of the coefficient of friction and wear rate of sliding systems. Knowledge of the resulting deformation at asperity microcontacts is of paramount importance to the reliability of various mechanical components, in particular those used in leading-edge technologies, such as information storage and microdynamic devices, where stringent design requirements prohibit high friction and generation of wear debris.

Emerging demands for even higher magnetic recording densities have led to the evolution of nearly contact (proximity) recording, achieved by reducing the effective distance between the read/write element embedded at the trailing edge of the head and the magnetic layer of the rigid disk. This requires a very low flying height (< 10 nm) and ultrathin overcoats of thickness in the range of ~2-10 nm. At such low flying heights and excessive shear rates caused by high rotational speeds (~20000 rpm), intermittent asperity interactions are inevitable, and the very small thickness of the protective carbon overcoat increases the probability of plastic deformation at the head-disk interface. Consequently, knowledge of the effects of the interfacial topography and the overcoat thickness, material properties, and residual stress (resulting from energetic ion bombardment of the growing

film during sputtering) on the contact stress and strain fields of asperity microcontacts is critical to the endurance of high-density disk drives.

Since the seminal work of Hertz (1882) on frictionless, nonconforming, elastic half-spaces undergoing small deformation due to normal contact, significant progress in contact mechanics has occurred mainly due to major advances in numerical techniques (e.g., finite element method), surface imaging, and computational efficiency. Early progress in contact mechanics has been motivated by problems encountered in large-scale engineering applications, such as railways, bearings, and seals, with most of the studies dealing with homogeneous and isotropic solids subjected to a diversified range of contact conditions (Johnson, 1985). Asymptotic solutions for contact situations involving thin or thick layers, rigid indenters, and moving surface loads have been reported in several early contact mechanics studies (Meijers, 1968; Alblas and Kuipers, 1970; Hardy et al., 1971; Ling and Lai, 1980).

The advent of high-resolution microprobe instruments and microscopy techniques and the development of efficient computational algorithms have enabled incorporation of more realistic topographies and boundary conditions in contact mechanics analyses of rough surfaces. The first study to incorporate roughness effects in contact analysis is that of Greenwood and Williamson (1966), who developed a statistical model that accounts for the height distribution of asperities and elastic-plastic deformation. However, the dependence of various moments of the surface height distribution, such as root-mean-square, skewness, and kurtosis, on the sample length and instrument resolution, demonstrates the need for scale-independent parameters for reliable surface characterization. Such limitations were overcome in recent contact analyses using fractal

geometry to describe the surface topography of both homogeneous half spaces (Majumdar and Tien, 1990; Majumdar and Bhushan, 1991; Wang and Komvopoulos, 1994a, 1994b, 1995; Yan and Komvopoulos, 1998) and layered media (Komvopoulos and Ye, 2001). These studies have provided valuable insight into the evolution of the real contact area, mode of deformation at asperity microcontacts, and interfacial temperature rise due to frictional heating. However, information about the subsurface stress and strain fields was not obtained, apparently due to the difficulty to tackle such complex contact problems analytically.

The objective of this study was to introduce an elastic-plastic finite element model that accounts for the actual topographies of magnetic recording head and rigid disk media characterized by fractal geometry. Finite element results for the subsurface stresses and evolution of plasticity in layered media are presented to elucidate the effects of surface topography and overcoat thickness, material properties, and residual stress.

3.2 Surface Characterization

The use of scale-independent parameters, such as the scale-invariant parameters used in fractal geometry (Mandelbrot, 1983), for topography characterization is especially advantageous since it provides the means for overcoming instrument resolution effects on the measurement of surface topography parameters. In previous two-dimensional contact mechanics analyses of rough surfaces exhibiting fractal behavior (Majumdar and Bhushan, 1991; Wang and Komvopoulos, 1994a, 1994b, 1995; Yan and Komvopoulos, 1998), the surface profile was represented by a Weierstrass-Mandelbrot (W-M) function (Majumdar and Tien, 1990) possessing continuity, differentiability, and self-affinity over a range of scale lengths given by

$$z(x) = L\left(\frac{G}{L}\right)^{D-1} \sum_{n=0}^{n_{\max}} \frac{\cos\left(\frac{2\pi g^n x}{L}\right)}{g^{(2-D)n}}, \tag{3.1}$$

where L is the sample length, G is the fractal roughness, D is the fractal dimension ($1 < D < 2$), g is a parameter controlling the density of frequencies in the surface profile (typically, $g = 1.5$ (Yan and Komvopoulos, 1998)), and n is a frequency index with $n_{\max} = \text{int}[\log(L / L_s)/\log g]$, where L_s is a cut-off length. The fractal roughness G is a height scaling parameter independent of frequency. The magnitude of the fractal dimension D determines the contribution of high and low frequency components in the surface function $z(x)$. The function given by Eq. (3.1) is suitable for simulating surface topographies similar to those of actual surfaces from which the fractal parameters D and G have been determined experimentally. The profile represented by function $z(x)$ is a statistically valid representation of an isotropic and homogeneous rough surface.

3.3 Finite Element Model

The head-disk interface is represented by a deformable flat surface in contact with a rigid rough surface having a structure function equal to the sum of the structure functions of the head and disk surfaces. Figure 3.1(a) shows a fractal profile generated from Eq. (3.1) for $G = 9.46 \times 10^{-4}$ nm, $D = 1.44$, $g = 1.5$, $L = 4379$ nm, and L_s equal to six times the carbon lattice dimension. Since the sample length, L, was chosen to be smaller than the upper limit of the sample length for fractal characterization (Wang and Komvopoulos, 1994a; Yan and Komvopoulos, 1998), the entire profile segment shown in Fig. 3.1(a) can be described by fractal geometry. The values of the fractal parameters D and G correspond to a smooth carbon-coated hard disk and an Al_2O_3-TiC slider

(Komvopoulos, 2000). The dashed line shown in Fig. 3.1(a) represents the surface of a truncating rigid plane (or the overcoat undeformed surface in the finite element model).

The finite element method was used to analyze normal contact between a rigid rough surface profile and a semi-infinite layered medium. Since constructing a finite element model of the entire head-disk interface with a high mesh resolution in order to account for the large range of wavelengths comprising the surface profile (Eq. (3.1)) is impractical, a segment of the surface profile was selected after truncating the entire surface profile by a rigid plane, as shown schematically in Fig. 3.1(a), and performing preliminary finite element contact simulations for each segment. For the relatively small range of maximum surface interference investigated (i.e., 0-3 nm), contact occurred only at a few profile segments, which can be analyzed independently due to their relatively large spacing. Since the interference range of the microcontacts is significantly smaller than that of the global interference d_g (due to the elastic deformation of the layered medium), the effect of relatively large wavelengths on the deformation behavior is secondary. Thus, any truncated profile segment of length several orders of magnitude greater than the simulated maximum local interference d can be used in the analysis. This is because all the truncated segments exhibit a similar scale-dependent behavior over the range of contributing wavelengths. In light of these considerations (and also the contact simulations discussed later), the profile segment between x = 3340 nm and x = 3540 nm (Fig. 3.1(b)) was selected for finite element analysis.

The layered medium consists of a carbon overcoat, a CoCrPt magnetic layer, a chromium-rich CrV layer, a NiP underlayer, and an Al-Mg substrate. Preliminary simulation results confirmed that, for the maximum interference distances examined, the

stress field is confined only in the overcoat and the magnetic layer. Consequently, the aluminum substrate was omitted from the finite element model. All layers were assumed to behave as elastic-perfectly plastic materials. The mechanical properties and thickness of each layer are given in Table 3.1. Figure 3.2 shows the mesh corresponding to a 10 nm thick carbon overcoat and a 40 nm thick magnetic layer. The mesh consists of 5395 plane-strain eight-node isoparametric elements with 16622 nodes. The smallest elements on the overcoat surface are squares with sides of 0.625 nm. The nodes of the vertical boundaries were constraint against displacement in the horizontal direction, whereas the nodes of the bottom boundary were constraint against displacement in the vertical direction. The mesh for the 5 nm thick overcoat is identical to that shown in Fig. 3.2. However, for the 2 nm thick carbon overcoat the mesh was refined to include 12063 eight-node isoparametric elements comprising a total of 34337 nodes, with the smallest elements at the surface being squares with 0.25 nm sides. An updated Lagrangian formulation was used to account for geometric nonlinearities due to large displacements. The finite element code ABAQUS was used to perform finite element simulations in 6-10 steps, each consisting of 10-15 increments. The typical computation time for a finite element simulation on a Pentium III 550 workstation was approximately 40000 CPU seconds.

3.4 Results and Discussion

Microcontact evolution over different profile segments (identified by the truncation procedure described previously) is discussed first in light of simulation results for the local contact pressure distribution, p. Figure 3.3 shows formation of microcontacts at different profile segments due to increasing interference (in the range of 0-2 nm) for a

layered medium with a 10 nm thick overcoat, elastic modulus E_1 = 114 GPa, and yield strength s_{Y1}= 5.67 GPa. As the surface interference increases, the local contact pressures intensify and, in some cases, new microcontacts are established at a later stage (e.g., Figs. 3.3(a), 3.3(d), and 3.3(e)). Asperity interaction appears to lower the peak pressure (e.g., Figs. 3.3(c) and 3.3(d)), evidently due to the larger effective radius of curvature at these locations. The figure shows that only a few microcontacts occur in each region, exhibiting similar peak contact pressures (~10 GPa in all segments) and average microcontact sizes at different maximum local surface interference distances. This behavior suggests that each segment experiences a similar deformation history that depends predominantly on the surface microtopography. Thus, while relatively large-scale waviness determines the various profile segments where microcontacts are established, small-scale waviness comprising all high-frequency components of the surface profile controls local contact, i.e., microcontact size and peak pressure distribution, for given material properties and surface interference. Therefore, it may be inferred that each segment should yield a similar deformation history, if subjected to the same range of maximum surface interference. In view of the above results and analysis, the profile segment shown in Fig. 3.1(b) was used to obtain the results presented below.

To examine the effects of the overcoat thickness, material properties, and residual stress on the evolution of subsurface stresses and strains, finite element results for a layered medium in normal contact with a rigid rough surface possessing a topography equivalent to that of the head-disk interface are presented next, followed by results for a layered medium with varying overcoat thickness, material properties, and residual stress. The two horizontal lines shown in all the stress and strain contour plots denote the

C/CoCrPt and CoCrPt/CrV interfaces. Subscripts 1 and 2 are used to distinguish the elastic modulus, E, and yield strength, σ_Y, of the overcoat and the magnetic layer, respectively. Simulation results are presented in terms of the maximum interference distance, d, defined as the maximum penetration depth of the first asperity of the profile segment contacting the layered medium (Fig. 3.1(b)). As mentioned earlier, due to elastic deformation of the layered medium, the local surface interference at asperity microcontacts assumed values significantly less than the specified maximum surface interference distance (typically about 5-10 times less than d).

3.4.1 Evolution of Subsurface Deformation. Figures 3.4-3.6 show contour plots of von Mises equivalent stress, σ_M, and equivalent plastic strain, ε_p, defined as $\varepsilon_p = \int_S \left[\frac{2}{3} d\varepsilon_{ij}^p d\varepsilon_{ij}^p\right]^{1/2}$, where S is the strain path, for overcoat thickness h = 2 nm, E_1/E_2 = 0.88, and σ_{Y1}/σ_{Y2} = 2.12. Hereafter, the overcoat with the former material properties will be referred to as “soft” overcoat. Figure 3.4(a) shows that the stress fields of the asperity microcontacts established at a maximum interference d = 0.5 nm do not interact with each other. While the stress fields exhibit similarities with that of a Hertzian contact, they are slightly asymmetric due to the non-spherical shape of the asperities, and reveal discontinuities at the overcoat interface with the magnetic layer due to differences in the mechanical properties of the overcoat and magnetic layer (Fig. 3.4(c)). The extremely small plastic zone (with a size comparable to that of the smallest finite elements) shown in Fig. 3.4(d) reveals that plasticity initiates in the magnetic layer, very close to the interface with the overcoat, where the material yield point (σ_{Y2} = 2.67 GPa) is first exceeded, in agreement with previous finite element studies of indented layered media

(Komvopoulos, 1989; Kral et al., 1995). The very small maximum equivalent plastic strain (e_p^{max} = 0.033%) suggests that the subsurface stress field in the layered medium for such small interference distance (or light contact load) is essentially elastic.

Figure 3.5(a) shows that increasing the surface interference promoted asperity interactions. The stress fields of the initially established microcontacts intensify and interact with each other, producing higher stresses (Fig. 3.5(c)) and higher plastic strains (Fig. 3.5(d)). While the carbon layer continues to deform elastically (Fig. 3.5(b)), plastic deformation in the magnetic layer increases and the plastic zone grows reaching the interface with the overcoat (Fig. 3.5(d)). At a larger interference, interaction of the microcontact stress fields becomes even more pronounced. In addition, new microcontacts with non-overlapping stress fields are established, as shown in Fig. 3.6(a). The discontinuity of the stress contours at the overcoat/magnetic layer interface due to the material property mismatch is more distinguishable at this interference distance (Fig. 3.6(c)). More importantly, a new plastic zone has been produced below one of the newly established microcontacts (Fig. 3.6(b)). Again, the plastic zones are confined in the magnetic layer, with the maximum plastic strain always occurring at the interface with the overcoat. The subsurface strain fields of the asperity microcontacts shown in Fig. 3.6(b) will be compared with those of microcontacts obtained in other simulations presented in a later section. Therefore, for convenience, the two microcontacts shown in Fig. 3.6(d) are denoted by letters A (left asperity) and B (right asperity).

3.4.2 Effect of Overcoat Thickness. Figures 3.7 and 3.8 show contour plots of von Mises equivalent stress and equivalent plastic strain obtained for h = 5 and 10 nm, respectively, and d = 2 nm, E_1/E_2 = 0.88, and s_{Y1}/s_{Y2} = 2.12. Figures 3.6-3.8 are

contrasted to reveal the effect of the overcoat thickness on the subsurface stresses and deformation fields. A comparison of the stress fields shown in Figs. 3.6(a), 3.7(a), and 3.8(a) suggests that the effect of the overcoat thickness on the distribution and magnitude of the stresses in the overcoat and magnetic layer is marginal. However, increasing the overcoat thickness from 2 to 5 nm promoted plasticity in the carbon layer under asperity B, while deformation in the magnetic layer under the same microcontact is purely elastic (Figs. 3.7(b) and 3.7(d)). In addition, the plastic strain in the magnetic layer under asperity A decreased significantly. For the 10 nm thick overcoat, deformation in the magnetic layer is purely elastic, while in the carbon overcoat plastic deformation commences again under asperity B, where a slightly larger plastic zone and higher maximum plastic strain occur (Figs. 3.8(b) and 3.8(d)) relatively to what was found in the 5 nm thick overcoat simulation case.

The results shown in Figs. 3.6-3.8 demonstrate that microcontacts A and B exhibit detrimental effects on the magnetic layer and overcoat, respectively. This behavior can be explained by considering the effect of the radius of curvature (or contact radius) on the deformation behavior. From the output information of the contact elements on the finite element mesh surface, the microcontact radius of asperities A and B for an interference distance d = 2 nm was found equal to ~3.7 and ~1.7 nm, respectively. Based on geometry considerations, the corresponding radius of curvature was estimated to be equal to 26.4 and 10.2 nm. For a similar interference, the depth of the maximum von Mises equivalent stress obtained from Hertz contact analysis increases with the radius of curvature (or contact radius). Thus, relatively sharp and blunt asperities promote yielding within the overcoat and the magnetic layer, respectively. This finding is also in agreement with the

substrate effect encountered in indentation tests, where extremely sharp tips (typically ~10-20 nm radius of curvature) and very shallow indentations (i.e., indentation depths less than ~10 percent of the overcoat thickness) are required in order to accurately measure the mechanical properties of ultrathin films.

Figures 3.9 and 3.10 provide additional insight into the effect of the overcoat thickness on the deformation behavior of the overcoat and magnetic layer. These figures show the variation of maximum von Mises equivalent stress, $s_M^{\max}$, maximum equivalent plastic strain, $e_p^{\max}$, and maximum first principal stress, $s_1^{\max}$, with maximum local surface interference d for h = 2, 5, and 10 nm, E_1/E_2 = 0.88, and s_{Y1}/s_{Y2} = 2.12. The stress results in each medium have been normalized by the corresponding material yield strength. The equivalent Mises stress and plastic strain yield information about the initiation and evolution of plasticity, whereas the first principal stress reveals the likelihood of cracking in each layer medium. Figure 3.9(a) shows that the thickness effect on the onset of yielding in the overcoat is marginal. For h = 2 nm, the maximum Mises stress and maximum plastic strain occur at the overcoat interface and for h = 5 and 10 nm they occur in the interior of the overcoat. Despite the slightly higher Mises stress in the thinner overcoat, in all cases yielding in the carbon overcoat commences at a similar interference distance (between 1.5 and 2 nm), i.e., the effect of the overcoat thickness on yielding is marginal. However, Fig. 3.10(a) shows that yielding in the magnetic layer depends strongly on the overcoat thickness. The thinner the overcoat, the smaller the critical interference distance at the inception of plasticity. This is also supported by the plastic strain results shown in Figs. 3.9(b) and 3.10(b). The maximum plastic strain in the magnetic layer always occurs at the interface with the overcoat. The results indicate that

decreasing the overcoat thickness enhances plastic flow in the magnetic layer. It is interesting to note that in the case of the 10 nm thick overcoat, plastic deformation in the magnetic layer did not occur (Fig. 3.10(b)). Thus, for the thickness range examined, plastic deformation in the overcoat is only slightly affected, whereas the resistance to plastic flow of the magnetic layer degrades significantly with decreasing overcoat thickness.

In all simulation cases, the maximum first principal stress in the overcoat and the magnetic layer occurred at the contact surface and interface, respectively. Thus, the results for the first principal stress characterize the propensity for cracking at the overcoat surface and its interface with the magnetic layer. While differences between stress results for h = 5 and 10 nm are negligible, a significantly higher tensile stress occurs in the thinner overcoat (h = 2 nm) indicating a greater likelihood for surface microcracking (Fig. 3.9(c)). A similar trend is observed for the magnetic layer, where higher peak tensile stresses occur at the interface of the magnetic layer in the case of the thinner overcoat (Fig. 3.10(c)).

3.4.3 Effect of Overcoat Mechanical Properties. To analyze the effect of the elastic modulus and yield strength (or hardness) of the overcoat on the resulting subsurface deformation, the results shown in Fig. 3.11 for a 5 nm thick overcoat with properties E_1/E_2 = 1.29 and s_{Y1}/s_{Y2} = 4.87 (hereafter referred to as “hard” overcoat) are contrasted with those of the relatively soft overcoat (Fig. 3.7). A comparison of Fig. 3.11(a) with Fig. 3.7(a) and Fig. 3.11(c) with Fig. 3.7(c) shows that, for the same interference distance, the stress distributions exhibit similarities; however, higher stresses were produced in the hard overcoat. An inspection of the equivalent plastic strain contours shown in Figs.

3.7(b), 3.7(d), 3.11(b), and 3.11(d) shows that deformation in the hard overcoat under asperity B is purely elastic, while the plastic strain in the magnetic layer adjacent to the interface with the overcoat has slightly increased. This is due to the higher stress concentration at the interface caused by the greater material property mismatch in the case of the hard layer. Therefore, increasing the overcoat yield strength (or hardness) produces plastic deformation only in the magnetic layer, at the interface with the overcoat.

To demonstrate the significance of the overcoat material properties on the evolution of plasticity and likelihood for microcracking in the layered medium, stress and plastic strain results for both relatively hard (b = 4.9) and soft (b = 2.1) overcoats of the same thickness (h = 5 nm) are cross-plotted in Fig. 3.12 (where b is the ratio of the overcoat hardness to that of the magnetic layer, assuming a proportionality between hardness and yield strength). The stresses in the overcoat and magnetic layer have been normalized by the yield strength of each material. For the hard overcoat case, Fig. 3.12(a) shows that yielding commences only in the magnetic layer, at a critical interference distance of the order of ~1 nm. Although in the case of the soft overcoat yielding occurs in both the overcoat and the magnetic layer, the inception of plasticity in the magnetic layer is encountered at a greater critical interference distance. This implies that yielding in the magnetic layer is promoted with harder and stiffer overcoats, evidently due to the higher interfacial stresses resulting from the increased material property mismatch and stress concentration effects. Figure 3.12(b) shows the development of plasticity in each layered medium. While the hard overcoat deforms only elastically, it induces plastic deformation in the magnetic layer prematurely, as evidenced by the relatively smaller interference at the onset of yielding and the larger plastic strains encountered with

increasing surface interference. Figure 3.12(c) shows a monotonic increase of the normalized maximum tensile stress with increasing interference distance. In view of the different yield strengths of the hard and soft overcoats, it may be concluded that the effect of the overcoat material properties on the maximum tensile stress in the carbon and magnetic layers is rather secondary.

3.4.4 Effect of Overcoat Residual Stress. Sputtering of thin carbon films on magnetic media may lead to the development of a residual stress in the overcoat, depending on the deposition conditions. A uniform biaxial residual stress, s_R, is typically produced in such ultrathin films. In general, a compressive residual stress is considered to be beneficial to the material resistance to plastic deformation and cracking. Thus, to elucidate the effect of the overcoat residual stress on the deformation at the head-disk interface, contact simulations were performed for s_R = 0, –1, –2, and –4 GPa. Contours of von Mises equivalent stress are shown in Fig. 3.13 for a relatively thick and soft overcoat (h = 10 nm, E_1/E_2 = 0.88, s_{Y1}/s_{Y2} = 2.12) under a biaxial residual stress s_R = –2 GPa. A comparison with the results obtained for the same layered medium and s_R = 0 (Fig. 3.8) reveals a significant effect of the compressive residual stress on the resulting stress field. More importantly, plastic deformation in the overcoat under asperity B (Fig. 3.8(d)) did not occur in the presence of the compressive residual stress, i.e., both the overcoat and the magnetic layer deformed elastically. This result supports the conventional notion that a compressive residual stress increases the plastic flow resistance of the overcoat material.

Figures 3.14 and 3.15 show the variation of $s_M^{\max}$, $e_p^{\max}$, and $s_1^{\max}$ with s_R and d in the overcoat and magnetic layer, respectively, for a layered medium with a thick and

soft overcoat (h = 10 nm, E_1/E_2 = 0.88, s_{Y1}/s_{Y2} = 2.12). Regarding yielding and plastic deformation in the overcoat, Figs. 3.14(a) and 3.14(b) reveal the existence of an optimum compressive residual stress that depends on the yield strength of the overcoat material. A high compressive stress (e.g., s_R = –4 GPa) promotes yielding and the development of large plastic strains at interference distances much smaller than those obtained for $s_R = 0$. A significant enhancement of the overcoat resistance against plastic deformation is shown for intermediate residual stress values, especially for s_R = –2 GPa. As expected, the maximum tensile stress decreases in the presence of a biaxial compressive stress (Fig. 3.14(c)). Thus, cracking at the overcoat surface (where the maximum tensile stress occurs in the case of overcoats with such small thickness) is less likely to occur when the overcoat is under a compressive residual stress. Conversely to the overcoat, the residual stress effect on the stress and strain fields in the magnetic layer is negligible (Figs. 3.15(a) and 3.15(b). However, for relatively large interferences (e.g., $d >$ 2.5 nm), a high compressive residual stress increases the magnitudes of both the plastic strain (Fig. 3.15(b)) and the tensile stress at the interface with the overcoat (Fig. 3.15(c)), suggesting that delamination at the interface of the layered medium is another possibility in the presence of a relatively high residual compressive stress in the overcoat.

The present contact analysis represents a general treatment to normal contact of layered media possessing rough surface topographies that can be characterized by fractal geometry. The uniqueness of the outlined approach stems from the combination of fractals and finite element modeling. This enables tracking of elastic-plastic deformation commencing at various length scales. The obtained results and trends should also be applicable to sliding at the head-disk interface, provided the friction coefficient is

relatively low (e.g., ~0.1 or less). However, when the magnitude of the tangential (friction) traction at asperity microcontacts is significant, the analysis must be modified to account for the effect of friction on the resulting deformation in the overcoat and magnetic layer. This can be easily accomplished by specifying the desired friction coefficient value to the contact elements of the finite element mesh. Results for the stress/strain field due to sliding at the head-disk interface will be presented in future publications dealing with friction of fractal surfaces.

3.5 Conclusions

A finite element model that accounts for the actual surface topographies (characterized by fractal geometry) and elastic-plastic material properties of the different layers in a thin-film disk was used to study deformation at the head-disk interface. Based on the presented results and discussion, the following main conclusions can be drawn.

(1) For the range of maximum surface interference examined (i.e., 0-3 nm), contact comprises mostly isolated asperity microcontacts at a few regions of the contact interface. This is controlled by characteristic surface topography parameters (i.e., fractal dimension D and fractal roughness G). Due to the dominant effect of high-frequency components in the surface profile on microcontact formation, the evolution of deformation in these regions exhibits similarities. Thus, the analysis can be carried over a contact segment of the surface profile containing all the contributing small wavelengths.

(2) The stress and strain fields are confined within the carbon overcoat and the magnetic layer. The asperity shape (or effective radius of curvature) controls plastic deformation in the overcoat and magnetic layer. Relatively sharp asperities induce plasticity in the overcoat just below the microcontact region (thick overcoats, h = 10 nm)

or at the interface with the magnetic layer (thin overcoats, h = 2 nm), while asperities with a relatively large radius of curvature promote plastic flow only in the magnetic layer, at the interface with the overcoat.

(3) For the ranges of overcoat thickness (h = 2, 5, and 10 nm) and material properties (E_1/E_2 = 0.88 and 1.29, and s_{Y1}/s_{Y2} = 2.12 and 4.87) examined in this study, the maximum tensile stress in the overcoat and the magnetic layer occurs at the surface and the interface, respectively.

(4) Plastic deformation and the likelihood of cracking due to a high tensile stress at the overcoat surface and the interface with the magnetic layer are both enhanced with decreasing overcoat thickness.

(5) Although stiffer and harder overcoats exhibit higher resistance to plastic deformation and surface cracking, they promote plasticity in the magnetic layer, at the interface with the overcoat.

(6) A compressive residual stress in the overcoat exhibits a profound effect on the plastic flow resistance of the overcoat; however, its effect on the deformation in the magnetic layer is secondary. An optimum compressive residual stress exists, which depends on the overcoat yield strength. For a 10 nm thick carbon overcoat of elastic modulus and yield strength equal to 114 and 5.67 GPa, respectively, the optimum compressive residual stress is equal to about –2 GPa.

Table 3.1. Thickness and mechanical properties of different layers used in the finite element model.

Layer	Thickness (nm)	Elastic modulus (GPa)	Yield strength (GPa)
C	2, 5, 10	114	5.67
		168	13.0
CoCrPt	15.6, 40, 45	130	2.67
CrV	100	140	2.58
NiP	420	160	2.67

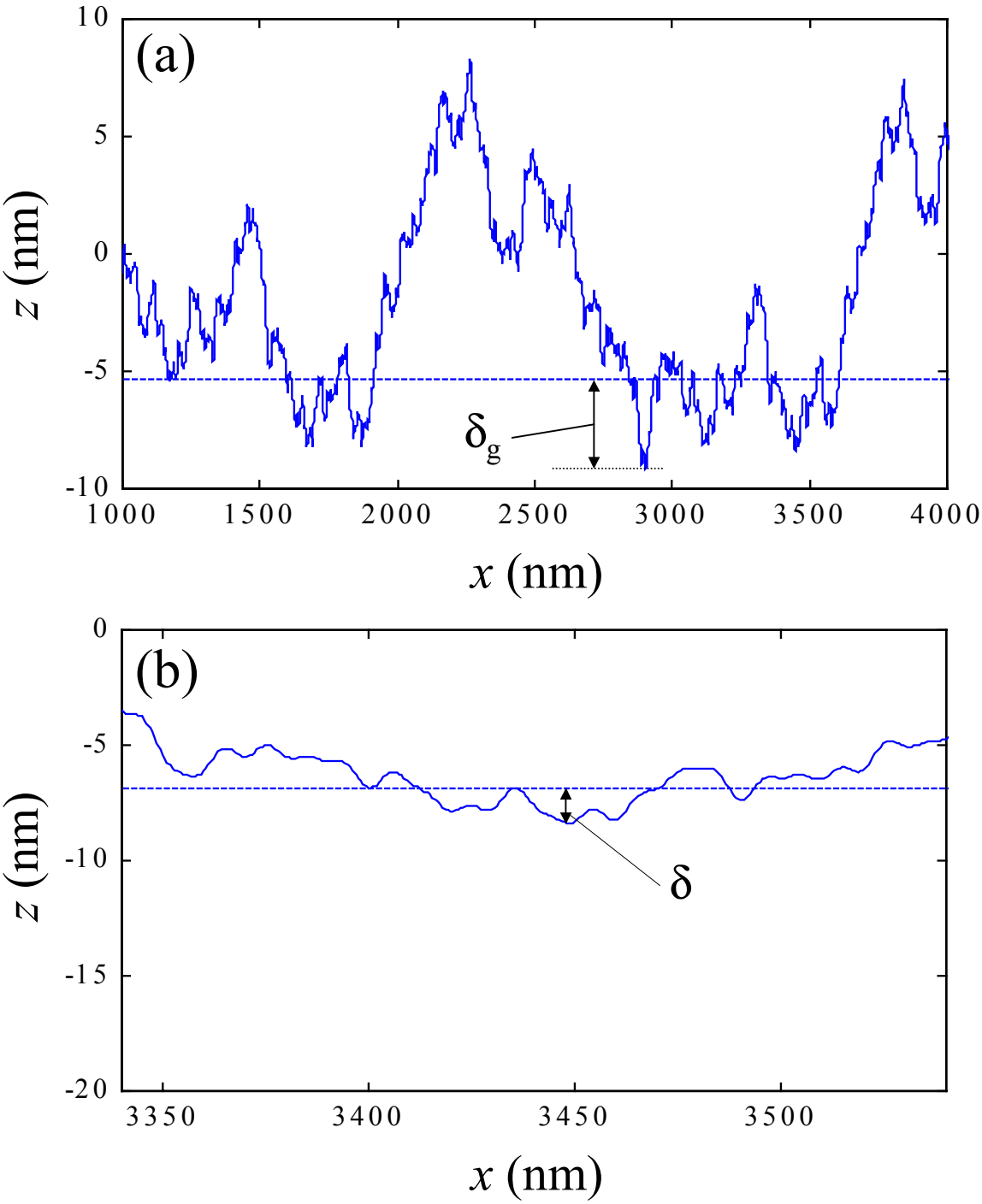

Figure 3.1 (a) Surface profile equivalent to the head-disk interface truncated by a rigid plane to a maximum global interference δ_g revealing contact at different regions and (b) profile region between x = 3340 nm and x = 3540 nm truncated by a rigid plane to a maximum local interference δ used in the finite element simulations.

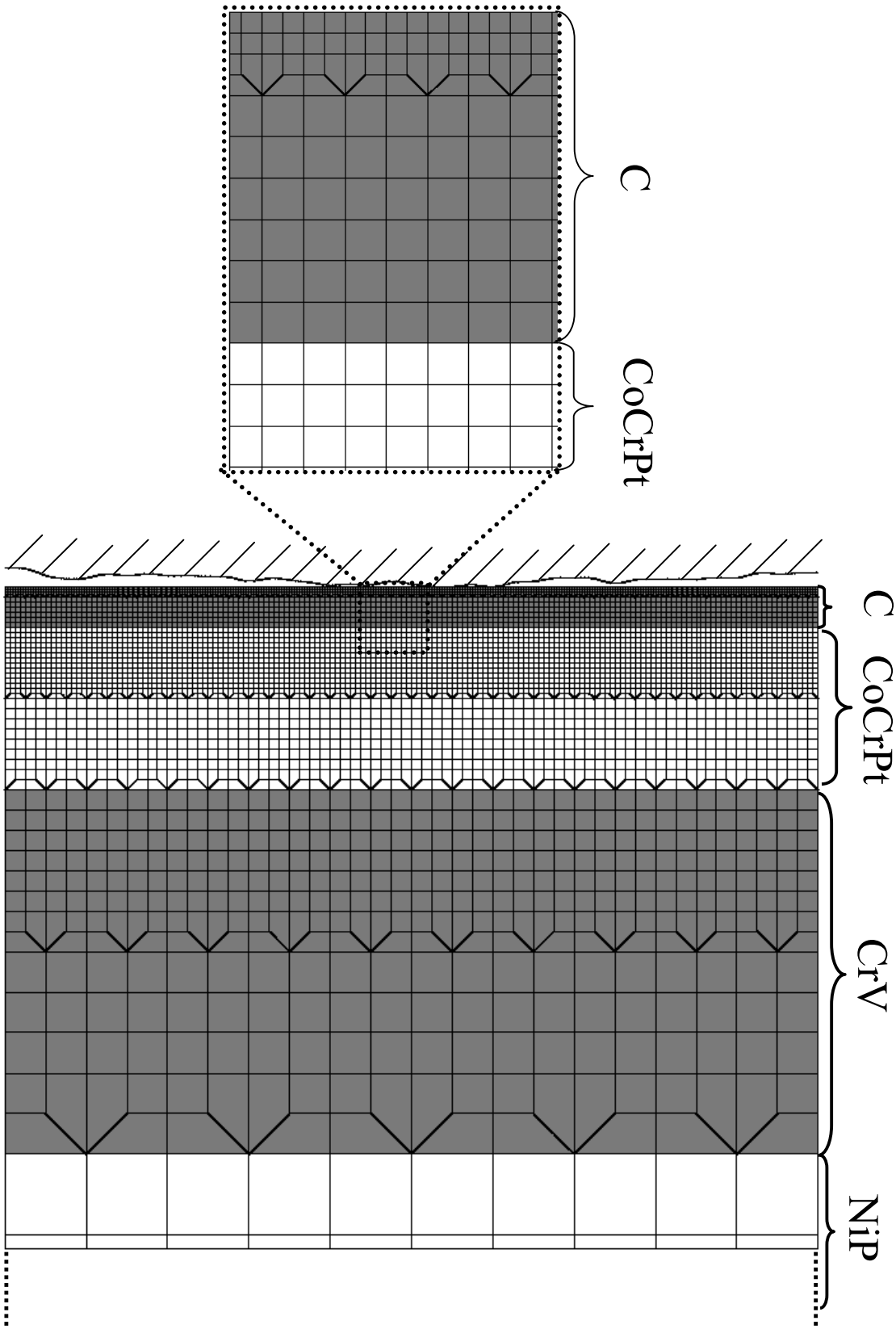

Figure 3.2 Finite element mesh of a layered medium with a 10 nm thick overcoat.

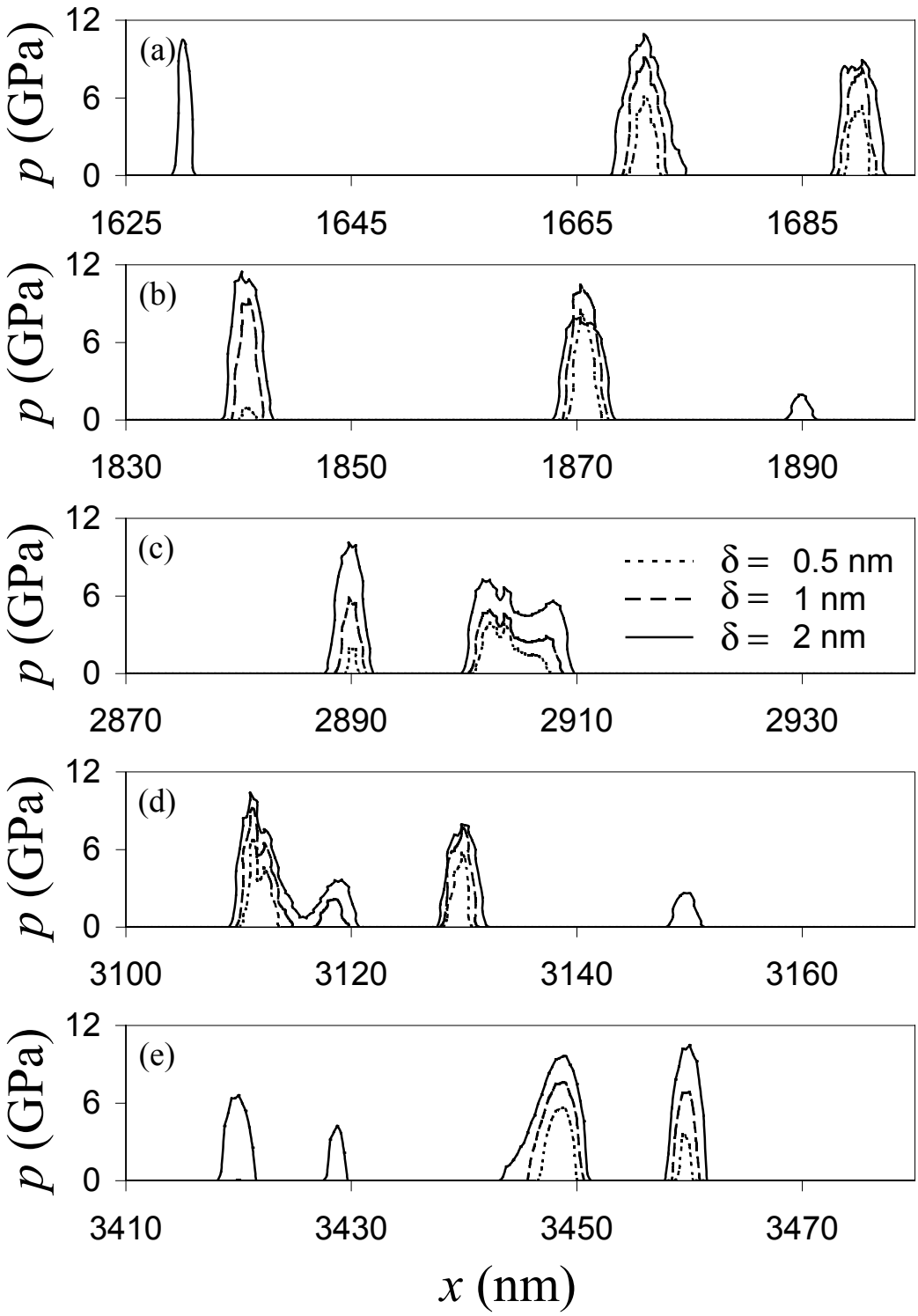

Figure 3.3 Evolution of contact pressure distributions at different regions of the surface profile shown in Figure 1(a) with increasing surface interference for h = 2 nm, E_1/E_2 = 0.88, and σ_{Y1}/σ_{Y2} = 2.12.

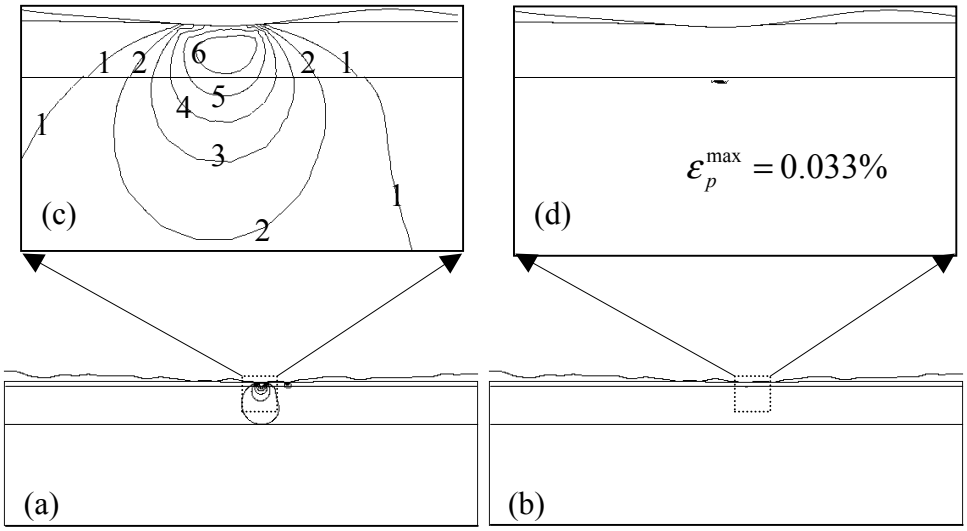

σ_M (GPa):

(1) 0.46	(4) 1.85
(2) 0.93	(5) 2.32
(3) 1.39	(6) 2.78

ε_p (%):

(1) 0.005	(4) 0.022
(2) 0.011	(5) 0.027
(3) 0.016	(6) 0.033

Figure 3.4 Contours of (a), (c) von Mises equivalent stress and (b), (d) equivalent plastic strain for δ = 0.5 nm, h = 2 nm, E_1/E_2 = 0.88, and σ_{Y1}/σ_{Y2} = 2.12.

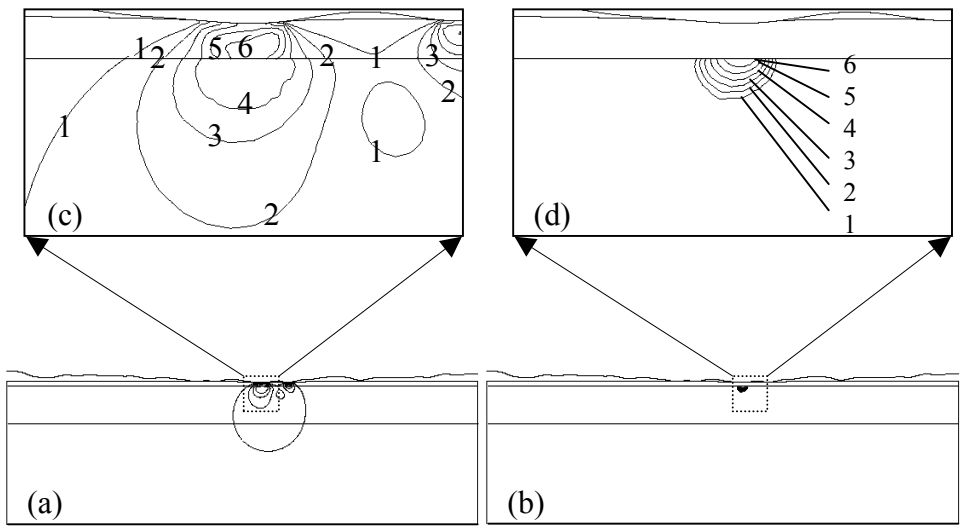

σ_M (GPa):

(1) 0.64	(4) 2.54
(2) 1.27	(5) 3.18
(3) 1.91	(6) 3.81

ε_p (%):

(1) 0.30	(4) 1.21
(2) 0.61	(5) 1.51
(3) 0.91	(6) 1.82

Figure 3.5 Contours of (a), (c) von Mises equivalent stress and (b), (d) equivalent plastic strain for δ = 1 nm, h = 2 nm, E_1/E_2 = 0.88, and σ_{Y1}/σ_{Y2} = 2.12.

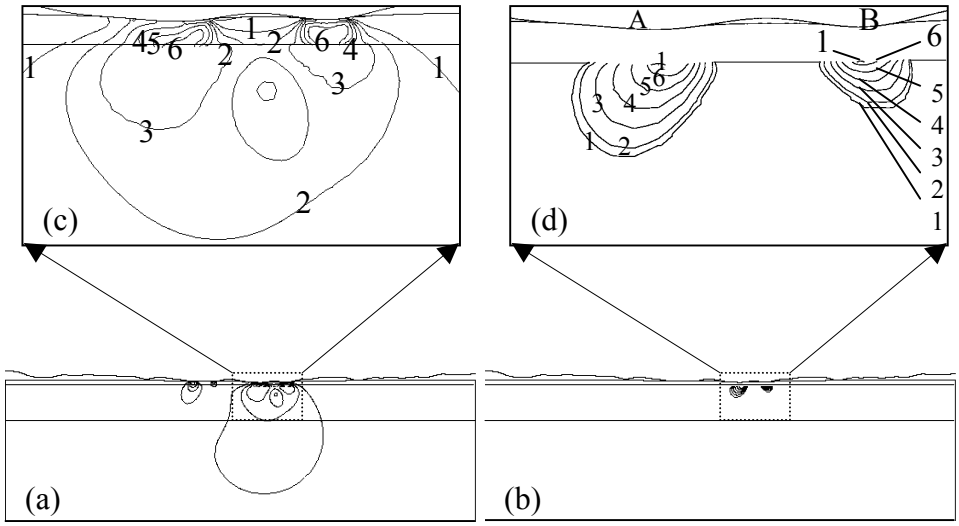

σ_M (GPa):

(1) 0.82	(4) 3.27
(2) 1.64	(5) 4.08
(3) 2.45	(6) 4.90

ε_p (%):

(1) 0.30	(4) 2.08
(2) 0.60	(5) 2.81
(3) 1.34	(6) 3.55

Figure 3.6 Contours of (a), (c) von Mises equivalent stress and (b), (d) equivalent plastic strain for $\delta = 2$ nm, $h = 2$ nm, $E_1/E_2 = 0.88$, and $\sigma_{Y1}/\sigma_{Y2} = 2.12$.

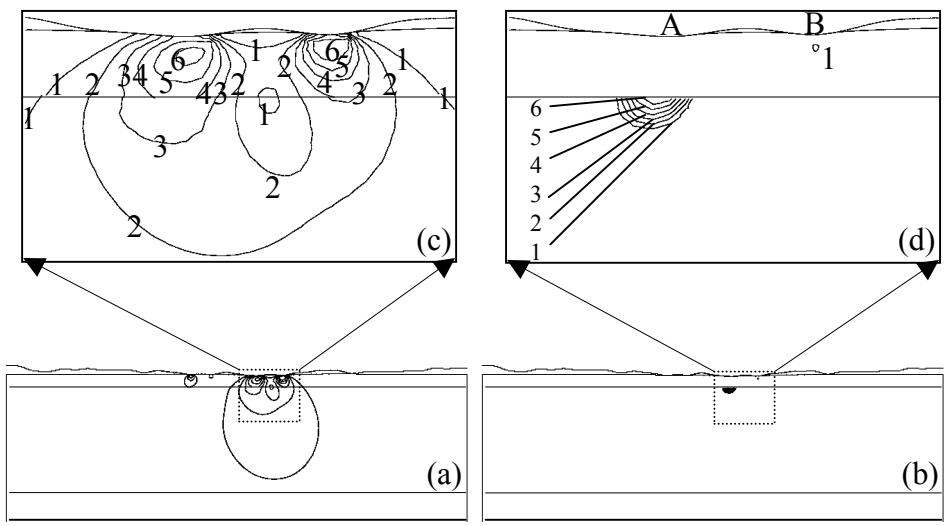

σ_M (GPa):

(1) 0.83	(4) 3.30
(2) 1.65	(5) 4.13
(3) 2.48	(6) 4.95

ε_p (%):

(1) 0.20	(4) 0.78
(2) 0.39	(5) 0.98
(3) 0.59	(6) 1.17

Figure 3.7 Contours of (a), (c) von Mises equivalent stress and (b), (d) equivalent plastic strain for $\delta = 2$ nm, $h = 5$ nm, $E_1/E_2 = 0.88$, and $\sigma_{Y1}/\sigma_{Y2} = 2.12$.

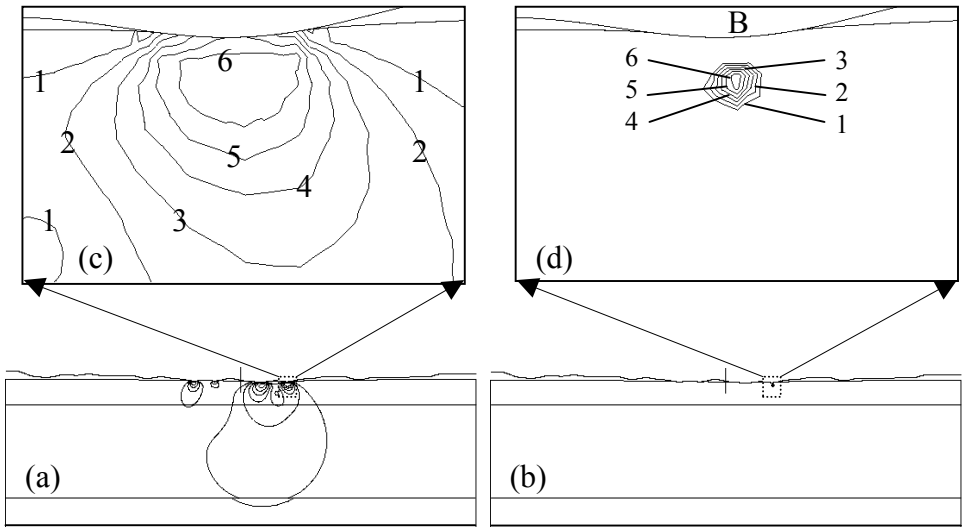

σ_M (GPa):

(1) 0.82	(4) 3.28
(2) 1.64	(5) 4.10
(3) 2.46	(6) 4.93

ε_p (%):

(1) 0.04	(4) 0.16
(2) 0.08	(5) 0.19
(3) 0.12	(6) 0.23

Figure 3.8 Contours of (a), (c) von Mises equivalent stress and (b), (d) equivalent plastic strain for $\delta = 2$ nm, $h = 10$ nm, $E_1/E_2 = 0.88$, and $\sigma_{Y1}/\sigma_{Y2} = 2.12$.

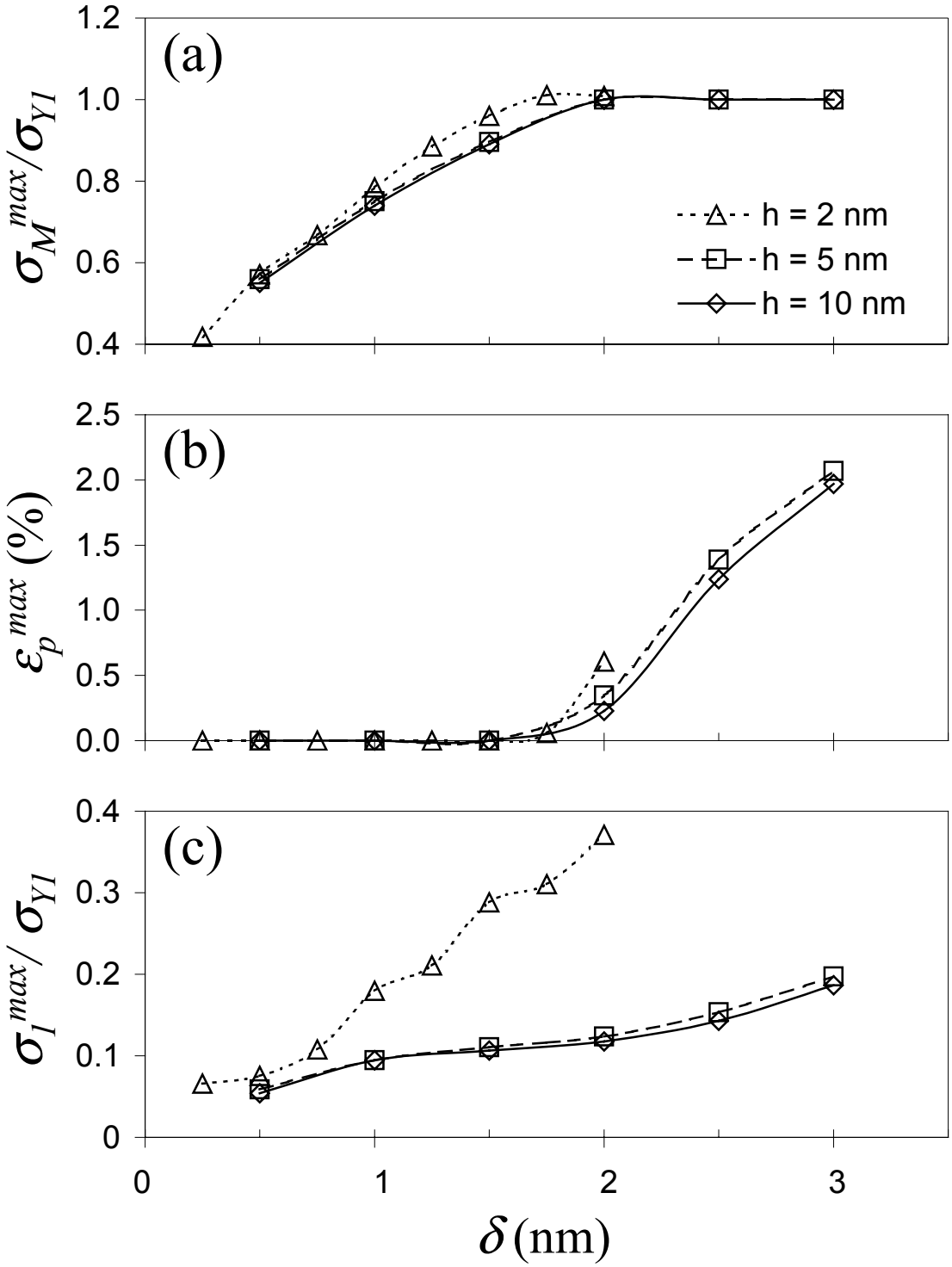

Figure 3.9 Variation of (a) maximum von Mises equivalent stress, σ_M^{max}, (b) maximum equivalent plastic strain, ε_p^{max}, and (c) maximum first principal stress, , with maximum local surface interference δ in the overcoat medium for h = 2, 5, and 10 nm, E_1/E_2 = 0.88, and σ_{Y1}/σ_{Y2} = 2.12. (Stress results have been normalized by the yield strength of the overcoat, σ_{Y1}.)

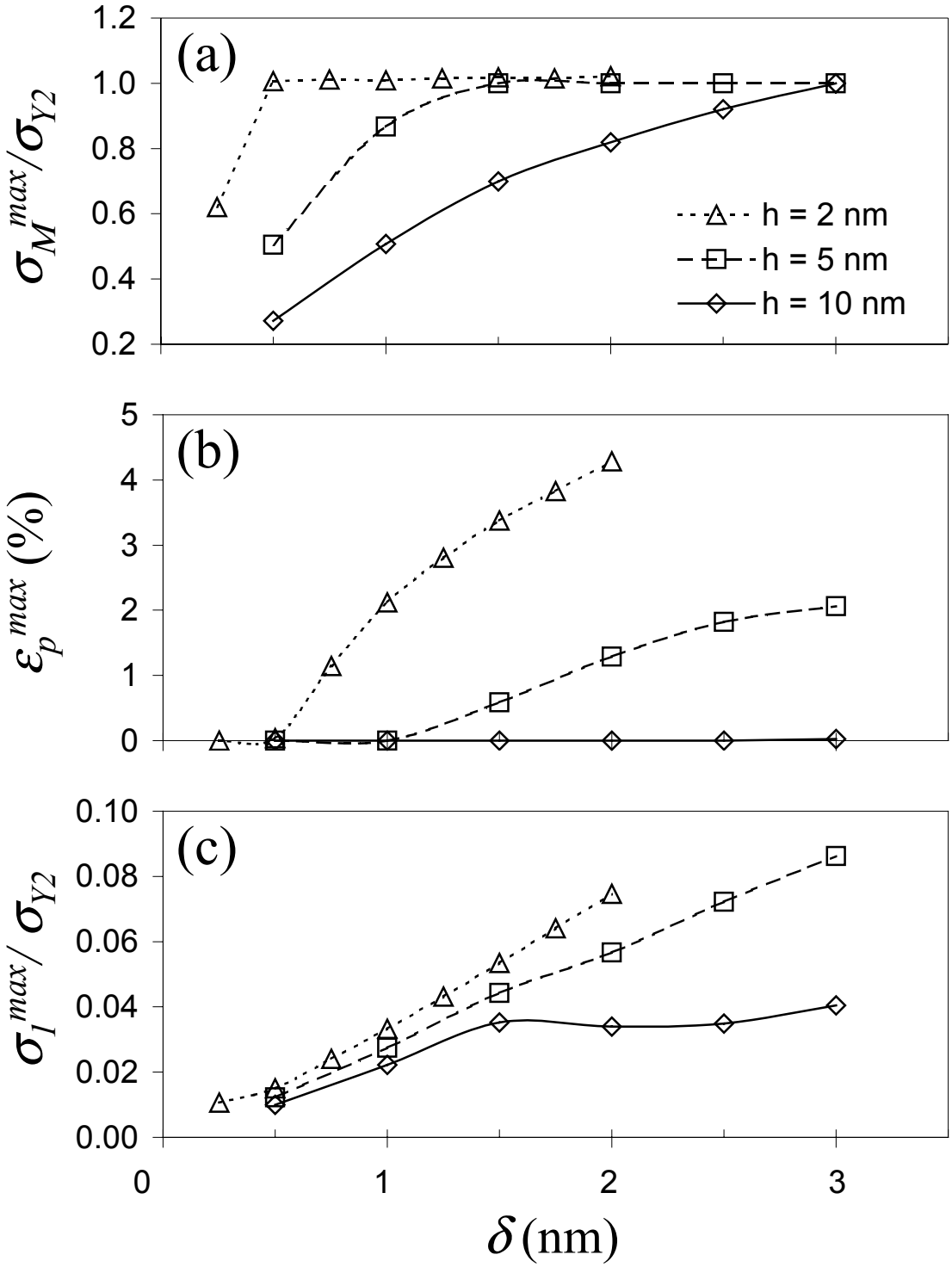

Figure 3.10 Variation of (a) maximum von Mises equivalent stress, $\sigma_M^{\max}$, (b) maximum equivalent plastic strain, $\varepsilon_p^{\max}$, and (c) maximum first principal stress, , with maximum local surface interference δ in the magnetic layer medium for h = 2, 5, and 10 nm, E_1/E_2 = 0.88, and σ_{Y1}/σ_{Y2} = 2.12. (Stress results have been normalized by the yield strength of the magnetic layer, σ_{Y2}.)

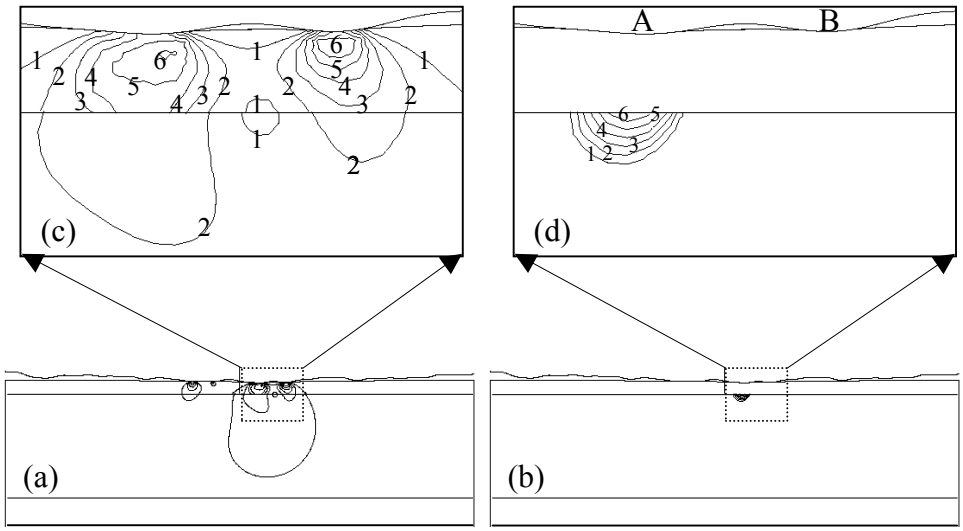

σ_M (GPa):

(1) 1.04	(4) 4.16
(2) 2.08	(5) 5.20
(3) 3.12	(6) 6.24

ε_p (%):

(1) 0.27	(4) 1.09
(2) 0.55	(5) 1.37
(3) 0.82	(6) 1.64

Figure 3.11 Contours of (a), (c) von Mises equivalent stress and (b), (d) equivalent plastic strain for $\delta = 2$ nm, $h = 5$ nm, $E_1/E_2 = 1.29$, and $\sigma_{Y1}/\sigma_{Y2} = 4.87$.

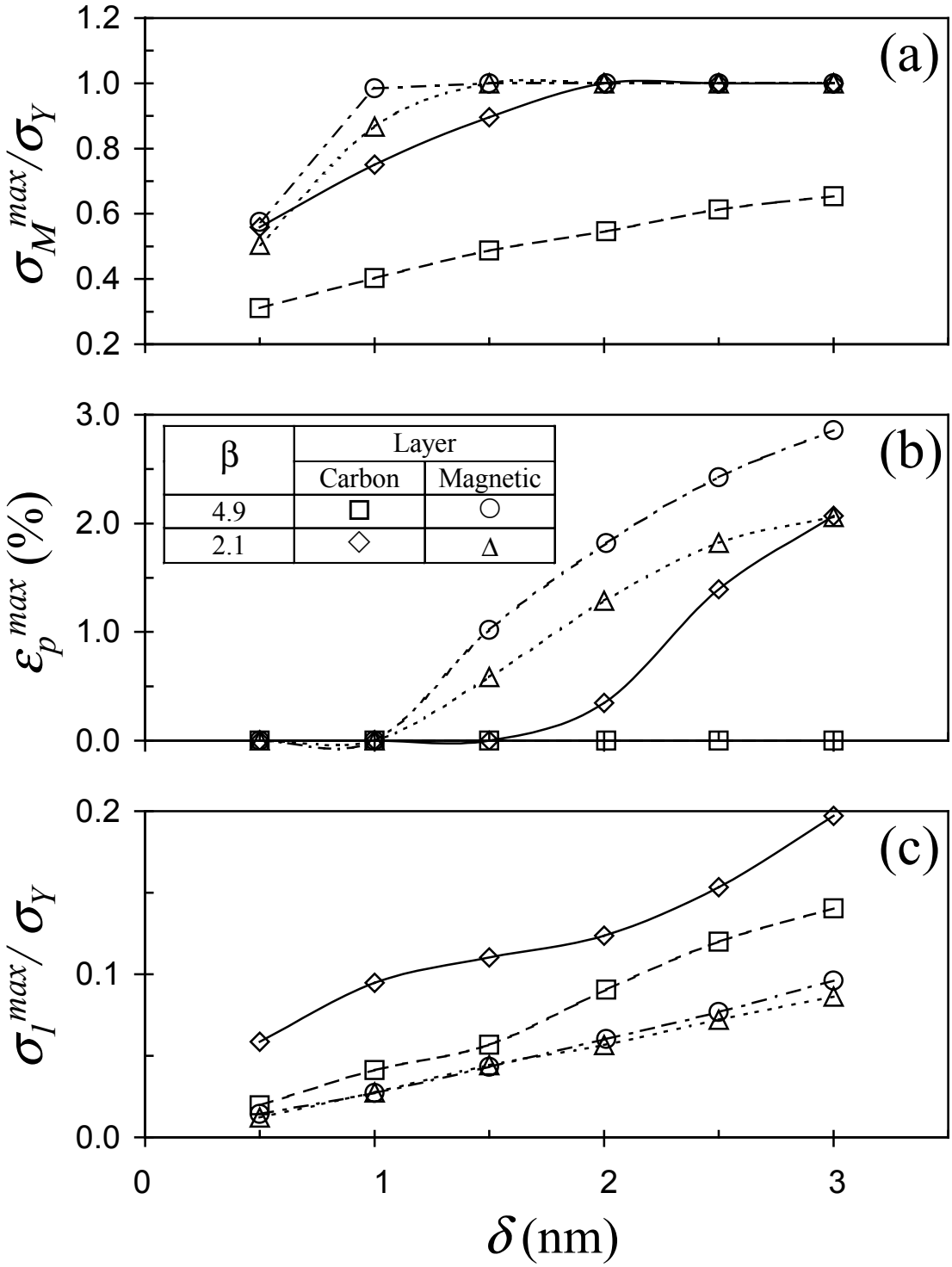

Figure 3.12 Variation of (a) maximum von Mises equivalent stress, σ_M^{max}, (b) maximum equivalent plastic strain, ε_p^{max}, and (c) maximum first principal stress, , with maximum local surface interference δ in the overcoat and magnetic layer media for h = 5 nm, β = 2.1 (E_1/E_2 = 0.88, σ_{Y1}/σ_{Y2} = 2.1), and β = 4.9 (E_1/E_2 = 1.29, σ_{Y1}/σ_{Y2} = 4.87). (Stress results have been normalized by the yield strength of each material, $\sigma_{Y.}$)

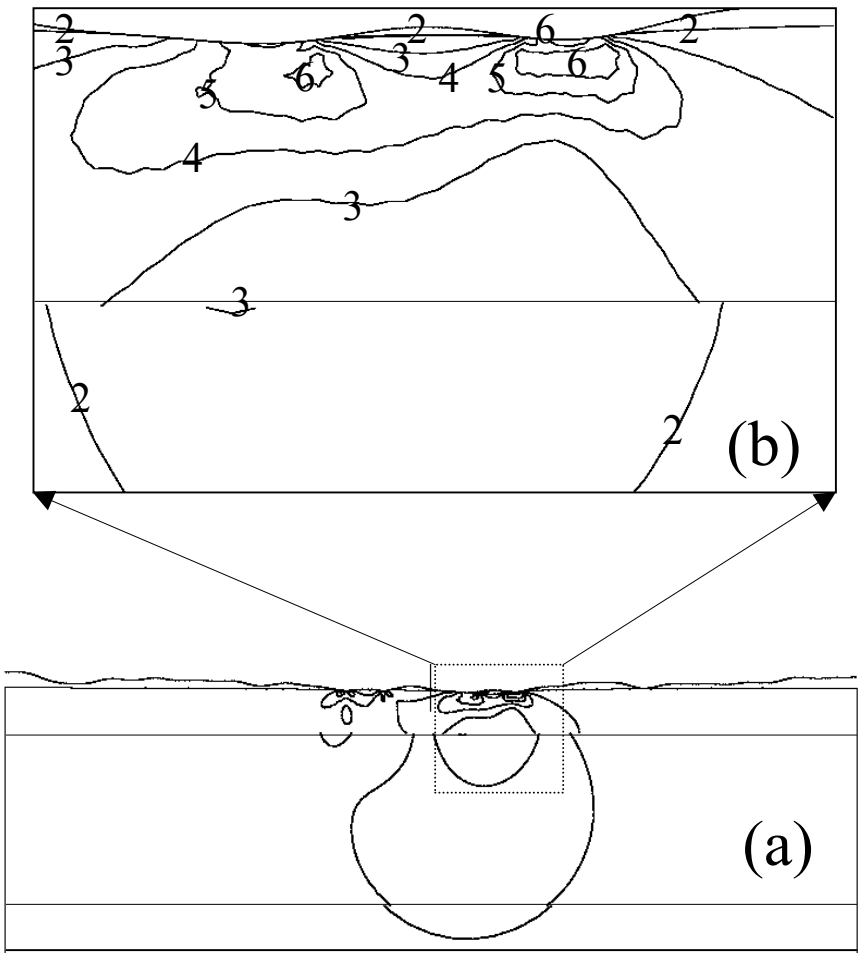

Figure 3.13 Contours of von Mises equivalent stress for δ = 2 nm, h = 10 nm, E_1/E_2 = 0.88, σ_{Y1}/σ_{Y2} = 2.12, and σ_R = –2 GPa.

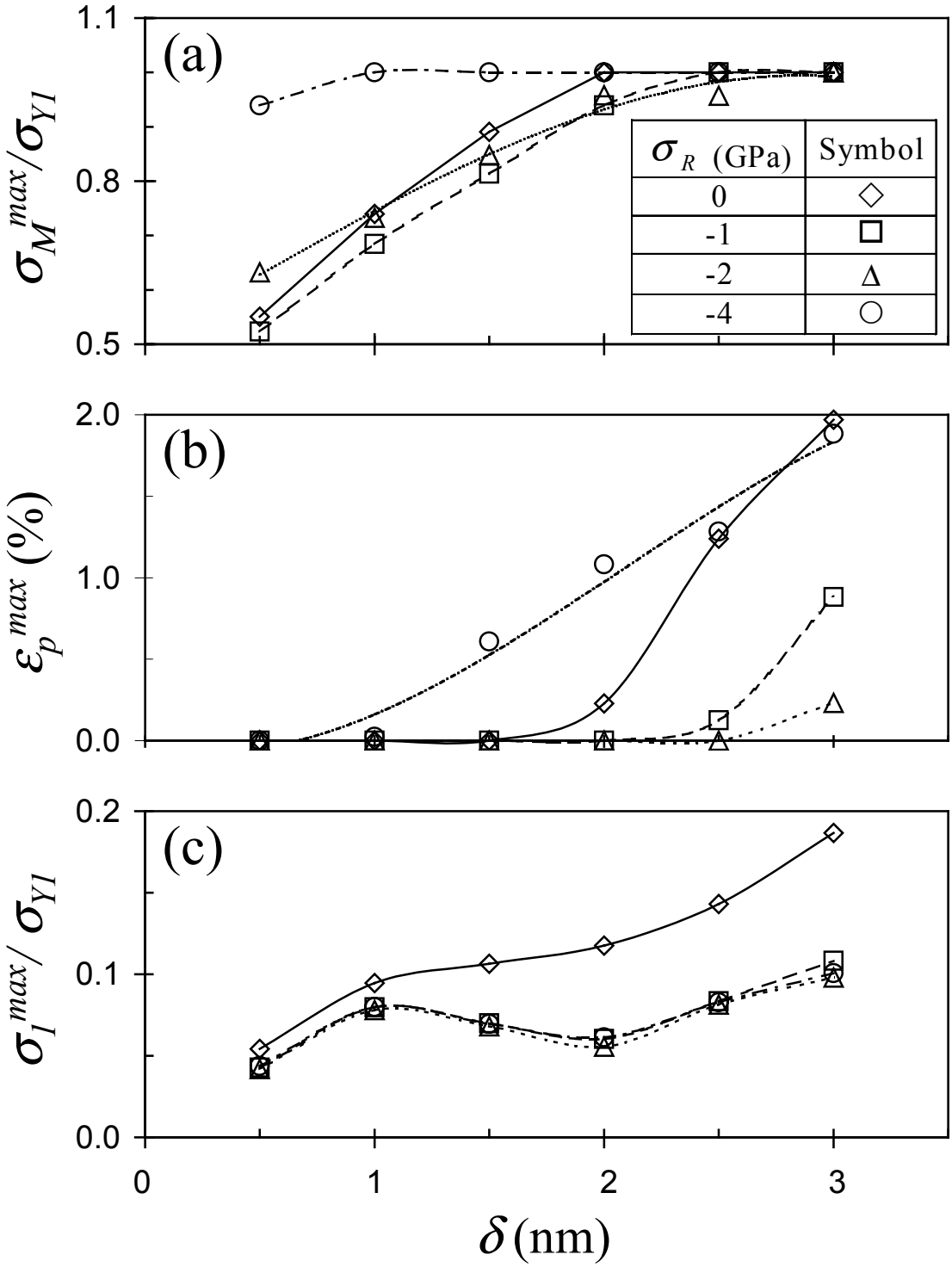

Figure 3.14 Variation of (a) maximum von Mises equivalent stress, σ_M^{max}, (b) maximum equivalent plastic strain, ε_p^{max}, and (c) maximum first principal stress, , with maximum local surface interference δ in the overcoat medium for h = 10 nm, E_1/E_2 = 0.88, σ_{Y1}/σ_{Y2} = 2.12, and σ_R = 0, –1, –2, and –4 GPa. (Stress results have been normalized by the yield strength of the overcoat, σ_{Y1}.)

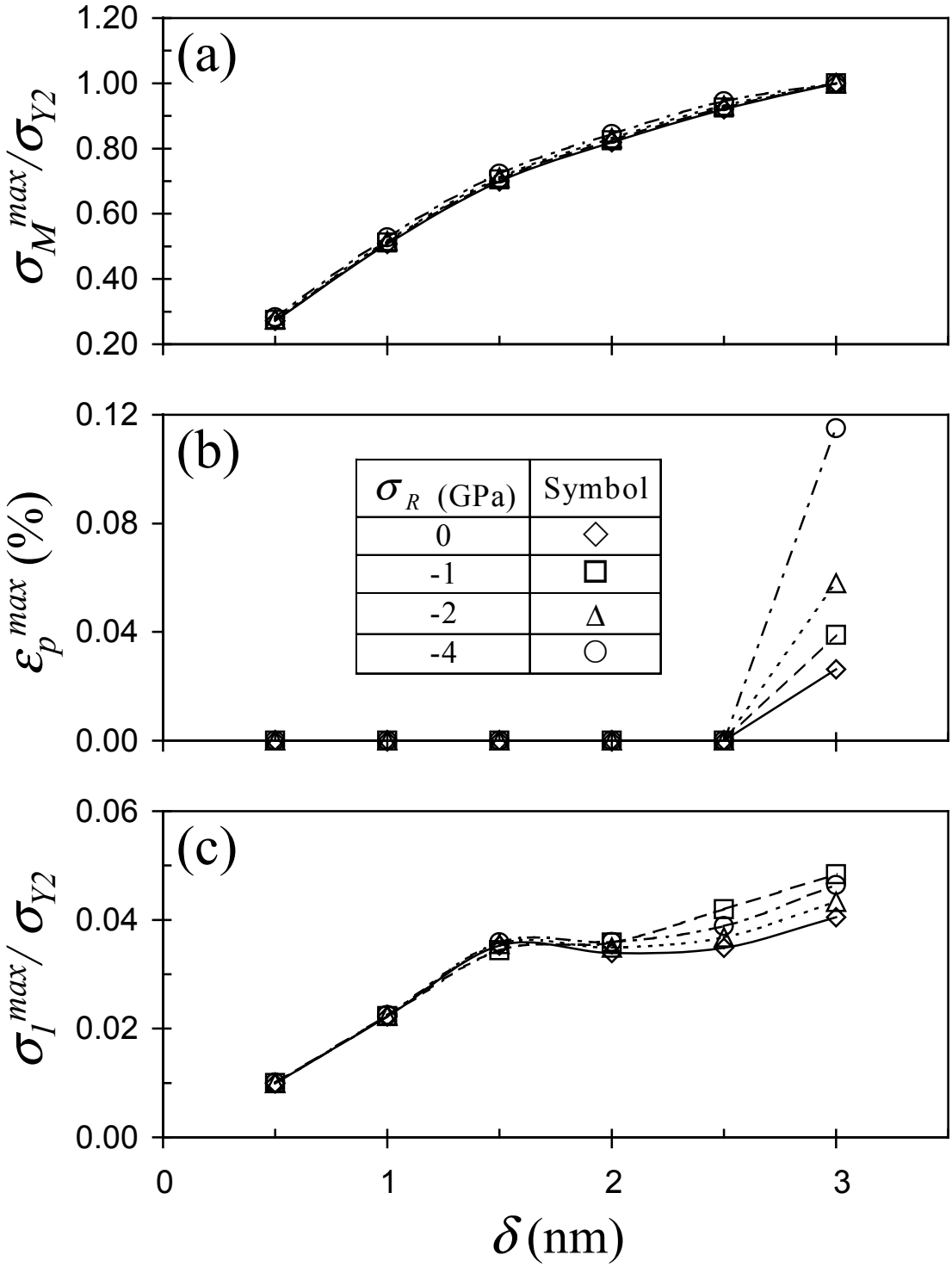

Figure 3.15 Variation of (a) maximum von Mises equivalent stress, σ_M^{max}, (b) maximum equivalent plastic strain, ε_p^{max}, and (c) maximum first principal stress, , with maximum local surface interference δ in the magnetic layer medium for h = 10 nm, E_1/E_2 = 0.88, σ_{Y1}/σ_{Y2} = 2.12 and σ_R = 0, –1, –2, and –4 GPa. (Stress results have been normalized by the yield strength of the magnetic layer, σ_{Y2}.)

CHAPTER 4

THREE-DIMENSIONAL FINITE ELEMENT ANALYSIS OF ELASTIC-PLASTIC LAYERED MEDIA UNDER THERMOMECHANICAL SURFACE LOADING

4.1 Introduction

The development of mechanical traction and frictional heating at sliding interfaces of components is of great importance in a wide range of engineering applications, such as face seals, bearings, automotive brake systems, electric motor brushes, hard disk drives, and electrical switches. Catastrophic failure of electromechanical devices is inevitable without knowledge of the thermomechanical behavior of contacting surfaces. In view of the dependence of the reliability and endurance of various mechanical systems on the material response to thermomechanical loading, numerous analytical and numerical studies of the temperature rise at sliding interfaces were conducted since the pioneering works of Blok (1937) and Jaeger (1942).

Significant advances in analytical and numerical techniques for analyzing material response due to thermomechanical surface loading have been observed in recent years. The focus in early studies was on the thermal response of bodies subjected to constant heat flux and different sliding contact conditions. Kennedy (1981) developed a finite element model to predict the surface temperature of a layered sliding medium due to frictional heating and reported a strong effect of sliding speed on temperature rise. Tian and Kennedy (1993) determined the temperature rise at sliding contacts in terms of the Peclet number, using a three-dimensional model of a coated semi-infinite body and an

integral transform method. Vick et al. (1994) adopted a variation of the boundary element method to examine the influence of a surface coating on the temperature rise at the sliding contact interface of a layered medium due to frictional heating. Tian and Kennedy (1994) used a Green's function method to determine the surface temperature on a semi-infinite body subjected to different moving heat sources.

Thermal and mechanical responses of solids due to thermal loading have been the objective of several studies. Ju and Liu (1988) used a Fourier transform method to obtain analytical solutions for the temperature and thermal stress fields in a semi-infinite medium with a thin, hard coating subjected to frictional heating. Depending on the properties of the layer and substrate materials, crack initiation was predicted to occur in the bulk of the coating and the substrate or at the layer/substrate interface. Leroy et al. (1989, 1990) used a fast Fourier algorithm and a two-dimensional finite element model to study the effects of the coating thickness and properties on the temperature and stresses in a layered medium produced by a moving heat source. Significantly higher coating stresses were reported for elastic modulus and thermal expansion coefficient of the coating higher than those of the substrate. Ju and Farris (1997) also used fast Fourier transformation to study the thermal and mechanical response of an elastic half-space subjected to a moving heat source. However, while in several previous analyses the mechanical response was determined from the applied thermal load, the distribution area of the heat flux was assumed to be unaffected by the mechanical response, i.e., the simultaneous effects of thermal and mechanical loadings on the medium response were not taken into account.

Most studies dealing with both thermal and mechanical behavior of solids under thermomechanical loading have relied on the finite element technique, presumably due to

the complex analytical relations of fully coupled thermomechanical contact problems. Kennedy and Ling (1974b) developed a finite element model to study thermal instabilities in disk brakes. Day and Newcomb (1984) performed finite element simulations and experiments to examine the thermomechanical behavior of automotive brakes. However, this study did not provide a fully coupled thermomechanical analysis because the frictional heat and temperature distribution in each step were obtained for fixed contact pressure and contact area. Kulkarni et al. (1991) developed a two-dimensional finite element model of a thermomechanical load moving over an elastic-plastic half-space, and reported results for the temperature distribution, stresses, and plastic strains. Although solutions for the temperature and displacement fields were obtained simultaneously, the thermomechanical load was assumed to be constant, despite changes in the temperature and displacement fields. Gupta et al. (1993) used the finite element technique to study two-dimensional rolling and sliding over a semi-infinite half-space, assuming invariance of the contact pressure with temperature changes. Cho and Komvopoulos (1997) conducted a linear elastic fracture mechanics analysis of subsurface cracking in a homogeneous half-space subjected to a moving thermomechanical surface load and reported that the effect of frictional heating on the crack growth behavior becomes more pronounced with increasing contact friction, crack length-to-depth ratio, and Peclet number.

Despite useful insight into thermomechanical behavior of contacting bodies, the majority of earlier studies used simplistic constitutive models (e.g., purely elastic behavior), ignored the interdependence of thermal and mechanical responses, and assumed invariant contact pressure distribution despite temperature variations. The

frictional heat generated in sliding contacts depends on the contact area and contact pressure profile and vice versa. Therefore, to accurately determine the stress field and contact pressure due to thermomechanical surface loading, it is necessary to adopt more realistic constitutive models (e.g., elastic-plastic material behavior) and account for the coupling of thermal and mechanical solutions. Hence, the main objective of this study was to investigate the thermomechanical response of elastic-plastic half-space media (both homogeneous and layered) under sliding contact. To accomplish this goal, a three-dimensional fully coupled thermomechanical finite element model was developed, and its accuracy was checked by comparing simulation results with analytical solutions from previous studies. Finite element results for the temperature, stresses, and plastic strain in an elastic-plastic layered medium under thermomechanical surface loading are presented for different thickness and thermal conductivity of the layer, Peclet number, and distance (time) from the initiation of sliding. The significance of mechanical traction and frictional heating on the propensity of the layered medium to undergo yielding and cracking are interpreted in the context of the obtained simulation results.

4.2 Finite Element Model

Sliding of an elastic sphere of radius R on elastic-perfectly plastic homogeneous and layered half-spaces was simulated with a finite element model composed of three-dimensional, eight-node, coupled temperature-displacement elements. Due to symmetry, only one-half of the sphere and the half-space medium were modeled in order to reduce the computation time. Figure 4.1 shows a cross section (x = 0) of a typical three-dimensional finite element mesh used in this study, consisting of 13,563 elements having a total of 19,902 nodes. The normalized mesh dimensions of the layered medium were

x/R = 1, y/R = 0.976 to 1.4 (depending on the layer thickness) and z/R = 3, while those of the homogeneous medium were x/R = 1, y/R = 1.4, and z/R = 3. Since sliding was simulated along the positive z-direction, plane x = 0 was a symmetry plane. The nodes on planes x/R = 0 and 1 were fixed against displacement in the x-direction, the nodes of the bottom boundary of the mesh were fixed against displacement in the y-direction, and the nodes on planes z/R = –1 and 2 were fixed against displacement in the z-direction. The temperature at the nodes of planes z/R = –1 and 2 was set equal to zero. The top and bottom boundaries of the mesh were thermally insulated except the contact area. The layered medium consists of a layer with thickness h/R = 0.02, 0.05, and 0.1 and a substrate with corresponding thickness h/R = 0.956, 0.956, and 1.3 and different material properties. Thickness and physical properties of the sphere and layered medium are given in Table 4.1. The values for the layer and substrate materials are typical of carbon overcoats and magnetic layers, respectively, used in computer hard disks. The elastic and thermal properties of the sphere were identical to those of the layer material; however, in all simulations the conductivity of the sphere was set equal to 5.2 W/m· K, i.e., constant thermal diffusivity of 4.837×10^{-6} m^2/s.

In sliding contacts, mechanical energy is transformed to heat due to the effect of friction. As frictional heat flows into the contacting bodies, the area of contact changes due to thermal expansion, affecting the contact pressure distribution. Since these changes in the contact conditions influence the heat generation rate and thermal boundary conditions, the mechanical and thermal analyses are interdependent and the temperature and stress/strain fields must be determined simultaneously, rather than sequentially as in most previous studies. In the present analysis, the temperature was integrated using a

backward-difference scheme, $T_{j+1} = T_j + \Delta t \dot{T}_{j+1}$, where T is the temperature and subscript j indicates the j^{th} time step, and the coupled system was solved using Newton's method. The adopted technique automatically invokes an asymmetric matrix storage and solution scheme to improve convergence. This is because the stiffness matrix is not symmetric due to friction and the convective term in the conduction-convection equation.

Contact between the sphere and the half-space was modeled with special contact elements, thus avoiding *a priori* assumptions for the contact pressure distribution. The overclosure (i.e., surface interpenetration) and relative tangential displacement were determined at each integration point of the contact elements. These two types of kinematic measures and appropriate Lagrange multipliers were used to determine the normal and tangential (friction) traction at the contact interface. The contact pressure at a point of the interface, p, depends on the local overclosure, d, of the surfaces, i.e.,

$$p = 0, \qquad \text{for } d < 0, \qquad \text{(no contact)} \tag{4.1a}$$

$$p = K\,d, \qquad \text{for } d \geq 0, \qquad \text{(contact)} \tag{4.1b}$$

where K is the contact stiffness, determined through an iterative procedure that satisfies equilibrium. Equations (4.1a) and (4.1b) indicate that the contact pressure is equal to zero when the two surfaces are separated, and assumes nonzero values at those surface nodal points where contact is established. The actual contact pressure depends on the material properties and boundary conditions.

A shear stress, t, develops between the contacting surfaces with the occurrence of a very small relative tangential displacement (stick). Lateral movement (slip) commences when $t = f\,p$, where f is the coefficient of friction. Thus, the stick and slip conditions at

the contact interface can be expressed as

$$t < f\,p \qquad \text{(stick)} \tag{4.2a}$$

$$t = f\,p \qquad \text{(slip)} \tag{4.2b}$$

In all simulation cases, the coefficient of friction specified for the contact elements was equal to 0.5.

The contact area depends on the fraction of energy converted to frictional heat during sliding, h, and the fraction of the frictional heat dissipated in each surface, f_1 and f_2, respectively. The heat flux density due to frictional heating, q_g, is given by

$$q_g = h\,t\,\frac{\Delta s}{\Delta t}, \tag{4.3}$$

where Ds and Dt denote incremental lateral displacement and time, respectively. Heat is instantaneously conducted into each body, depending on the values of f_1 and f_2. Unlike other methods, where it was assumed that heat is generated within elements near or at the contact interface, in the present analysis the contact interface has no heat capacity because it is modeled to have zero thickness. Therefore, because the heat is not generated within elements, the heat fractions f_1 and f_2 are used to model the distribution of heat in each contacting body.

The heat flux densities of the sphere and half-space medium, q_1 and q_2, respectively, are given by

$$q_1 = -q_k + f_1 q_g, \tag{4.4a}$$

and

$$q_2 = q_k + f_2 q_g, \tag{4.4b}$$

where q_k is the heat flux across the contact interface due to conduction. Since heat flux

due to convection and radiation was neglected in this study, the obtained temperature solutions represent upper bounds. Nevertheless, because heat flux due to radiation is normally much smaller than that due to conduction, its effect can be ignored as secondary. When both bodies are at the same temperature, the heat flux into each body is equal to $0.5\,q_g$. However, as the sphere becomes hotter due to continuous sliding, heat conduction q_k occurs across the contact interface (Eqs. (4.4a) and (4.4b)).

Simulations were performed for $f_1 = f_2 = 0.5$, assuming that the total frictional energy is dissipated as heat ($h = 1$), consistent with Kennedy's finding (1984). The fraction of heat generated in each body differs from the traditional heat partition factor, which is equal to q_1/q_2. Thus, in the present study the traditional heat partition factor varied with the heat flux due to conduction across the contact interface, q_k, given by

$$q_k = k_g(q_1 - q_2), \tag{4.5}$$

where q_1 and q_2 are temperatures at surface elements of the sphere and half-space medium, respectively, and k_g is the gap conductance, assumed equal to $k_L/\Delta y$, with $\Delta y = \Delta l/10$, where k_L is the thermal conductivity of the layer and Δl is the size of the smallest element at the mesh surface. The gap conductance represents the thermal conductivity of a fictitious "third-body" layer of thickness Δy between the contacting surfaces, used to avoid temperature discontinuities and infinite heat flux at the contact interface. Preliminary simulations revealed the occurrence of temperature discontinuities when $\Delta y > \Delta l$; however, a continuous and invariant temperature field was obtained when $\Delta y < \Delta l/10$. Hence, the value of k_g was selected to yield a continuous temperature across the contact interface. The continuity of the interface temperature determines the traditional heat

partition factor, q_1/q_2 (Eqs. (4.4a), (4.4b), and (4.5)). In addition, the high gap conductance reduced the sensitivity of the results on the values of f_1 and f_2.

Both the layer and the substrate were modeled as elastic-perfectly plastic materials, obeying the yield condition

$$s_M = \sqrt{\frac{3}{2} S_{ij} S_{ij}} = s_Y, \tag{4.6}$$

where s_M is the von Mises equivalent stress, S_{ij} is the deviatoric stress tensor ($S_{ij} = s_{ij} - s_{kk} d_{ij}/3$, where s_{ij} is the stress tensor and d_{ij} is Knonecker's delta function), and s_Y is the yield strength in uniaxial tension. The layer and substrate materials exhibit linear elastic behaviors up to yielding, thereafter following the usual flow rule given by

$$de_{ij}^p = dl \; S_{ij}, \tag{4.7}$$

where de_{ij}^p is the plastic strain increment and dl is a scalar depending on the plastic strain rate.

Quasi-static sliding contact simulations were performed with the multi-purpose finite element code ABAQUS using six main steps. The simulations comprised indentation of the half-space by the sphere (at $z/R = 0$) to a depth corresponding to a fixed normal load, followed by five incremental displacements of the sphere in the z direction, Dz/R = 0.05, 0.15, 0.35, 0.65, and 0.95, under the given load and constant sliding speed, v. Each incremental displacement, Dz, was simulated in 5-30 time steps, $\Delta t = \Delta l/v$, each consisting of 8-23 increments. The magnitudes of Δt, Δl, and v were selected to satisfy condition for numerical stability, $v\Delta t/\Delta l \leq 1$ (Yu and Heinrich, 1986). An automatic time increment scheme was used in each time step, and the magnitude of the time increment

was adjusted according to the maximum allowable temperature change, $\Delta T_{max} = T_{max}/20$ and $T_{max}/5$ for homogeneous and layered media, respectively, where T_{max} is the maximum surface temperature determined from preliminary simulations using larger values of ΔT_{max} and a coarser mesh. A smaller time increment was used when the temperature change during this particular time increment was found larger than ΔT_{max}. If this did not occur within three consecutive iterations, a greater increment was used in the following iteration. The typical computational time on a Pentium III 550 workstation was about 55,040 CPU seconds.

4.3 Model Validation

Normal contact simulations (with and without frictional heating) were performed in order to evaluate the appropriateness of the finite element model. Figure 4.2 shows a comparison between finite element results and analytical solutions (Huber, 1904) for an elastic homogeneous half-space, with properties identical to those of the layer material, indented by a rigid sphere. The stresses were normalized by the maximum contact pressure, p_0, and coordinate z by the contact radius, r. The figure shows a good agreement between finite element and analytical solutions for the normal surface stresses along the z-direction ($x = y = 0$). A closer agreement could have been achieved with further refinement of the mesh adjacent to the surface, at the expense of computational time. Results for the surface temperature distribution obtained from a thermomechanical finite element analysis of a sphere sliding over an elastic homogeneous half-space are shown in Fig. 4.3 ($h = 1$ and $f = 0.5$). The figure shows the evolution of the surface temperature, T, with time, t, for Peclet number $Pe = 30$ ($Pe = vr/a$, where a is the thermal diffusivity). In this figure, as well as in subsequent figures, the temperature was normalized by $2rq_m/k$,

where q_m is the average heat flux into the medium and k is the thermal conductivity, and the time was normalized by t_0, which is the time for the sphere to slid over the medium by a distance equal to the contact radius. The z-coordinate of the sphere center is denoted by z_0. The maximum temperature increases with time and its location shifts gradually toward the trailing edge of the contact region due to the movement of the heat source (sphere). The temperature distribution reaches a steady state at t/t_0 = 6.50. The variation and magnitude of the peak temperature, shown in Fig. 4.3, are in fair agreement with analytical results (Tian and Kennedy, 1994). In fact, the normalized maximum temperature at t/t_0 = 6.50 is equal to 0.163, which differs only by 1 percent from the steady-state temperature value predicted by Tian and Kennedy (1994). Favorable comparisons of the results shown in Figs. 4.2 and 4.3 with those of other studies (Tian and Kennedy, 1994; Huber, 1904) indicate the suitability of the finite element model and appropriateness of the boundary conditions for thermomechanical sliding contact analysis.

4.4 Results and Discussions

Finite element solutions for the temperature, stress, and strain fields in a layered medium subjected to thermal and mechanical surface loadings are interpreted in terms of the thickness and thermal conductivity of the layer, Peclet number, and distance of sliding. All simulation results presented below were obtained for h = 1 (unless stated otherwise) and m = 0.5. The significance of frictional heating and tangential (friction) traction on the deformation behavior, in particular the tendency for yielding and cracking in the layered medium, is elucidated in light of stress and strain results. The typical number of elements in the contact region was 14 to 16. For the layered medium with the

thinnest layer (h/R = 0.02) that exhibited relatively more severe plastic deformation, the ratio of the maximum contact pressure and the substrate yield strength was found to be equal to 2.3. Despite the relatively large thermal expansion coefficient mismatch between the layer and substrate materials, this effect on the stress/strain field at the interface of the layered medium was found to be secondary, evidently because of the lower temperature rise in the substrate due to the significantly higher thermal conductivity of the substrate material.

Figure 4.4 shows the variation of the maximum contact pressure and contact radius with the normalized maximum temperature at the surface of a homogeneous elastic-plastic medium with properties identical to those of the layer material (Table 4.1, k = 0.052 W/m·K) for Pe = 30 and h = 1. The maximum contact pressure due to indentation, p_{oi}, and corresponding contact radius, r_i, were used to normalize the pressure and contact radius, respectively. Figure 4.4(a) reveals a linear increase of the peak contact pressure with maximum temperature to values greater than that obtained without frictional heating (i.e., pure indentation) by about 30 percent. Figure 4.4(b) demonstrates a less pronounced, non-linear temperature dependence of the contact area on the maximum surface temperature. The slight increase of the contact region with increasing temperature is attributed to thermal expansion of both the sphere and the homogeneous medium.

Figure 4.5 illustrates the effect of frictional heating on the steady-state distribution and maximum value of the von Mises equivalent stress in a homogeneous elastic-plastic half-space with properties identical to those of the layer material (Table 4.1, k = 0.052 W/m·K) for Pe = 30 and h = 0 and 1. The maximum indentation load and penetration

depth during sliding were the same in both thermomechanical (h = 1) and mechanical (h = 0) simulation cases. The maximum von Mises equivalent stress during sliding occurs always at the surface. (Stress values at surface nodes were obtained by extrapolation from stress values calculated at integration points.) The small stress fluctuation in the contact region is due to numerical effects. The results shown in Fig. 4.5(a) are consistent with analytical results of Hamilton (1983) and Sackfield and Hills (1983), demonstrating that the maximum von Mises stress occurs always at the surface when f > 0.3. Frictional heating affects the location of the maximum Mises stress at the surface. For h = 0, the maximum Mises stress occurs near the front edge of the contact region ($z > z_0$), whereas for h = 1 it occurs at the center of contact ($z = z_0$). For h = 1, the temperature at the contact interface rises as the sphere slides over the medium, leading to thermal expansion of both sphere and half-space media. As shown in Fig. 4.5(a), growth of the contact region due to thermal expansion affects the steady-state Mises stress distribution. However, Fig. 4.5(b) shows that the effect of frictional heating is negligible during indentation, evidently due to the very small relative slip at the contact interface in normal contact. Under purely mechanical loading (h = 0), the maximum Mises stress increases rapidly with the onset of sliding, reaching a steady state at a sliding distance approximately equal to the contact radius (t/t_0 = 1). However, when frictional heating occurs simultaneously with mechanical loading at the contact interface (h = 1), the maximum Mises stress continues to intensify during sliding, thus increasing the probability of yielding at the contact region.

Temperature results for a layered medium with properties given in Table 4.1 (h/R = 0.1 (layer) and 1.3 (substrate); k_L = 5.2 W/m·K (layer)) subjected to both thermal and

mechanical loadings are shown in Fig. 4.6 for Pe_L = 0.29, where Pe_L is the Peclet number defined in terms of the thermal diffusivity of the layer, $a_L = k_L / r_L c_L$, where r_L and c_L are the density and heat capacity of the layer, respectively. The temperature is normalized by the thermal conductivity of the substrate, k_s. Figures 4.6(a) and 4.6(b) show the temperature evolution at the surface (y/h = 0) and interface (y/h = –1) of the layered medium, respectively. A steady-state surface temperature profile was obtained at a sliding distance of about four times the contact radius (i.e., t/t_0 = 4.62), in agreement with the findings of a previous study (Kennedy, 1981). Figure 4.6(b) shows that the interface temperature is significantly lower than that at the layer surface. The main reason for this temperature difference is the very low thermal conductivity of the layer (~5.3 percent that of the substrate). This case resembles that of a thermally conductive substrate coated by an insulating material. Thus, the small fraction of frictional heat reaching the layer/substrate interface is effectively conducted into the substrate medium, thus producing a temperature rise at the interface an order of magnitude less than that at the layer surface.

Figures 4.7 and 4.8 show the effects of the layer material properties and thickness on the maximum temperature rise at the surface and interface of an elastic-plastic layered medium. Three cases of different layer thermal conductivity (k_L = 0.052, 0.52, and 5.2 W/m·K) and fixed thickness (h/R = 0.02 (layer) and 0.956 (substrate)), and three cases of fixed layer thermal conductivity (k_L = 5.2 W/m·K) and different layer thickness (h/R = 0.02, 0.05, and 0.1, and corresponding substrate thickness h/R = 0.956, 0.956, and 1.3) were simulated for the same normal load and sliding speed. The increase of the maximum surface temperature with Peclet number (Fig. 4.7(a)) suggests a higher probability of

thermal cracking at the surface of the layered medium. An opposite trend can be seen for the temperature at the layer/substrate interface (Fig. 4.7(b)). The increase of Pe_L can be associated with higher sliding speed, larger conduct radius, and lower diffusivity. Hence, in the case of a fast moving heat source and/or insulating layer material, heat conduction through the layer is prevented and high temperatures arise only at the layer surface within the contact region. Similar trends are observed with increasing layer thickness (Fig. 4.8). However, considering the change of the maximum temperature in terms of the corresponding ranges of Peclet number and layer thickness (the scale of the horizontal axis in Fig. 4.7 is logarithmic), it is concluded that the effect of the layer thickness is relatively more pronounced than that of the layer thermal conductivity (or Peclet number). Therefore, it may be argued that a thicker and less conductive layer will be more effective in protecting the substrate from thermal softening and phase transformation (annealing), although under certain circumstances this might have an adverse effect on the layer.

The likelihood of yielding and cracking in the layered medium due to thermomechanical loading can be interpreted by considering the variation of the maximum von Mises equivalent stress, $s_M^{\max} / p_0$, maximum first principal stress, $s_I^{\max} / p_0$, and maximum equivalent plastic strain, $e_p^{\max}$, with sliding time, t/t_0, and layer thickness, h/R, shown in Figs. 4.9 and 4.10. Stresses were normalized by the maximum contact pressure, p_0, corresponding to $h/R = 0.1$ and $t/t_0 = 0$. Locations of maximum stress and strain are indicated by open and filled symbols. Open (filled) symbols in Fig. 4.9 denote the layer surface (interface), while open (filled) symbols in Fig. 4.10 denote the bulk (interface) of the substrate. The same normal load was used in all simulation cases.

Both $s_M^{\max}$ and $s_I^{\max}$ increase rapidly with the initiation of sliding in both layer and substrate media, evidently due to the development of shear traction, reaching steady-state values at sliding distances of 2-6 times the contact radius, depending on the layer thickness. The higher maximum von Mises and first principal stresses obtained with relatively thin layers (h/R = 0.02) indicate a greater propensity for thin overcoats to undergo plastic deformation and cracking due to thermomechanical surface loading.

The layer thickness plays an important role on the location of $s_M^{\max}$ and $s_I^{\max}$. For relatively thin layers (h/R = 0.02), sliding causes $s_M^{\max}$ to shift from the surface to the interface of the layer (Fig. 4.9(a)), while $s_I^{\max}$ occurs always at the layer surface (Fig. 4.9(b)). For layers of intermediate (h/R = 0.05) or relatively large (h/R = 0.1) thickness, an opposite trend is observed after the initiation of sliding ($t/t_0 > 1$), i.e., the location of $s_M^{\max}$ shifts from the interface to the surface of the layer, indicating a significant friction (thermal) effect on the location where plasticity commences in these layers (Fig. 4.9(a)). For h/R = 0.02 and 0.05, $s_I^{\max}$ occurs always at the surface; however, for h/R = 0.1 it shifts from the interface to the surface of the layer after the initiation of sliding. Thus, shear traction and frictional heating affect the location of the maximum tensile stress during sliding only in the case of relatively thick layers (Fig. 4.9(b)).

Regarding deformation in the substrate, Fig. 4.10(a) shows that plastic deformation during sliding occurs always at the interface. For the range of layer thickness, material properties, and normal load analyzed, plasticity was confined in the substrate in all simulation cases. The magnitude of $e_p^{\max}$ in the substrate increases with decreasing layer thickness, suggesting a greater likelihood for plastic flow in the substrate

in the case of thin layers. In addition, the thin layer produces a higher maximum tensile stress at the layer/substrate interface (Fig. 4.10(b)). The location of $s_I^{\max}$ shifts from the bulk to the interface of the substrate for h/R = 0.05 and 0.1 but not for h/R = 0.02. This indicates that the effect of shear traction and frictional heating on the location where microcracking is likely to occur in the substrate of layered media is significant in the case of overcoats with intermediate and large thickness. The results shown in Figs. 4.9 and 4.10 reveal the important role of the layer thickness on the resistance against plastic deformation and cracking of layered media subjected to thermomechanical surface loading.

4.5 Conclusions

A thermomechanical finite element analysis for an elastic sphere sliding on an elastic-plastic layered (or homogeneous) half-space was performed to elucidate the role of material properties and thickness of the layer on the evolution of temperature, stress, and strain fields. The present finite element model accounts for the simultaneous effects of elastic-plastic deformation and conduction of frictional heat in both contacting solids. Based on the presented results and discussion, the following main conclusions can be drawn.

(1) A three-dimensional finite element model for thermomechanical contact analysis was developed and validated by comparing simulation results with solutions from an elastic normal contact analysis and surface temperature results from an earlier thermal numerical analysis of sliding contact.

(2) Steady-state temperature distributions were reached at the layer surface and layer/substrate interface at sliding distances of 4-6 times the contact radius.

(3) For the range of parameters examined in this study, the layer thickness exhibits a more pronounced effect on the temperature rise at the layer surface and layer/substrate interface than the layer thermal conductivity.

(4) Frictional heating and shear surface traction may intensify the stress field significantly. The likelihood for yielding and cracking in the layered medium increases with decreasing layer thickness. The locations of the maximum von Mises equivalent stress, maximum tensile stress, and maximum equivalent plastic strain are affected by the layer thickness and the frictional heat conducted through the layer, which is controlled by the thermal conductivity of the layer material, coefficient of friction, contact interface compliance, and applied normal load.

Table 4.1. Thickness and properties of layered medium and sphere used in the finite element model

Medium	Layer	Substrate	Sphere
Thickness, h/R	0.02, 0.05, 0.1	0.956, 0.956, 1.3	–
Elastic modulus, E (GPa)	168	130	168
Poisson ratio, n	0.3	0.3	0.3
Yield strength, s_Y (GPa)	13	2.67	–
Conductivity, k (W/m · K)	0.052, 0.52, 5.2	98	5.2
Specific heat, c (J/g · K)	0.5	0.42	0.5
Density, r (kg/m^3)	2150	8800	2150
Thermal expansion (K^{-1})	2×10^{-6}	13×10^{-6}	2×10^{-6}
Thermal diffusivity, a (m^2/s)	$4.837 \times (10^{-8}, 10^{-7}, 10^{-6})$	26.52×10^{-6}	4.837×10^{-6}

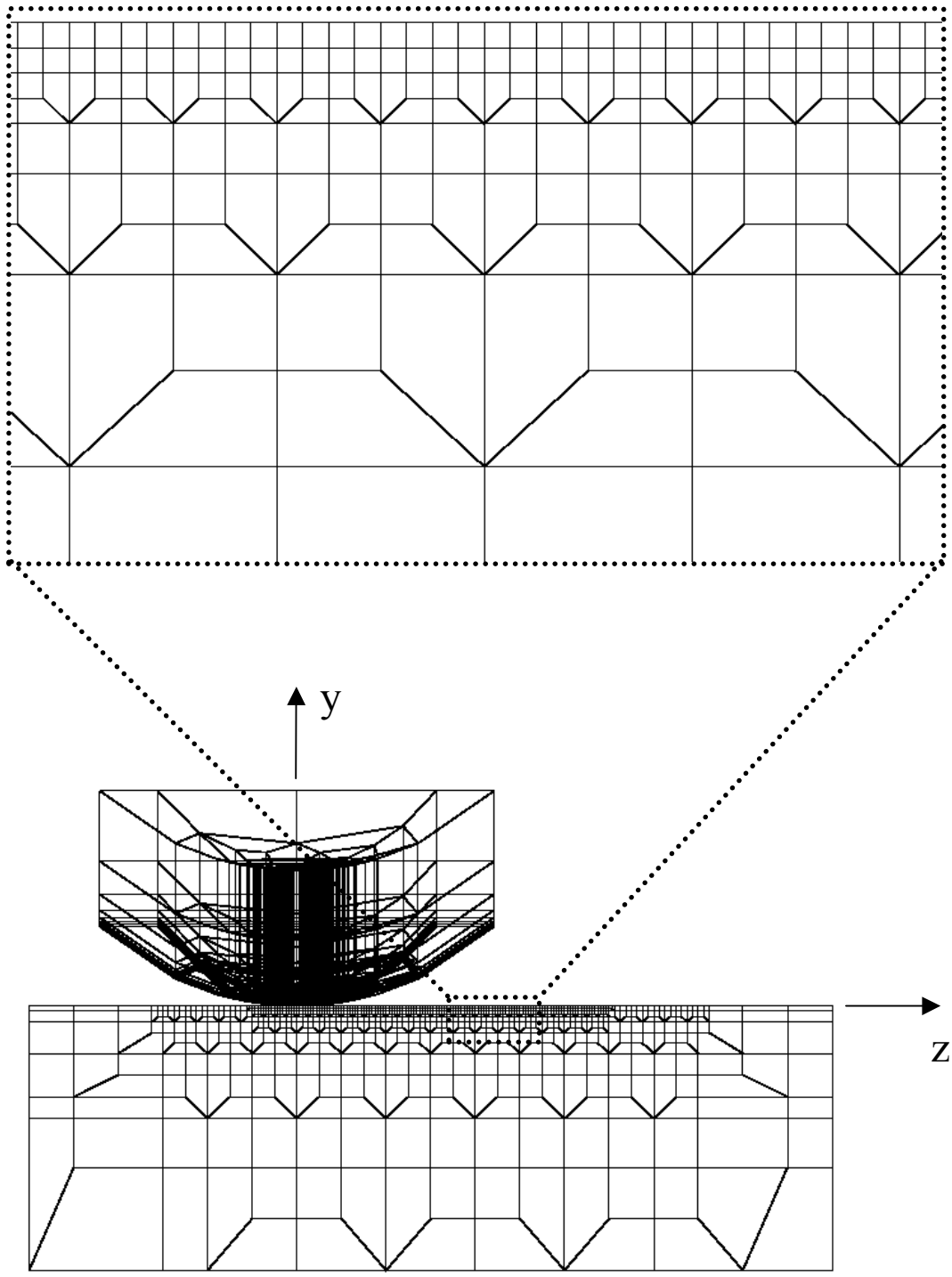

Figure 4.1 Cross section (x = 0) of three-dimensional finite element mesh used in the thermomechanical sliding contact simulations.

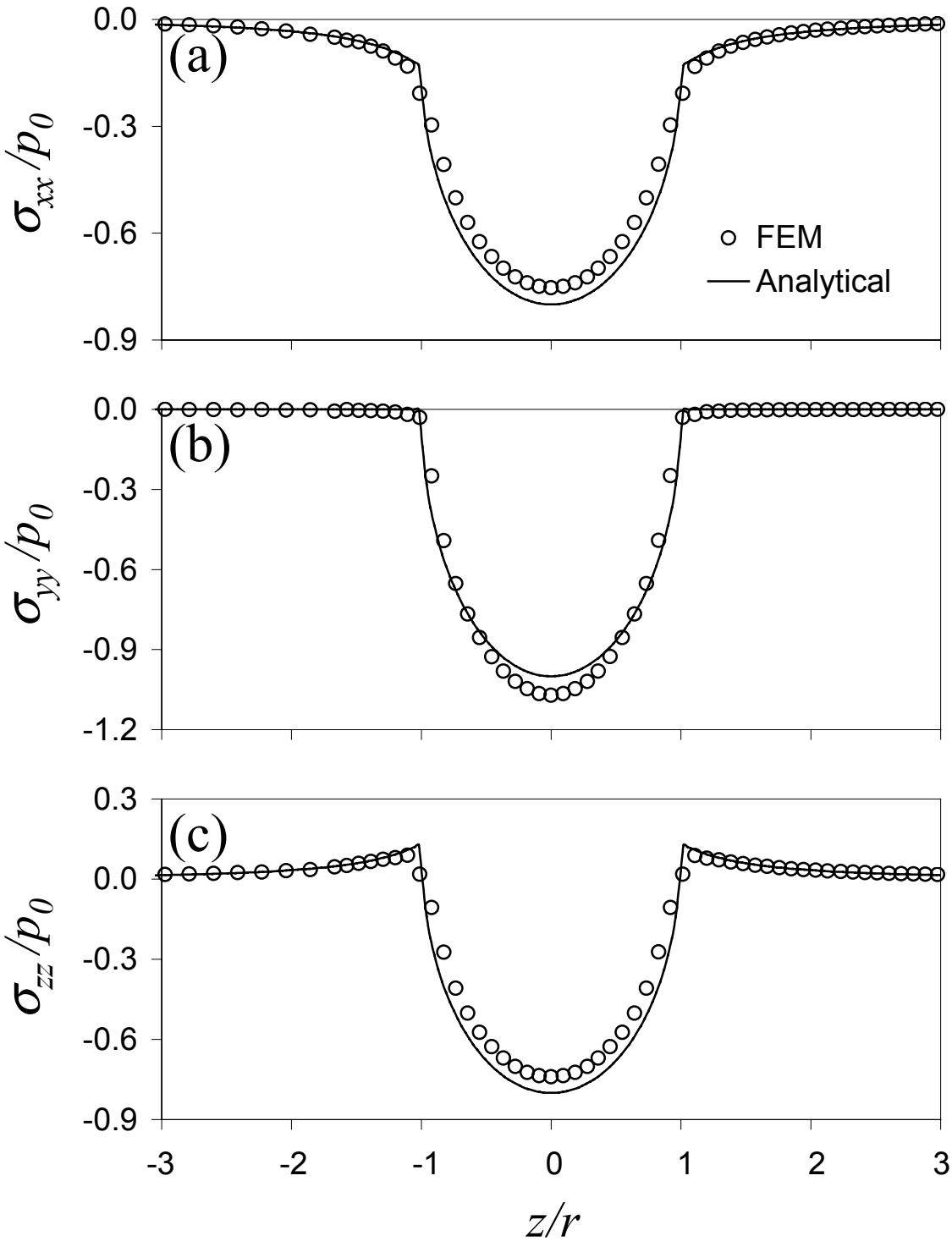

Figure 4.2 Comparison of finite element and analytical results for (a) σ_{xx}, (b) σ_{yy}, and (c) σ_{zz} stresses at the surface of an elastic homogeneous medium indented by a rigid sphere.

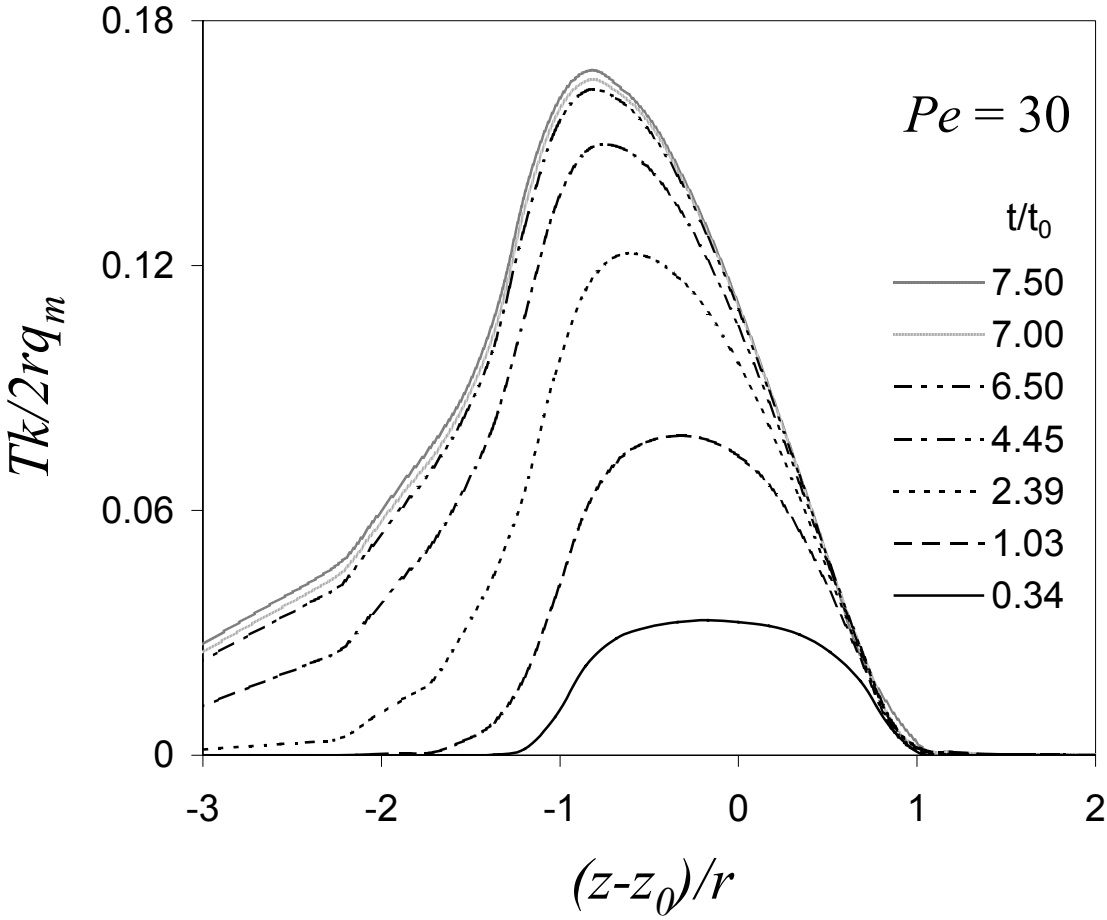

Figure 4.3 Evolution of temperature at the surface of an elastic homogeneous medium in sliding contact with an elastic sphere ($\eta = 1$, $f = 0.5$, and $Pe = 30$).

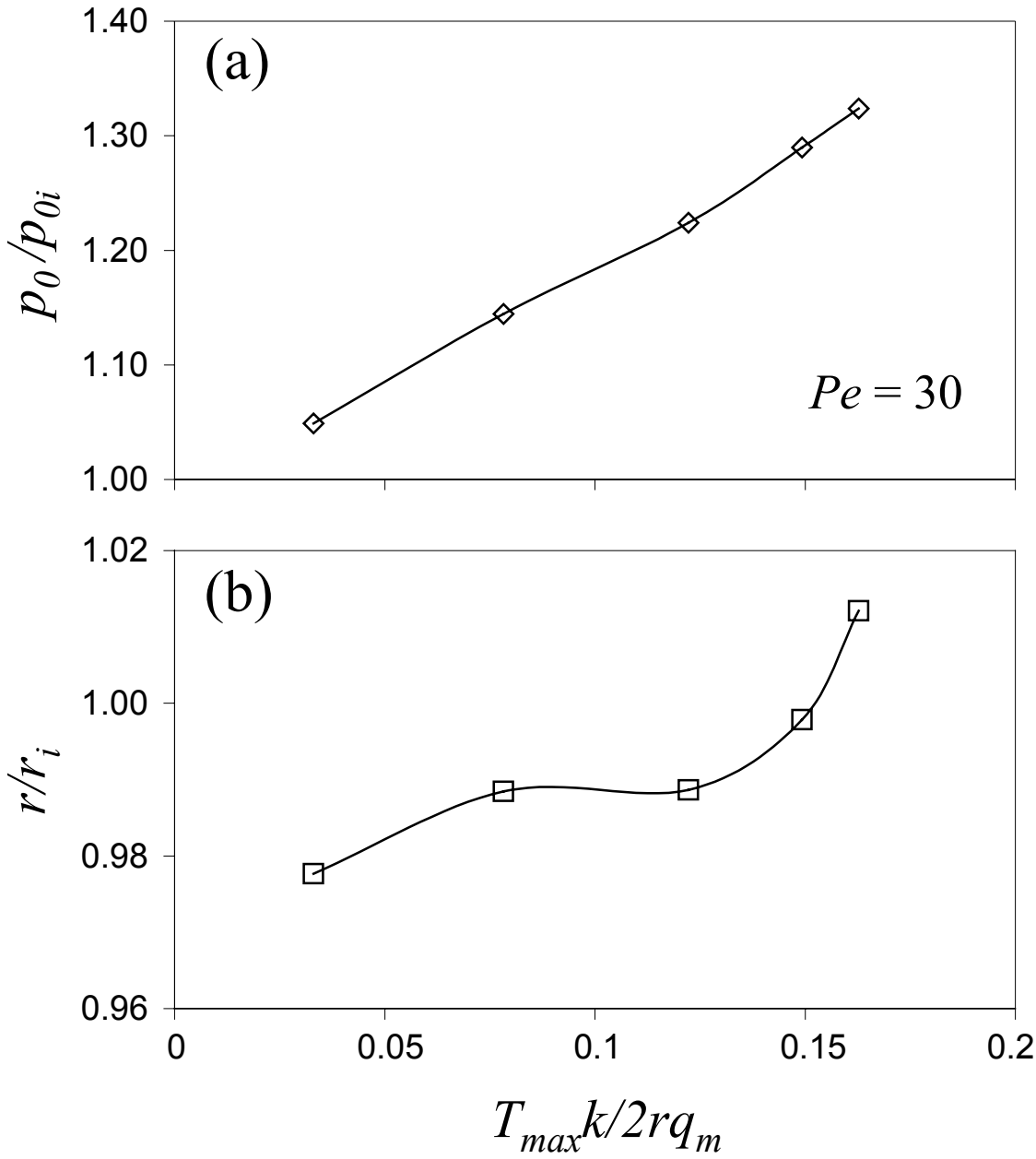

Figure 4.4 Variation of (a) maximum contact pressure and (b) contact radius with maximum temperature at the surface of an elastic-plastic homogeneous medium in sliding contact with an elastic sphere ($\eta = 1$, $f = 0.5$, and $Pe = 30$). (Subscript i denotes indentation.)

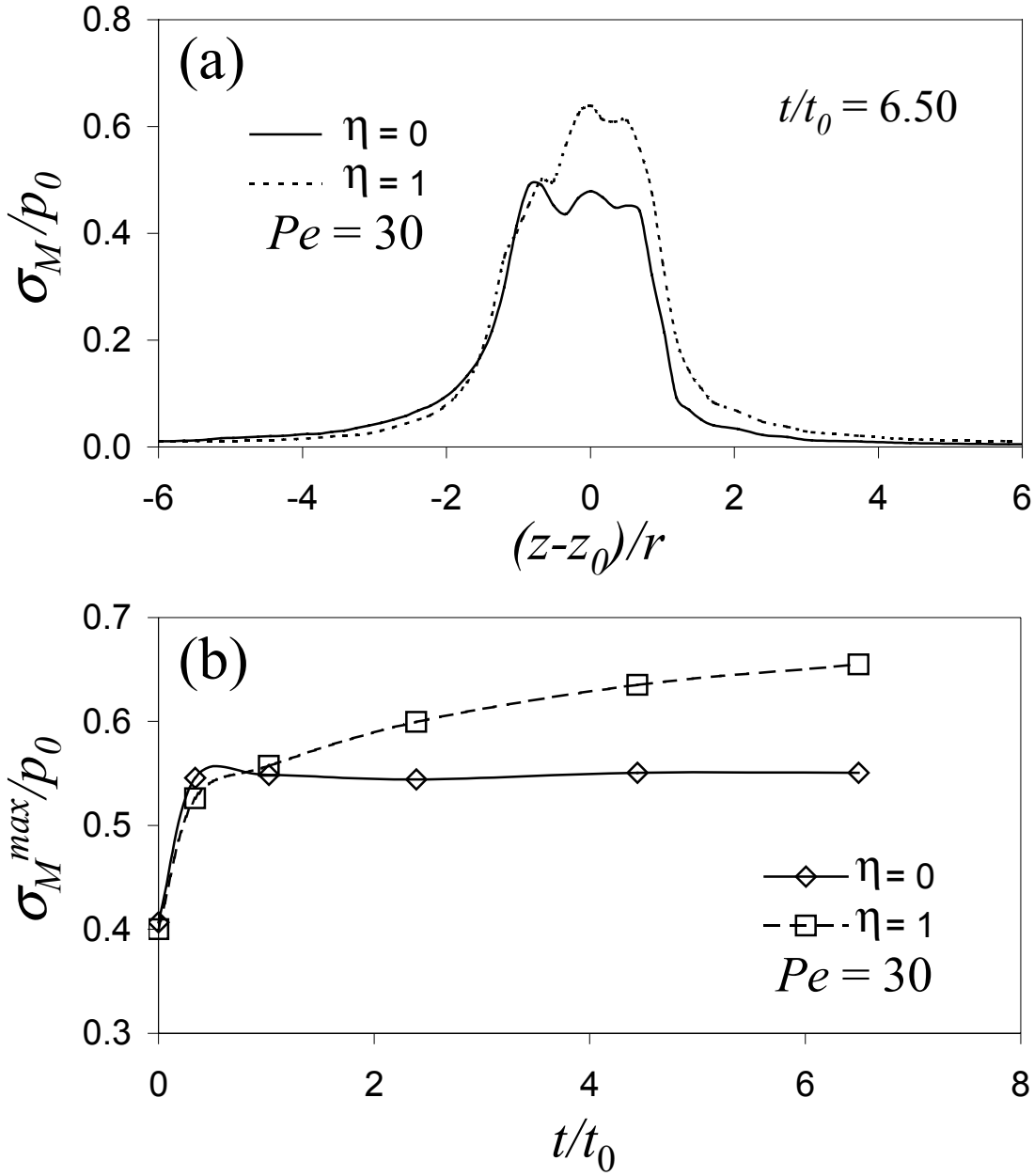

Figure 4.5 Comparison of thermomechanical (η = 1) and mechanical (η = 0) simulation results for an elastic-plastic homogeneous medium in sliding contact with an elastic sphere (f = 0.5 and Pe = 30): (a) von Mises equivalent stress distribution at the surface and (b) evolution of maximum von Mises equivalent stress.

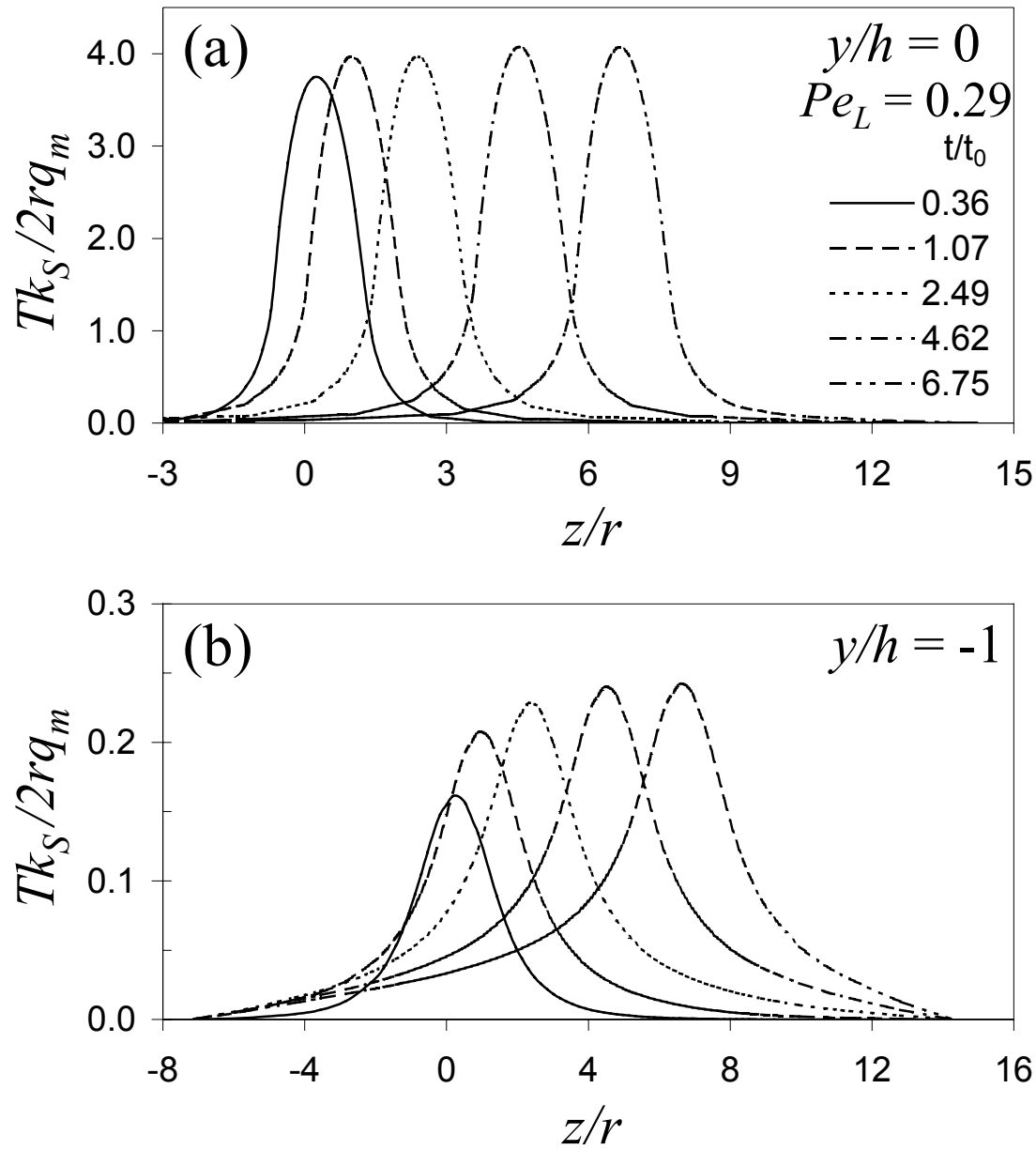

Figure 4.6 Evolution of temperature at the (a) surface ($y/h = 0$) and (b) interface ($y/h = -1$) of an elastic-plastic layered medium with layer thickness $h/R = 0.1$ and thermal conductivity $k_L = 5.2$ W/m·K in sliding contact with an elastic sphere ($\eta = 1$, $f = 0.5$, and $Pe_L = 0.29$).

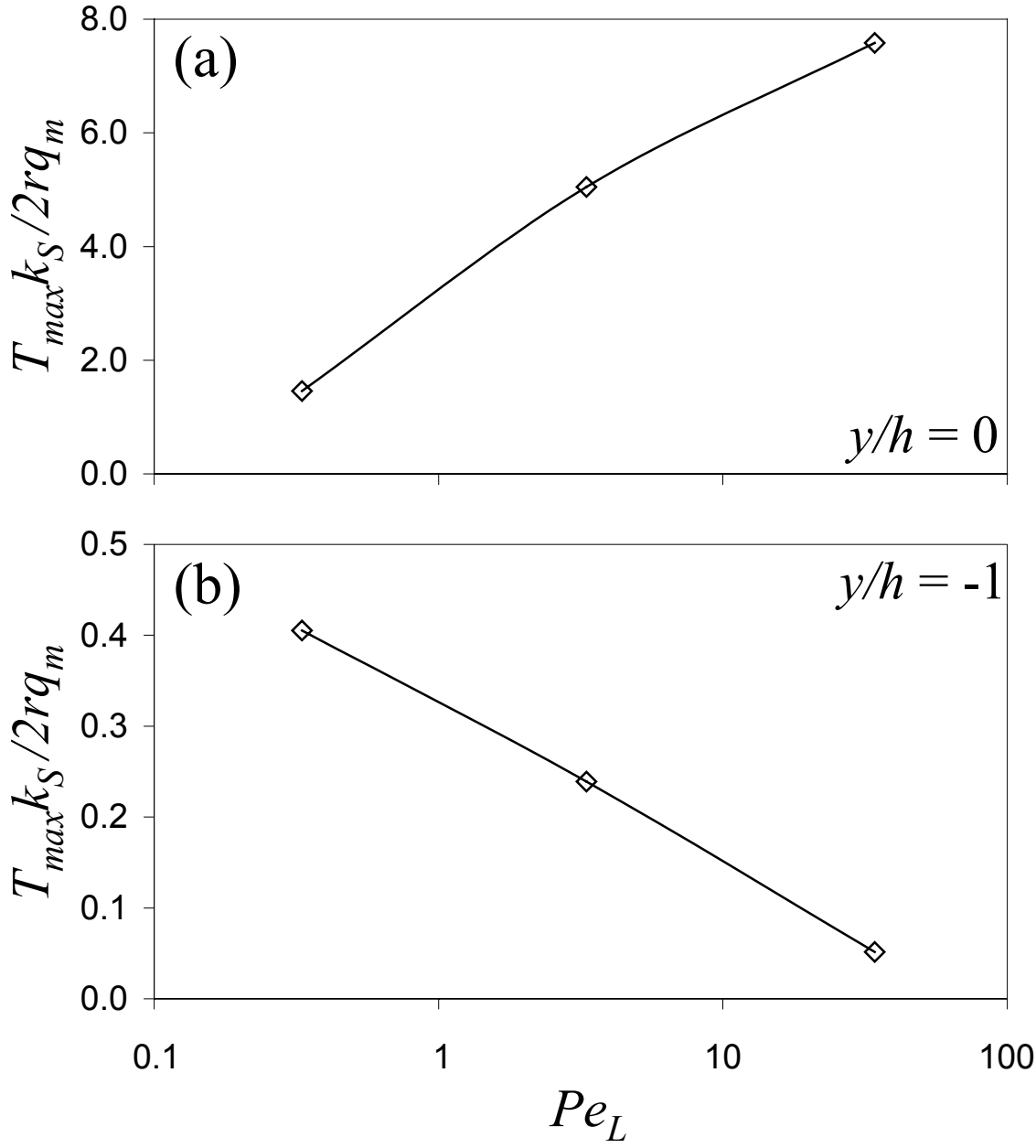

Figure 4.7 Effect of Peclet number on maximum temperature at (a) surface (y/h = 0) and (b) interface (y/h = –1) of an elastic-plastic layered medium with layer thickness h/R = 0.02 in sliding contact with an elastic sphere (η = 1 and f = 0.5).

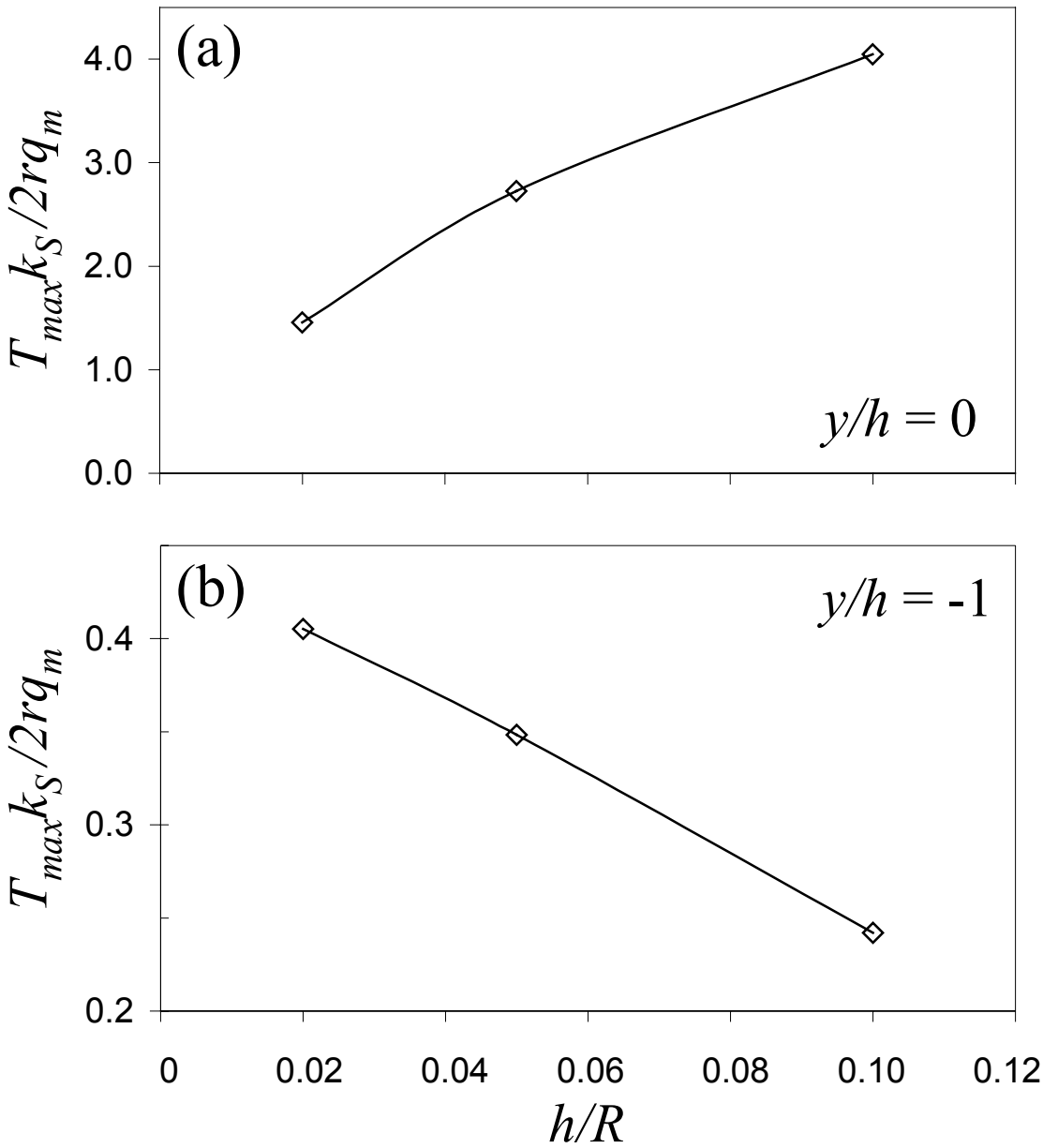

Figure 4.8 Effect of layer thickness on maximum temperature at (a) surface (y/h = 0) and (b) interface (y/h = –1) of an elastic-plastic layered medium with layer thermal conductivity k_L = 5.2 W/m·K in sliding contact with an elastic sphere (η = 1, f = 0.5, and $Pe_L \simeq 0.3$).

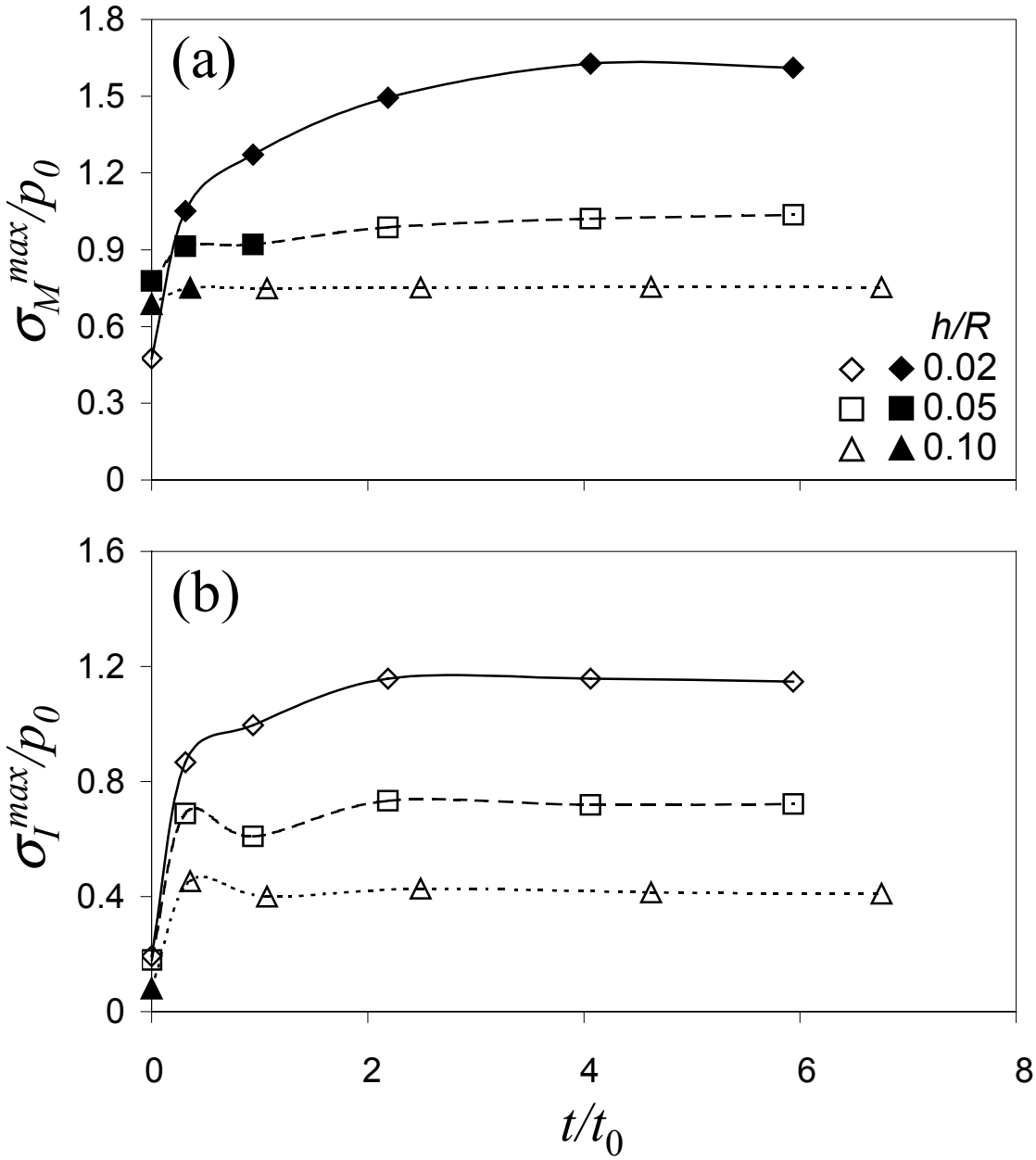

Figure 4.9 Evolution of (a) maximum von Mises equivalent stress and (b) maximum first principal stress in the layer of an elastic-plastic layered medium with layer thickness h/R = 0.02, 0.05, and 0.1 and thermal conductivity k_L = 5.2 W/m·K in sliding contact with an elastic sphere (η = 1, f = 0.5, and $Pe_L \simeq 0.3$). (Open and filled symbols denote the layer surface and interface, respectively.)

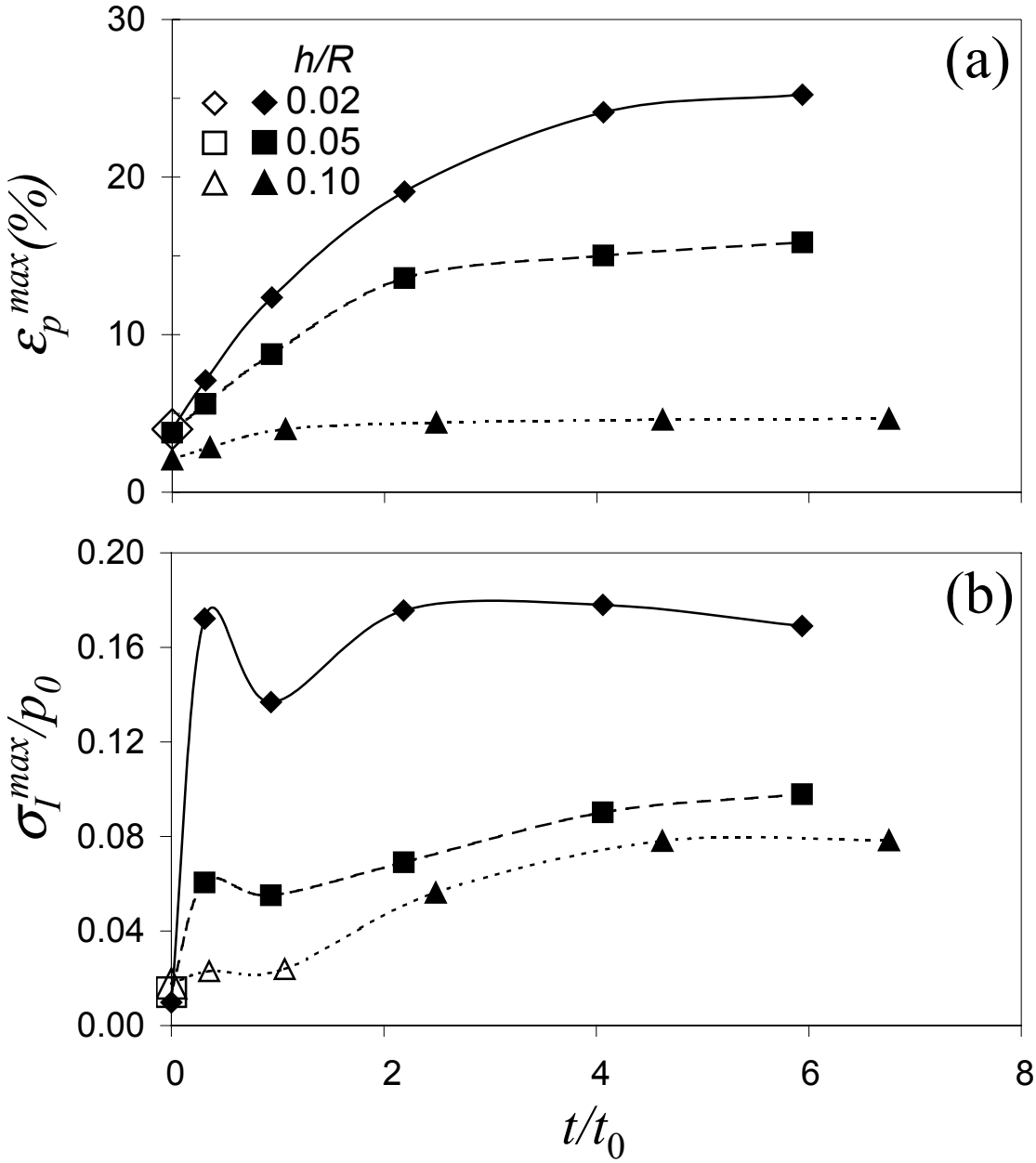

Figure 4.10 Evolution of (a) maximum equivalent plastic strain and (b) maximum first principal stress in the substrate of an elastic-plastic layered medium with layer thickness h/R = 0.02, 0.05, and 0.1 and thermal conductivity k_L = 5.2 W/m·K in sliding contact with an elastic sphere (η = 1, f = 0.5, and $Pe_L \simeq 0.3$). (Open and filled symbols denote the bulk and interface of the substrate, respectively.)

CHAPTER 5

EFFECT OF RESIDUAL STRESS IN SURFACE LAYER ON DEFORMATION OF ELASTIC-PLASTIC LAYERED MEDIA UNDER NORMAL AND SLIDING CONTACT TRACTION

5.1 Introduction

Residual stress due to manufacturing process exists in surfaces of many engineering applications. Surface property modification technique can generate residual stress, tensile stress during surface thermal quenching, and compressive stress resulting from shot peening and ion implantation. The importance of residual stress during thin-film deposition has become more and more significant as thin film media are widely used in integrated circuits, MEMS, and wear protection coatings on cutting tools or hard disks in computers. Both experimental and theoretical studies have been carried out to determine the origin and magnitude of residual stress and its effect on film properties and mechanical performance.

The presence of residual stress in thin films has been the focus of many experimental investigations, and several techniques have been developed to measure residual stress in thin films deposited on substrates. Nix (1989) summarized the common experimental techniques used to measure stresses in thin films including X-ray diffraction, optical inteferometry, and laser scanning. Mehregany et al. (1997) determined the tensile residual stress in 3C-SiC films from load-deflection measurements of suspended diaphragms. Kamiya et al. (1999) evaluated the residual stress distribution in

thin diamond films deposited on Si substrate by measuring the curvature and with the aid of Raman spectroscopy. The average intrinsic stress was found to be tensile, although a high compressive stress was observed in a very small region near the film/substrate interface. Lu and Komvopoulos (2000) proposed a technique for evaluating residual stresses in ultrathin films by using small amounts of Ar atoms implanted in the film as stress-sensing probes. This technique is especially useful when the film is only a few nanometers thick, where conventional techniques may not be suitable.

Machlin (1995) reviewed the various theories proposed to explain the intrinsic stresses that have been found in thin films. Most of the stresses in thin films exist because the film is bonded to a massive substrate. Thus, any change in length along the film plane (either due to thermal mismatch or lattice mismatch), which is not matched exactly by an equal change in length in the substrate, will result in a stress in the film. During non-energetic deposition of metal films, intrinsic stresses are usually tensile and their magnitudes can equal or exceed the yield strength values for the severely cold-worked state (Pulker, 1982, Martinez and Abermann, 1982, Abermann and Koch, 1980). This result may be explained on the basis that the yield strength in thin films exceeds that for bulk material for comparable conditions of dislocation density and grain size. A compressive intrinsic stress is found in films produced from condensation of energetic particles or grown under energetic particle bombardment. The maximum value of the compressive stress is again the yield strength, but in compression.

Serving as a wear protection overcoat is one of the most important applications of thin film. Therefore, experimental studies have been conducted to understand the correlation between residual stress and tribological performance of thin film. Kao et al.

(1989) investigated the mechanical and tribological characteristics of thin chromium oxide films by controlling the process parameters in reactive deposition and subsequent annealing. Their experimental results demonstrated that wear resistance was reduced by tensile residual stress, but was increased by a moderate compressive residual stress. Mounier et al. (1995), Mounier and Pauleau (1997) carried out ball-on-disk tribological tests on amorphous carbon films deposited by sputtering. The residual stresses in the films deposited on Si substrates were obtained from the change in the radius of curvature of substrates measured before and after deposition of films and the residual stresses were found to be compressive. They attribute severe damage and formation of a large quantity of wear debris in the wear tracks to high level of compressive residual stresses in a-C films. They further suggested that the residual stress level might affect the mechanical resistance and integrity of the deposited material, i.e., brittleness, fracture resistance or fragility, and also the adherence of a-C films to various substrates. A high level of tensile stresses can produce film and substrate cracking whereas excessive compressive stresses can lead to delamination of films from the substrate surface and formation of blister zone. Scharf and Barnard (1997) studied the wear and frictional behavior of ultrathin (25 nm) a:SiC/SiC-N overcoat using a depth sensing nanoindentation multiple sliding technique. They found that the presence of compressive residual stress improved the wear resistance for the SiC-N film. The improvement was attributed to the facts that compressive stress can close through thickness cracks and densify the microstructure. Herr and Broszeit (1997) investigated the effect of annealing process on the tribological properties of sputtered titanium, hafnium and chromium based nitride and boride layers on steel and titanium alloy substrate. The microhardness test results showed that hardness is higher in

films with higher compressive residual stress. However, high compressive stresses also resulted in premature failures during scratch test, which was proved by cracking and spalling at low critical loads. Kato et al. (1999) measured change in curvature of silicon substrates to detect internal stress in CN_x coating. Their wear tests showed that internal compressive stress reduced wear within the range of stress in their study. They suggested that a thin coating, after optimizing synthesis routine and processing conditions, may have a longer wear life if it has a suitable internal stress. Zhong et al. (2001) investigated the mechanical properties and tribological performance of the sputtered Ti-B-C-N films. Varying magnitudes of compressive residual stresses were found in films deposited at different substrate bias and with different argon-nitrogen atmospheres. The wear resistance was found to be inversely related to the compressive residual stress in the film measured using X-ray diffraction analysis.

Analytical and numerical approaches have also been applied to study residual stress effect. Hills and Ashelby (1982) determined and compared the elastic and shakedown limits for elastic homogeneous half space under sliding containing a cylindrical residual stress system using analytical solution given by Hamilton and Goodman (1966). The optimum value of compressive residual stress was found for different coefficient of friction. In their study, residual stress was assumed to be a constant along the depth direction of homogeneous half space. Mesarovic and Fleck (1999) performed finite element simulation to evaluate the role of residual stress within the elastic-ideally plastic half-space under spherical indentation. Indentation predictions are shown for the cases of vanishing pre-stress, equibiaxial tension of magnitude $s_Y/2$ and equibiaxial compression of magnitude $-s_Y/2$, where s_Y is the yield strength. For both the

similarity regime and the finite-deformation plasticity regime of indentation, residual stress has a negligible effect on the average contact pressure, on the normalized contact area, and on the contact stiffness. However, within the elastic-plastic indentation regime, the average contact pressure and normalized contact area decrease with increasing residual tension, while the contact stiffness is approximately independent of the initial stress state. While the overall plastic zone shape depends upon the level of pre-stress, the region of large strain (effective strain greater than 0.01) is practically identical in all three cases of pre-stress. Thus, pre-stress only has an effect in the vicinity of the elastic-plastic boundary, where elastic and plastic strains are of similar magnitude. Finite element method has been recently used to by Bai et al. (2000) to study the effect of internal stress on mechanical properties of thin films. The results of their simulation showed that the film with compressive internal stress has larger hardness and modulus than that without compressive internal stress; and vice versa if the internal stress is tensile.

It can be seen from the aforesaid studies that most of them are experimental, although they provided invaluable insight into the understanding of residual stress effect on tribological performance and mechanical properties of thin film, there is still a lack of a overall picture, as few theoretical studies were able to include layered media, elastic-plastic constitutive relationship, normal/sliding contact, and wide range of top layer internal stress. However, these aspects are key to promote understanding of internal stress effect on thin film used as tribological application, which is the main objective of this study. In order to achieve this, a three-dimensional finite element model was developed, and its accuracy was validated by favorable comparisons of simulation result with analytical solutions from previous study. Finite element results for the stresses, and

plastic strain in an elastic-plastic layered medium under normal and sliding contact are presented for different magnitudes of internal stress and coefficient of friction. The significance of internal stress and coefficient of friction the likelihood of the layered medium to undergo yielding and cracking are interpreted in the context of simulation results.

5.2 Finite Element Model

In the finite element model the spherical asperity was assumed to be rigid and the layered medium was modeled by three-dimensional, eight-node, linear hexahedron finite elements. In order to save the computation time only one-half of the sphere and the medium were modeled facilitated by the symmetric nature of the problem. The cross section at the symmetry plane $x = 0$ of the three-dimensional mesh of the finite element model is shown in Figure 5.1. The layered medium is discretized using 11,113 elements with a total of 15,006 nodes. To obtain accurate stress/strain field the mesh is refined in the region near the asperity as it indents in the negative y direction, and then slides along the positive z-direction. The x, y, z dimensions of the mesh normalized by the radius R of the rigid spherical asperity are 1, 0.976, and 3. The boundary conditions are as follows: the nodes on planes $x/R = 0$ and 1 were fixed against displacement in the x-direction, the nodes on plane $y/R = -0.976$ were fixed against displacement in the y-direction, and the nodes on planes $z/R = -1$ and 2 were fixed against displacement in the z-direction. The layered medium consists of a layer of thickness and a substrate, whose thickness and physical properties are given in Table 5.1. These data are typical of carbon overcoats and magnetic layers used in hard disks.

The interaction between the deformable layered medium and the rigid sphere is

modeled with finite-sliding formulation using contact elements. At each integration point these elements construct a measure of overclosure (interpenetration of the surfaces) and measures of relative shear sliding. These kinematic measures are then used, together with appropriate Lagrange multiplier techniques, to determine surface interactions: contact and friction.

The constitutive model of the normal interaction between the surfaces is defined as:

$$p = 0, \quad \text{for } d < 0, \quad \text{(no contact)} \tag{5.1a}$$

$$p = K\,d, \quad \text{for } d \geq 0, \quad \text{(contact)} \tag{5.1b}$$

where p is the contact pressure between two surfaces at a point, d is the overclosure of the surfaces K is the stiffness in stick, determined through an iterative procedure that satisfies equilibrium. The model given by Eq. (5.1) indicates that when the clearance between two surfaces reduces to zero, separated surfaces come into contact and the contact pressure assumes a nonzero value, which depends on the material properties and boundary conditions. When the two surfaces separate, the contact pressure reduces to zero.

Coulomb friction model is applied as the constitutive model of the sliding interaction to the surfaces. No relative motion or stick occurs if the shear stress t is less than the critical stress, t_{crit}, which is proportional to the contact pressure, p, in the form $t_{crit} = f\,p$, where f is the coefficient of friction. No relative motion is actually approximated by stiff elastic behavior. The stiffness is chosen such that the relative motion from the position of zero shear stress is bounded by the allowable maximum elastic slip, 0.5% of the average length of all contact elements in the model. If the shear stress is at the critical stress, macroscopic lateral movement or slip can occur. Thus, the

stick and slip conditions at the contact interface can be expressed as

$$t < f\,p \qquad \text{(stick)} \tag{5.2a}$$

$$t = f\,p \qquad \text{(slip)} \tag{5.2b}$$

Two values of coefficient of friction, 0.25 and 0.5, were specified to the contact elements in simulation cases.

When residual stress sr was introduced to the top layer, the stress state may not be an exact equilibrium state for the finite element model. Therefore, an initial step was included to allow ABAQUS to check for equilibrium and iterate, if necessary, to achieve equilibrium. Eight different magnitudes of sr were used and sr varied from –0.75 to +0.95 times the yield strength of the layer.

The constitutive relationship of both layer and substrate materials is assumed to be elastic-perfectly plastic, following yield criterion

$$s_M = \sqrt{\frac{3}{2} S_{ij} S_{ij}} = s_Y\,, \tag{5.3}$$

where s_M is the von Mises equivalent stress, S_{ij} is the deviatoric stress tensor ($S_{ij} = s_{ij} - s_{kk} d_{ij}/3$, where s_{ij} is the stress tensor and d_{ij} is Knonecker's delta function), and s_Y is the yield strength in uniaxial tension.

Two types of quasi-static simulations were performed with the multi-purpose finite element code ABAQUS: (a) normal contact involving indentation and unloading, and (b) sliding contact consisting of indentation, sliding, and unloading. Indentation of the layered medium by the asperity to a depth corresponding to a fixed normal load was modeled in one step of 21 to 24 increments each. Unloading was simulated in one step of 6 to 11 increments each. Sliding simulations comprised five incremental displacements

Dz/R = 0.05, 0.15, 0.35, 0.65, and 0.95 of the asperity under the given load in the *z* direction each having 11-19 increments. The typical computational time on a Pentium III 550 workstation was about 20,000 to 49,000 CPU seconds.

5.3 Model Validation

To examine the accuracy of the finite element model, a normal contact simulation was performed for an elastic homogeneous half-space indented by a rigid sphere. Figure 5.2 shows the variations of the von Mises equivalent stress and first principal stress at the surface along the *z*-direction ($x = y = 0$) predicted by the finite element model and the analytical solution of Huber (1904). The stresses are normalized by the maximum contact pressure p_0 and coordinate *z* by the contact radius *r*. The good agreement between the two methods indicates the validity of the finite element model and the correctness of the assumed boundary conditions for contact analysis.

5.4 Results and Discussions

A series of finite element simulations were performed with varying magnitudes of residual stress and coefficient of friction. Finite element simulation results are presented to illustrate the effect of residual stress and coefficient of friction on the stress and strain fields. Results from sliding simulation are given for *Dz/R* = 0.95. The locations of maximum stress and strain in the layered medium are listed in Tables 5.2 to 5.4.

To provide a general guideline to the FEM simulation, analytical approach was first applied to evaluate the effect of residual stress on subsurface stress field of elastic homogeneous half-space under normal Hertzian contact. As will be shown later, there are some similarities between the results for a homogeneous medium and a layered medium.

Varying magnitudes of equibiaxial residual stress (in the x and z directions) were superimposed to the normal contact stress field obtained from Huber's analysis (Huber, 1904). A MATLAB code was written to find the maximum von Mises stress and solve the eigenvalue problem to obtain the maximum first principal stress under different magnitudes of equibiaxial residual stress. Poisson ratio was assumed to be 0.3 and the result is plotted in Figure 5.3. To minimize von Mises stress, residual stress needs to be $-0.22p_0$, where p_0 is the peak contact pressure. Maximum first principal stress is suppressed to zero when residual stress is equal or smaller than $-0.13p_0$. It is noticed that when residual stress is zero the maximum first principal stress is $0.13p_0$. This is not a coincidence, because the maximum first principal stress lies in the same direction as that of the residual stress, and a compressive residual stress can cancel out the tensile stress induced by indentation. Therefore, for elastic homogeneous half-space under normal Hertzian contact, the optimal equibiaxial residual stress is $-0.22p_0$ to minimize the possibilities of yielding and crack initiation.

The results of FEM simulation of layered medium under normal and sliding contact with rigid sphere are displayed in Figures 5.4 to 5.9. Figure 5.4 through 5.6 are results in the layer.

Figure 5.4 shows the dependence of maximum von Mises stress in the layer on residual stress during indentation, sliding, and unloading. During indentation, similar to the analytical result of homogeneous half space, there is an optimal value of compressive residual stress to minimize the maximum von Mises stress and the value is between $-0.25p_0$ and $-0.5p_0$. The effect of friction is negligible for indentation. During unloading after indentation, sliding at $f = 0.25$, and unloading after sliding at $f = 0.25$, the von Mises

stress is minimum for residual stress close to zero. However, the residual stress does not affect the maximum von Mises stress during sliding at f = 0.5 and the subsequent unloading. This is actually because yielding occurs in the layer at higher friction, and the maximum von Mises stress cannot increase beyond yield strength even under larger residual stress. The effect of coefficient of friction is insignificant during indentation and subsequent unloading, mainly because of the limited relative slipage between the contacting surfaces. During sliding, the higher coefficient of friction is expected to lead to higher von Mises stress; however, it is noticed that at high magnitudes of residual stress (either tensile or compressive) there is no difference between the value of maximum von Mises stress for f = 0.25 and 0.5. This is also due to yielding in the layer under larger residual stress during sliding.

To better illustrate the effect of residual stress and coefficient of friction during sliding after yielding occurs, the maximum equivalent plastic strain in the layer varying with the magnitude of residual stress is shown in Figure 5.5. No re-yielding occurs during the subsequent unloading after sliding. It is shown that neither compressive nor tensile residual stress reduces the plastic strain in the layer material. So, from maximum plastic strain point of view, the optimal residual stress is zero, or smaller than $|0.5p_0|$ for f = 0.25. Higher coefficient of friction generates higher plastic strain and the increase at a given residual stress is approximately the same. The location of the maximum equivalent plastic strain during sliding was found to be at the surface of the layer for tensile residual stress, and at the layer/substrate interface for zero or compressive residual stress.

The dependence of the maximum first principal stress in the layer on residual stress is shown in Figure 5.6. Maximum first principal stress is considered to be

responsible for crack initiation especially in a brittle material. After unloading following indentation, the maximum first principal stress remains approximately the same (Fig. 5.6(a)). This is caused by the development of plasticity mainly in the substrate, and after unloading the plastic zone places a constraint to the surrounding elastic region. The overall trend during indentation closely resembles that of the analytical result (Fig. 5.3), however, the compressive stress required to suppress the maximum first principal stress increases to around $-0.4p_0$, which is needed to cancel out the maximum first principal stress at residual stress equal to zero. It is noticed that this magnitude is higher than that in homogeneous half space ($0.13p_0$). This is because of the effect of lower Young's modulus and strength of the substrate. The more compliant and plastically deformed substrate cannot provide a strong support to the layer; therefore, the layer deforms more than if it was supported by a stronger material like itself, and hence encounters higher stress. It is the larger elastic and plastic deformation in the substrate that causes the increase of the maximum first principal stress in the layer. When sliding occurs, for f = 0.25, the residual stress has to increase to $-p_0$ to suppress the maximum first principal stress close to zero. This increase is caused by the added shear stress component during sliding. For f = 0.5, increasing the residual stress cannot suppress the maximum first principal stress in the layer to zero any more. This is caused by the larger plastic deformation in the substrate, which can be seen from the location of maximum first principal stress. During sliding, the maximum first principal stress location is always at the layer surface for f = 0.25, but for high level of compressive residual stress and f = 0.5, the maximum stress location shifts to the layer/substrate interface. During indentation, the maximum first principal stress is found to be at the layer surface for zero or tensile

residual stress, and in the bulk of the layer for compressive residual stress. During unloading after indentation, the maximum first principal stress location is always the layer/substrate interface. The results shown in Figs. 5.5 and 5.6 demonstrate the important role of the residual stress on the resistance against plastic deformation and cracking of layered media subjected to normal and sliding contact.

The stress and strain results in the substrate are shown in Figures 5.7 to 5.9.

Figure 5.7 shows the dependence of the maximum von Mises stress on the residual stress in the layer after unloading from indentation and sliding for f = 0.25 and 0.5. It is noticed that after unloading from indentation there is an optimal "tensile" residual stress (around p_0) that minimizes the maximum von Mises stress. After unloading from sliding, the higher coefficient of friction raises the maximum von Mises stress, which is expected because of the larger plastic deformation occurring mainly in the substrate at higher coefficient of friction (as shown in Figure 5.8). Tensile is put in quotation marks because tensile residual stress in the layer is actually compressive in the substrate. With this in mind, Figs. 5.8 and 5.9 can also be easily understood. Upon unloading from indentation or sliding, for all magnitudes of residual stress, the maximum von Mises stress is located at the layer/substrate interface.

Figure 5.8 shows the maximum equivalent plastic strain versus the residual stress. Again, the coefficient of friction only affects the plastic strain during sliding. Higher coefficient of friction renders larger plastic strain and the increase amount is about the same at different magnitude of residual stress. During indentation and sliding with f = 0.25, a tensile residual stress in the layer of ~ $1.5p_0$ minimizes the plastic deformation in the substrate. This trend is similar to that of as the maximum von Mises stress in

homogeneous medium (Fig. 5.3) as tensile residual stress in the layer is balanced by a compressive stress in the substrate. Therefore, plastic deformation in the substrate is minimized by compressive stress in the substrate. During sliding, the maximum equivalent plastic strain is located at the interface between the layer and substrate for both $f = 0.25$ and 0.5.

In Fig. 5.9 the maximum first principal stress is plotted as a function of the residual stress. The significance of coefficient of friction is only shown during sliding and the following unloading. It is noticed that s_I^{max} is higher after unloading than during sliding. This is caused by the mismatch unloading of elastic and plastic regions in the substrate. Plastic zones are in both the layer and substrate. Also, elastic recovery is different in the layer and substrate ($E_l > E_s$). During sliding and the unloading afterwards, the maximum first principal stress is always located at the interface between the layer and substrate for both $f = 0.25$ and 0.5.

To further illustrate the effect of friction and residual stress on plastic deformation, a comparison of plastic zones during sliding for different coefficient of friction and residual stress is shown in Fig. 5.10 to 5.13. The spherical sliding asperity starts from position 1 and stops at position 2. At a given coefficient of friction, increasing the magnitude of residual stress (either tensile or compressive) enlarges the plastic zone in the layer, although tensile stress has a more significant effect than compressive stress. However, the depth of the plastic zone in the substrate is increased by higher compressive stress in the layer (balancing tensile stress in the substrate). Higher coefficient of friction renders larger plastic zones in both the layer and substrate, more noticeably in the layer, which is apparently because the substrate is separated from the sliding asperity by the

layer. It is also noticed that tensile (compressive) residual stress tends to induce larger plastic zone at the trailing (front) edge along the sliding direction. This can be explained by the fact that during sliding, the dominant stress generated by shear force at the trailing (front) edge is tensile (compressive). Therefore, tensile (compressive) residual stress helps enlarge plastic deformation at the trailing (front) edge.

5.5 Conclusions

A three-dimensional finite element analysis for normal & sliding contact of elastic-plastic layered media was performed in order to elucidate the role of the residual stress in the surface layer (overcoat) and coefficient of friction on the evolution of stress and strain fields. Based on the presented results and discussion, the following main conclusions can be drawn.

(1) A three-dimensional finite element model for contact analysis was developed and validated by comparison of simulation results those obtained from an elastic normal contact analysis.

(2) In the surface layer, the maximum first principal stress increases (decreases) with tensile (compressive) residual stress.

(3) During indentation, the location of the maximum first principal stress in the layer shifts from the bulk to the surface of the layer as the residual stress changes from compressive to zero and tensile.

(4) During indentation, the effect of coefficient of friction is negligible.

(5) During sliding, the magnitude of optimal residual stress depends on the coefficient of friction. Higher coefficient of friction promotes plasticity and intensifies the maximum first principal stress in both the layer and substrate media.

(6) During sliding, the location of maximum plastic strain in the substrate is always at the interface between the layer and substrate. The location of maximum plastic strain in the layer shifts from the interface between the layer and substrate to the surface of the layer as the residual stress changes from compressive to tensile.

(7) During unloading, unmatched elastic relaxation between plastic and elastic regions in the substrate generates a higher maximum first principal stress than that during sliding.

(8) During sliding and unloading, the location of the maximum first principal stress in the substrate is always at the interface between the layer and substrate.

(9) The optimal value of normalized residual stress s_r/p_0 depends on the type of contact (normal or sliding), coefficient of friction, and deformation mode of the overcoat, i.e., plastic deformation or cracking.

Table 5.1. Thickness and properties of layer and substrate media of the finite element model.

Medium	Layer	Substrate
Thickness, h/R	0.02	0.956
Elastic modulus, E (GPa)	168	130
Poisson ratio, n	0.3	0.3
Yield strength, s_Y (GPa)	13	2.67

Table 5.2. Location of maximum von Mises stress s_M^{max}.

Material	Step	f	s_r/p_0							
			-1.60	-1.04	-0.51	0.00	0.49	0.95	1.43	1.88
Layer	indentation	0.25	I	I	I	I	I	I	N/A	N/A
		0.5	I	I	I	I	I	I	N/A	N/A
	unloading	0.25	I	I	I	I	I	I	I	S
		0.5	I	I	I	I	I	I	S	S
	sliding	0.25	N/A	N/A	I	S	S	N/A	N/A	N/A
		0.5	N/A	N/A	N/A	N/A	N/A	N/A	N/A	N/A
	unloading	0.25	S	I	I	I	I	I	S	S
		0.5	S	I	I	I	I	I	S	S
Substrate	indentation	0.25	N/A	N/A	N/A	N/A	N/A	N/A	N/A	N/A
		0.5	N/A	N/A	N/A	N/A	N/A	N/A	N/A	N/A
	unloading	0.25	I	I	I	I	I	I	I	I
		0.5	I	I	I	I	I	I	I	I
	sliding	0.25	N/A	N/A	N/A	N/A	N/A	N/A	N/A	N/A
		0.5	N/A	N/A	N/A	N/A	N/A	N/A	N/A	N/A
	unloading	0.25	I	I	I	I	I	I	I	I
		0.5	I	I	I	I	I	I	I	I

I: layer/substrate interface, S: layer surface, N/A: yielding has occurred, multiple points have reached yield strength

Table 5.3. Location of maximum equivalent plastic strain e_p^{max}.

Material	Step	f	s_r/p_0							
			-1.60	-1.04	-0.51	0.00	0.49	0.95	1.43	1.88
Layer	indentation	0.25	N/A	N/A	N/A	N/A	N/A	N/A	I	I
		0.5	N/A	N/A	N/A	N/A	N/A	N/A	I	I
	unloading	0.25	N/A	N/A	N/A	N/A	N/A	N/A	I	I
		0.5	N/A	N/A	N/A	N/A	N/A	N/A	I	I
	sliding	0.25	I	I	N/A	N/A	S	S	S	S
		0.5	I	I	I	I	S	S	S	S
	unloading	0.25	I	I	N/A	N/A	S	S	S	S
		0.5	I	I	I	I	S	S	S	S
Substrate	indentation	0.25	B	B	B	B	B	B	I	I
		0.5	I	I	I	B	B	B	I	I
	unloading	0.25	B	B	B	B	B	B	I	I
		0.5	I	I	I	B	B	B	I	I
	sliding	0.25	I	I	I	I	I	I	I	I
		0.5	I	I	I	I	I	I	I	I
	unloading	0.25	I	I	I	I	I	I	I	I
		0.5	I	I	I	I	I	I	I	I

N/A: yielding has not occurred

Table 5.4. Location of maximum first principal stress s_I^{max}.

Material	Step	f	s_r/p_0							
			-1.60	-1.04	-0.51	0.00	0.49	0.95	1.43	1.88
Layer	indentation	0.25	B	B	B	S	S	S	S	S
		0.5	B	B	B	S	S	S	S	S
	unloading	0.25	I	I	I	I	I	I	I	I
		0.5	I	I	I	I	I	I	I	I
	sliding	0.25	S	S	S	S	S	S	S	S
		0.5	I	I	S	S	S	S	S	S
	unloading	0.25	S	I	I	I	I	I	I	S
		0.5	I	I	I	I	I	I	S	S
Substrate	indentation	0.25	I	I	I	B	B	I	I	I
		0.5	I	I	I	B	B	I	I	I
	unloading	0.25	I	I	I	B	I	I	I	I
		0.5	I	I	I	I	I	I	I	I
	sliding	0.25	I	I	I	I	I	I	I	I
		0.5	I	I	I	I	I	I	I	I
	unloading	0.25	I	I	I	I	I	I	I	I
		0.5	I	I	I	I	I	I	I	I

B: bulk of layer or substrate

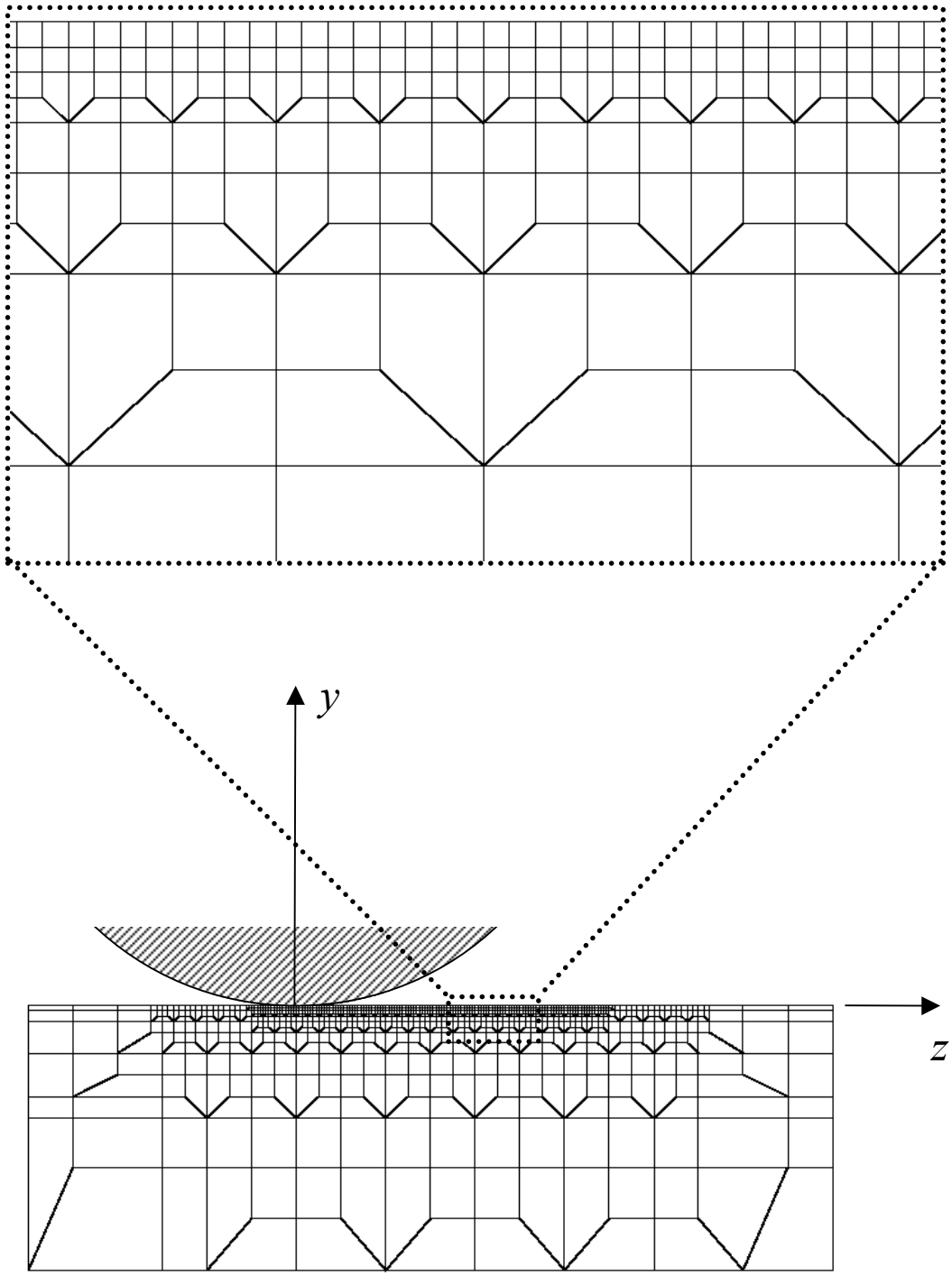

Figure 5.1 Cross section ($x = 0$) of three-dimensional finite element mesh used in the normal/sliding contact simulations and a detail view of the mesh near the surface.

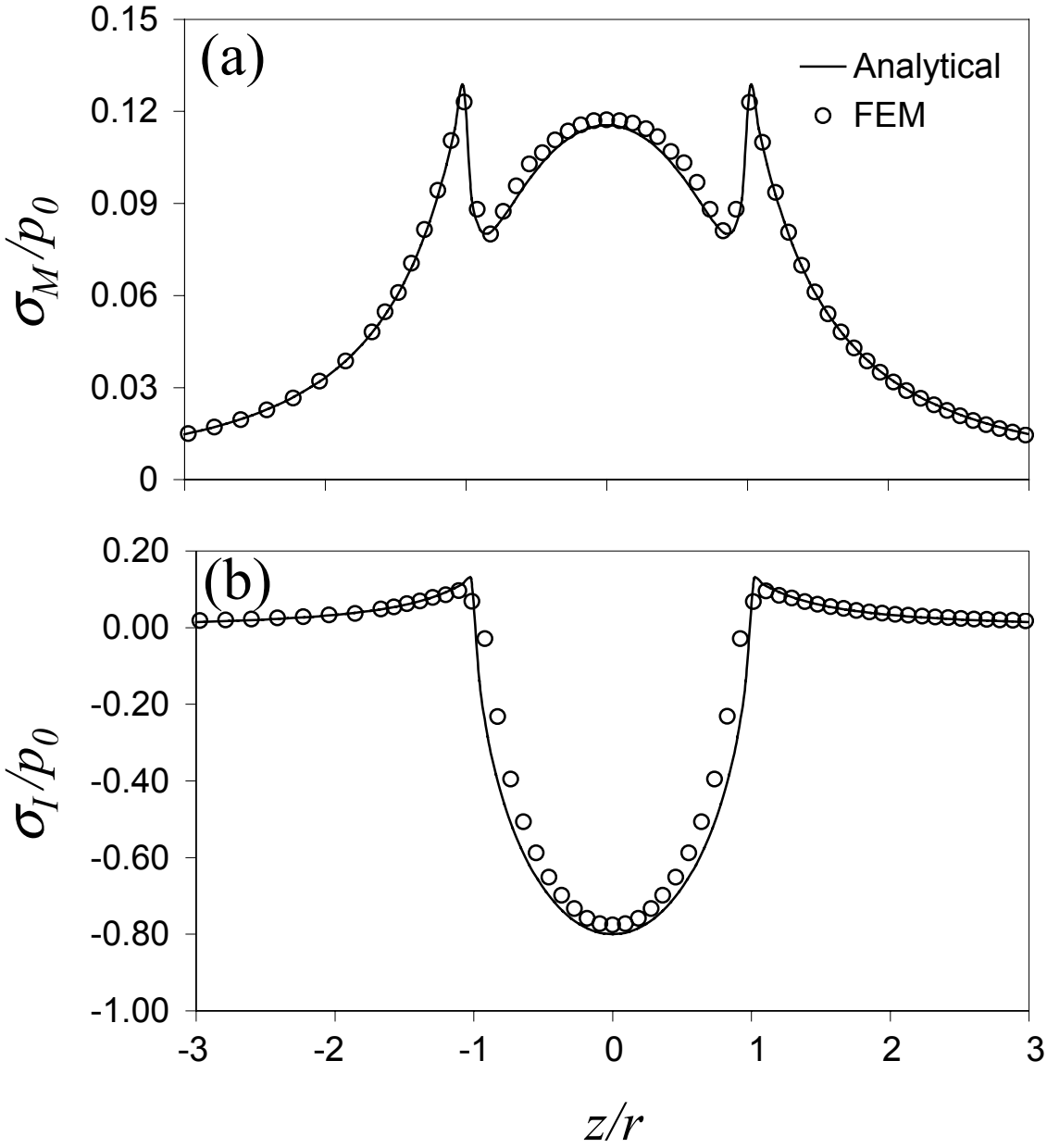

Figure 5.2 Comparison of finite element and analytical results for (a) von Mises stress and (b) first principal stress at the surface of on an elastic homogeneous medium indented by a rigid sphere.

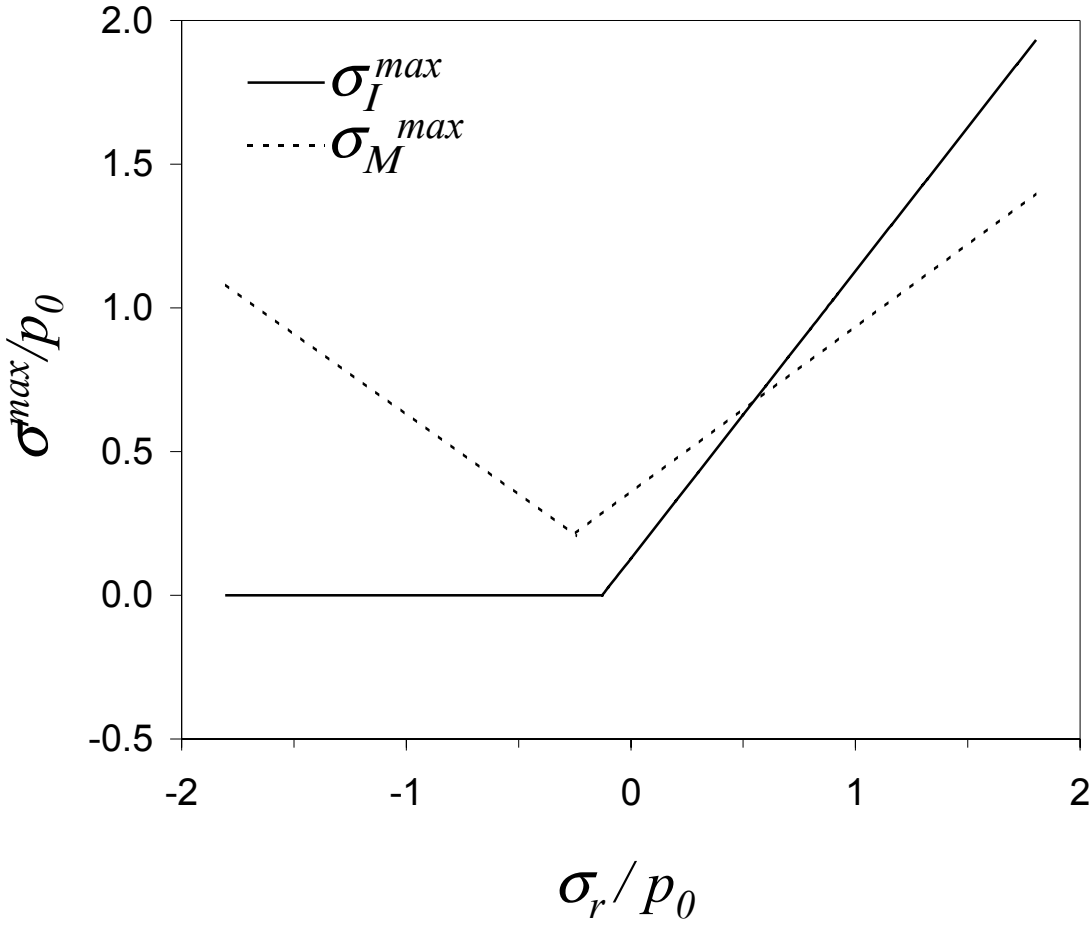

Figure 5.3 Maximum von Mises equivalent stress and maximum first principal stress versus residual stress in an elastic homogeneous half-space subjected to Hertizan normal traction.

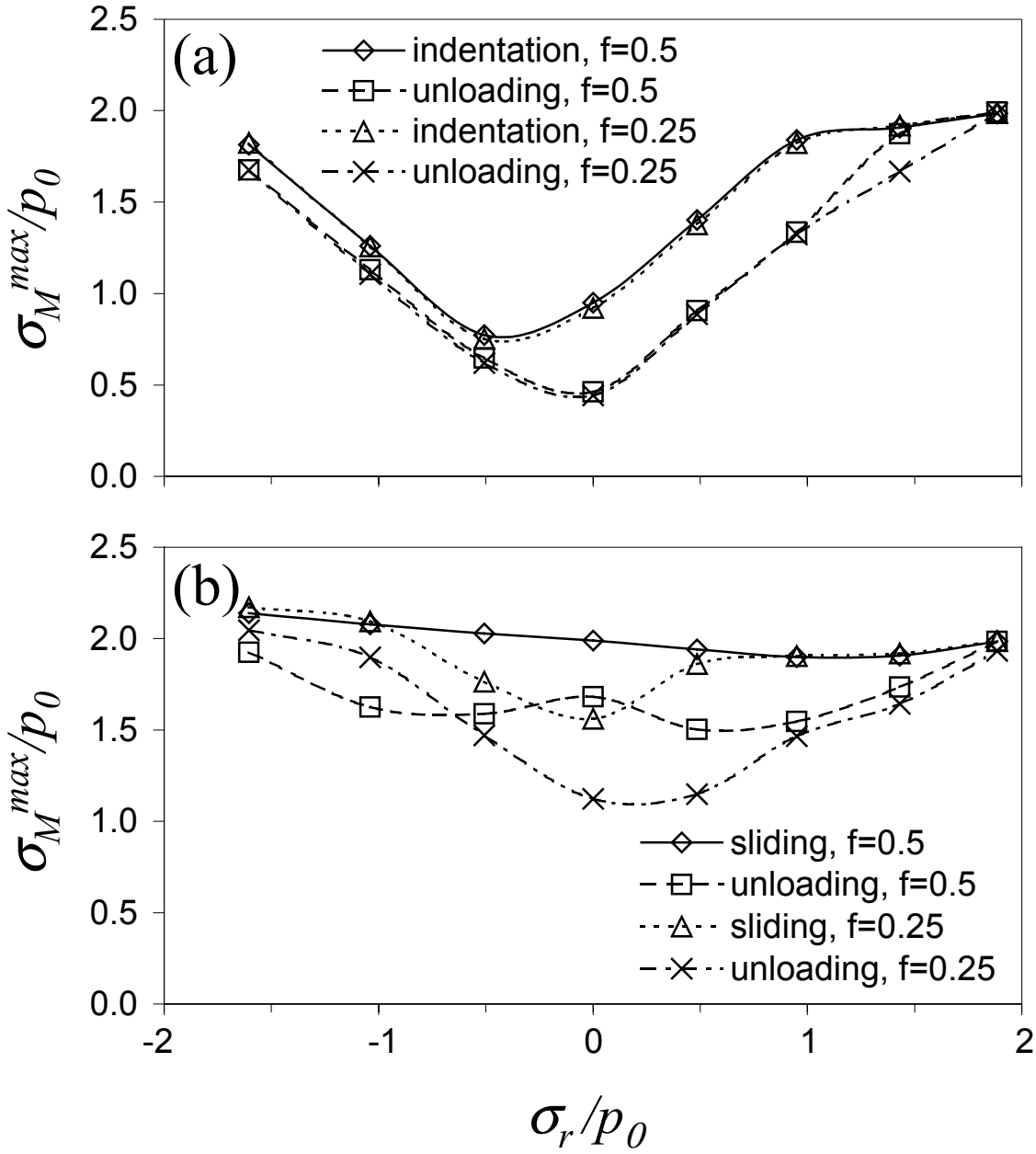

Figure 5.4 Maximum von Mises equivalent stress in the layer of an elastic-plastic layered medium in contact with a rigid sphere versus residual stress for f = 0.25 and 0.5: (a) indentation and unloading, and (b) sliding and unloading.

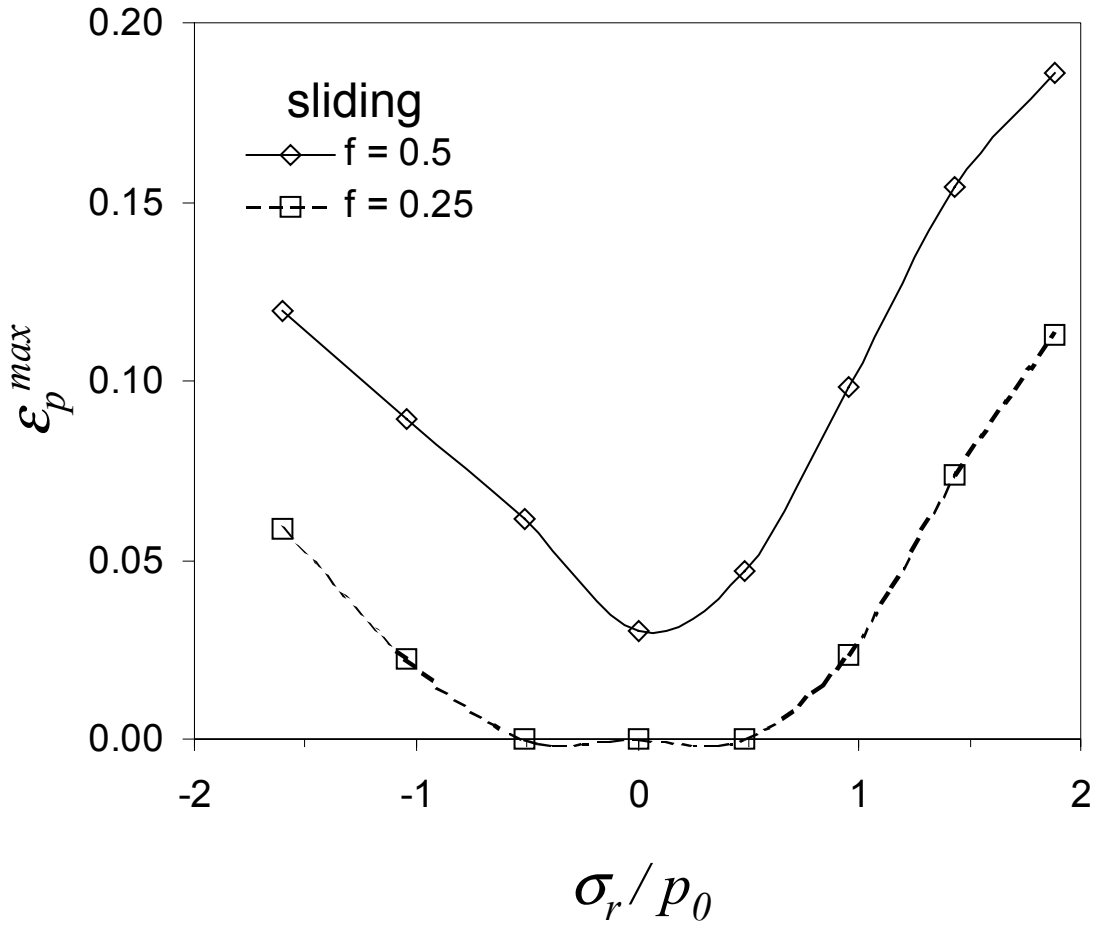

Figure 5.5 Maximum equivalent plastic strain in the layer of an elastic-plastic layered medium in sliding contact with a rigid sphere versus residual stress for f = 0.25 and 0.5.

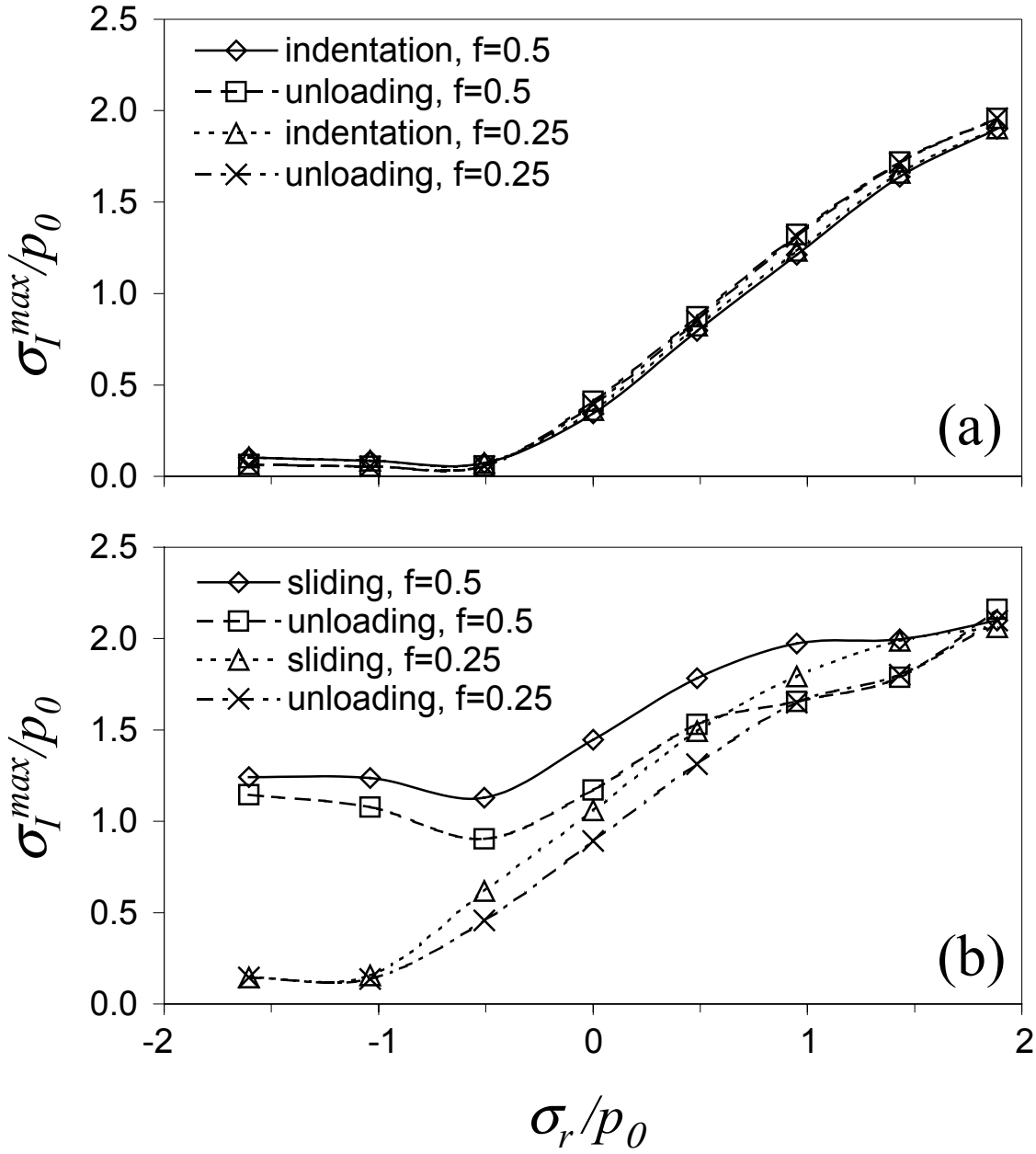

Figure 5.6 Maximum first principal stress in the layer of an elastic-plastic layered medium in contact with a rigid sphere versus residual stress for f = 0.25 and 0.5: (a) indentation and unloading, and (b) sliding and unloading.

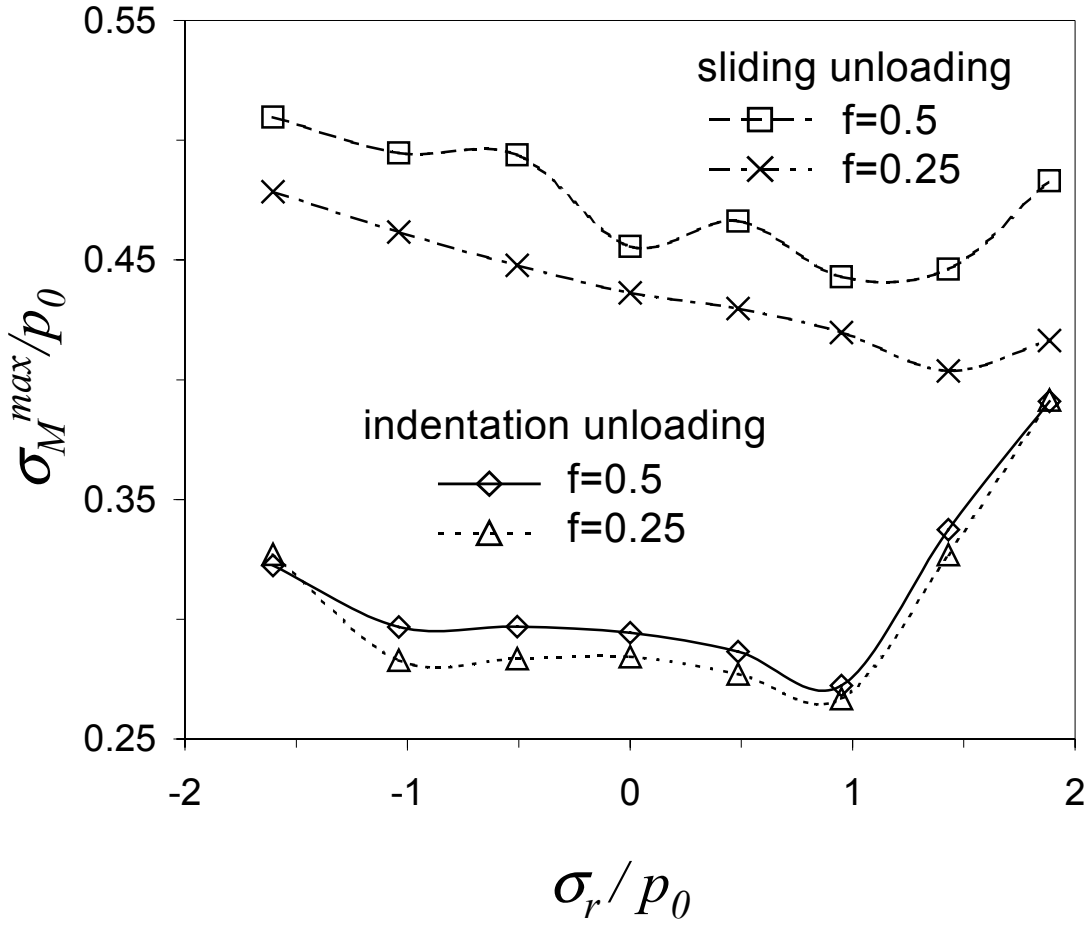

Figure 5.7 Maximum von Mises equivalent stress in the substrate of an elastic-plastic layered medium in contact with a rigid sphere versus residual stress after unloading from indentation and sliding for f = 0.25 and 0.5.

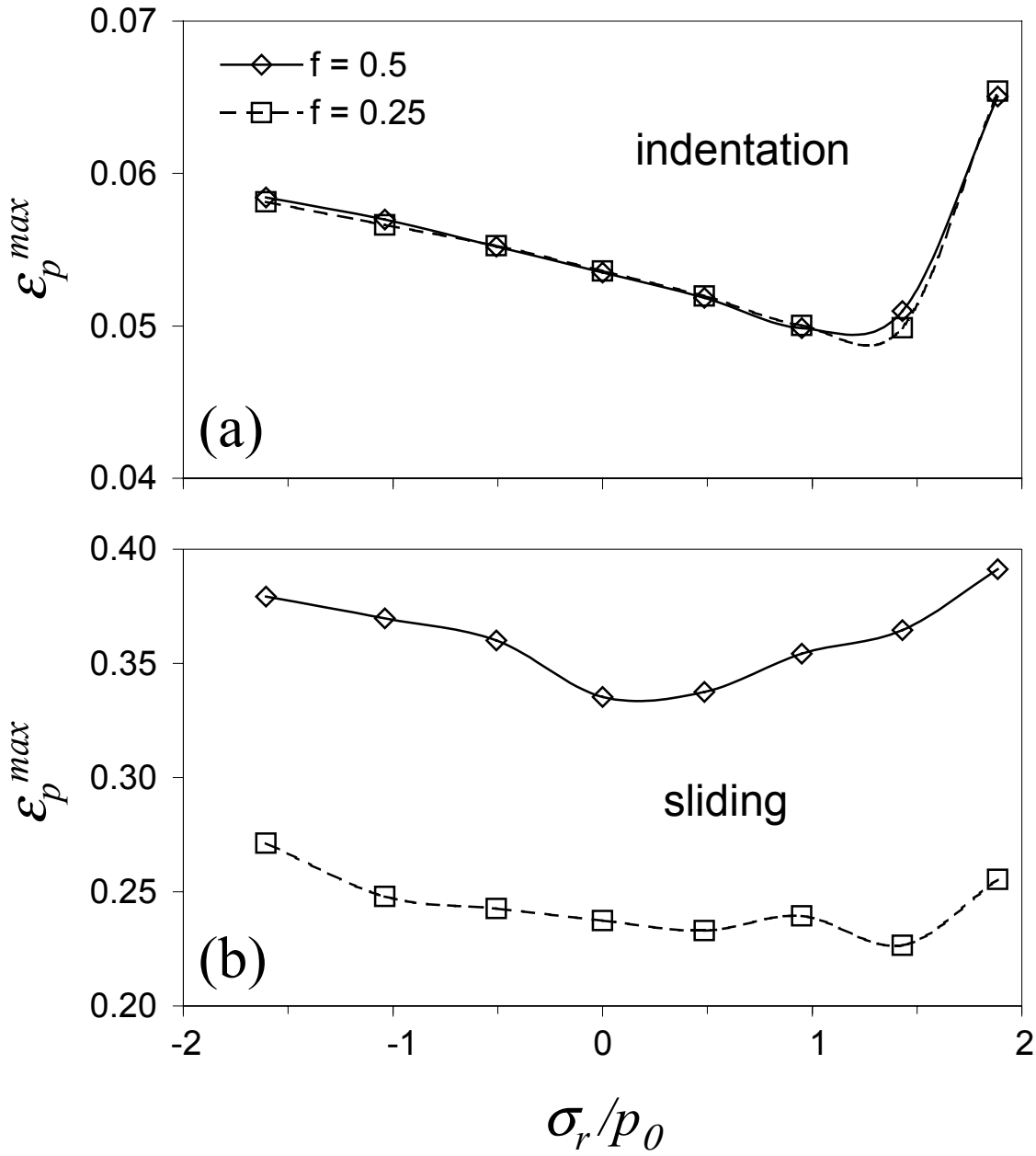

Figure 5.8 Maximum equivalent plastic strain in the substrate of an elastic-plastic layered medium in contact with a rigid sphere versus residual stress for f = 0.25 and 0.5: (a) indentation, and (b) sliding.

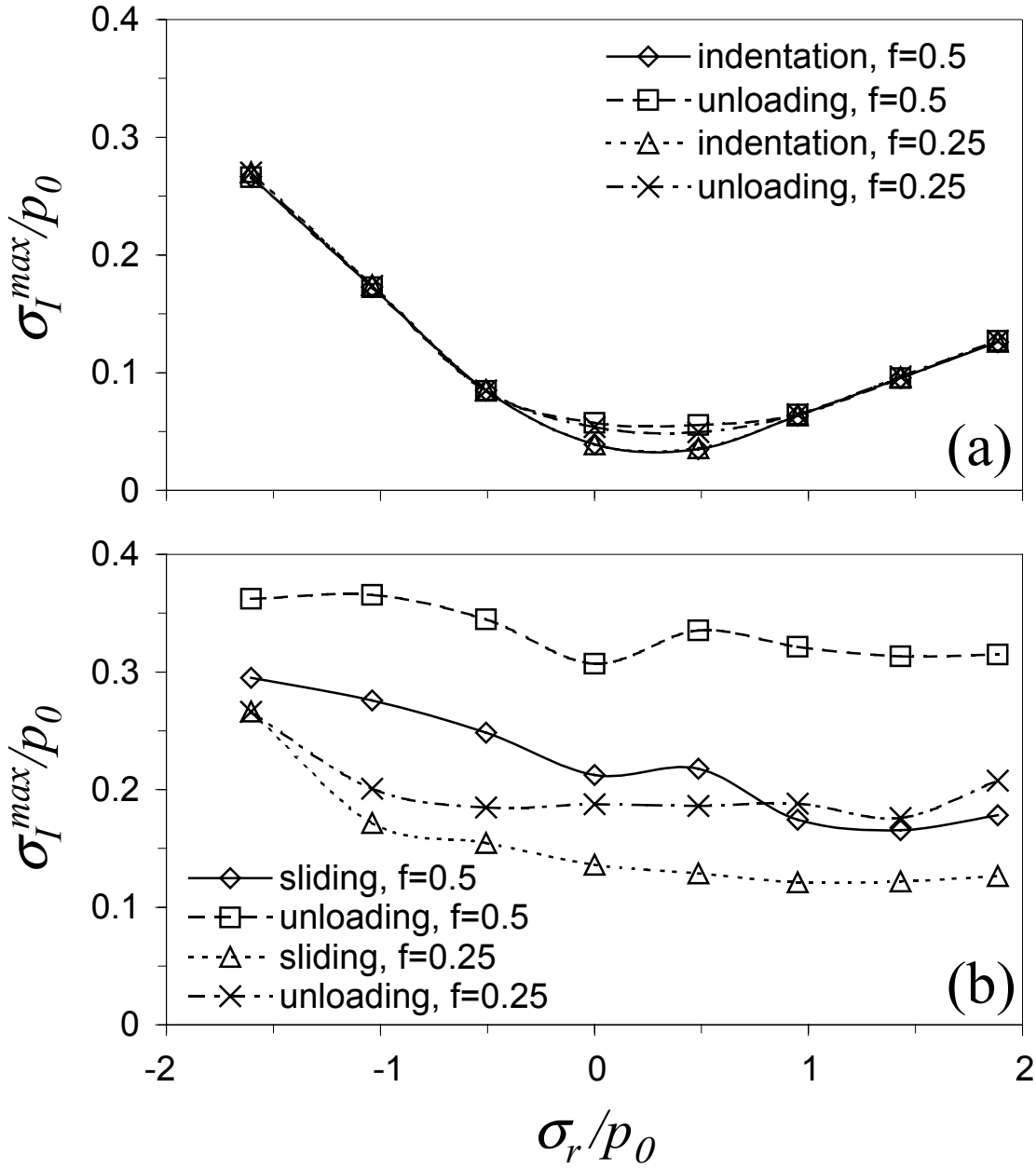

Figure 5.9 Maximum first principal stress in the substrate of an elastic-plastic layered medium in contact with a rigid sphere versus residual stress for f = 0.25 and 0.5: (a) indentation and unloading, and (b) sliding and unloading.

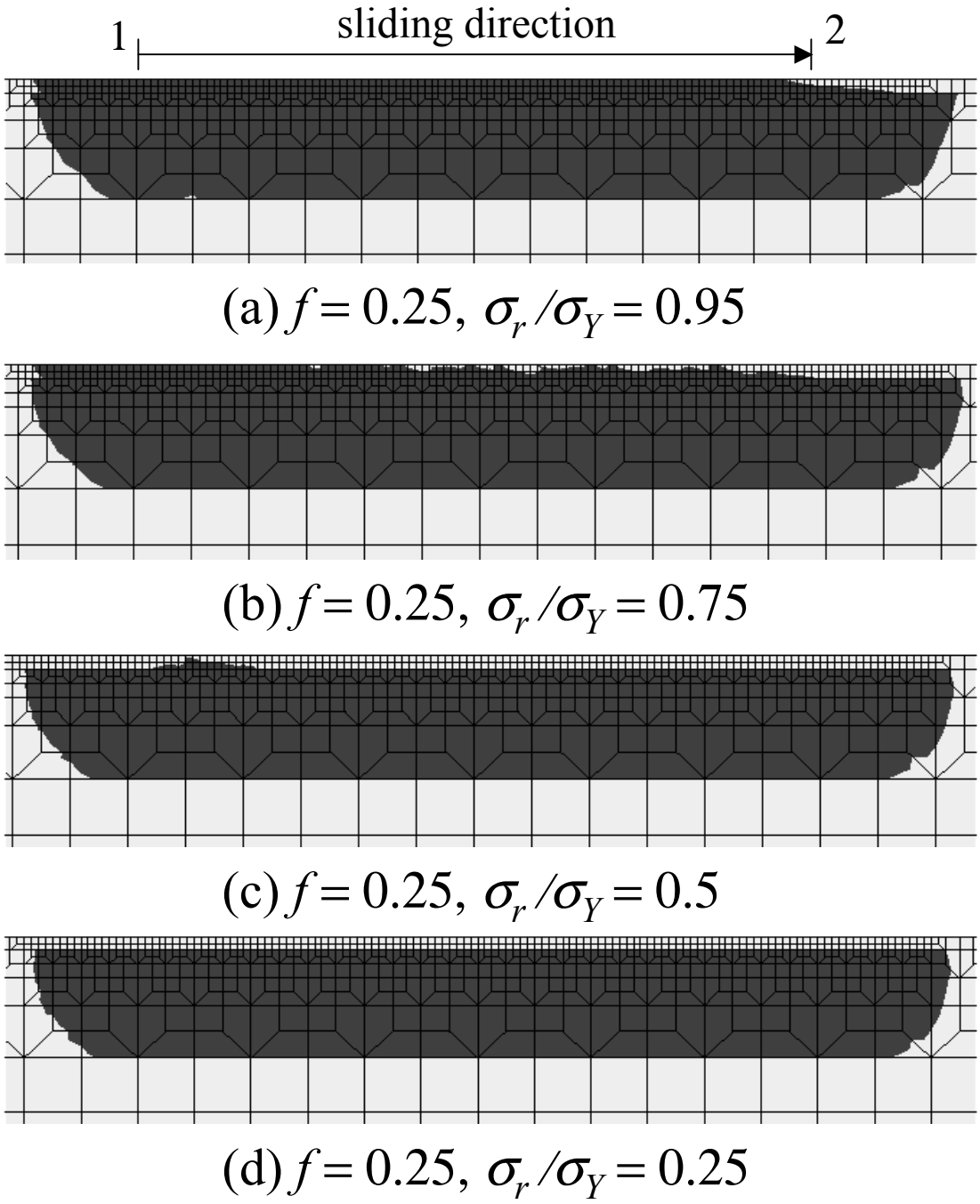

Figure 5.10 Comparison of plastic zones during sliding in a layered medium with f = 0.25: (a) $\sigma_r/\sigma_Y = 0.95$, (b) $\sigma_r/\sigma_Y = 0.75$, (c) $\sigma_r/\sigma_Y = 0.5$, and (d) $\sigma_r/\sigma_Y = 0.25$.

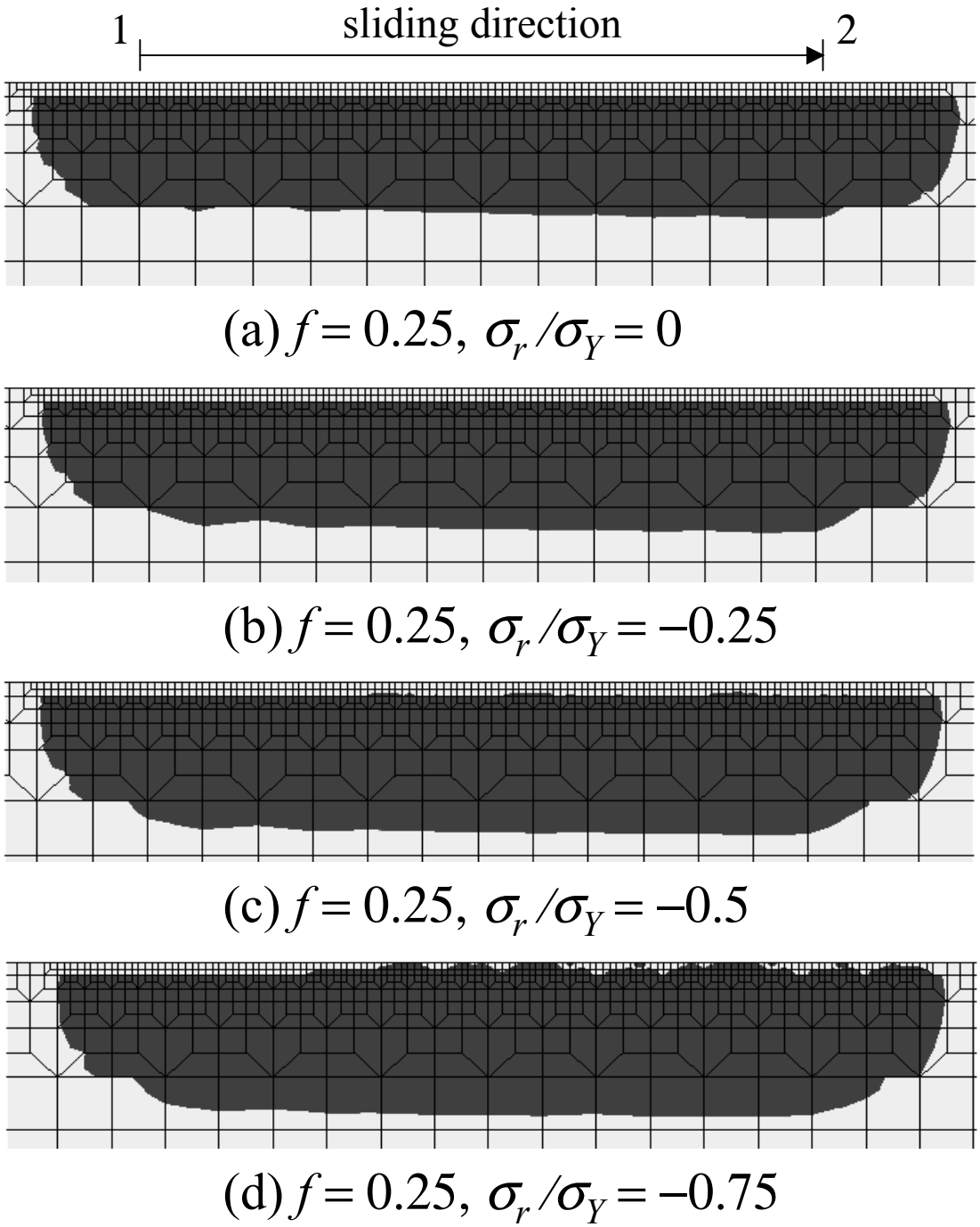

Figure 5.11 Comparison of plastic zones during sliding in a layered medium with f = 0.25: (a) $\sigma_r/\sigma_Y = 0$, (b) $\sigma_r/\sigma_Y = -0.25$, (c) $\sigma_r/\sigma_Y = -0.5$, and (d) $\sigma_r/\sigma_Y = -0.75$.

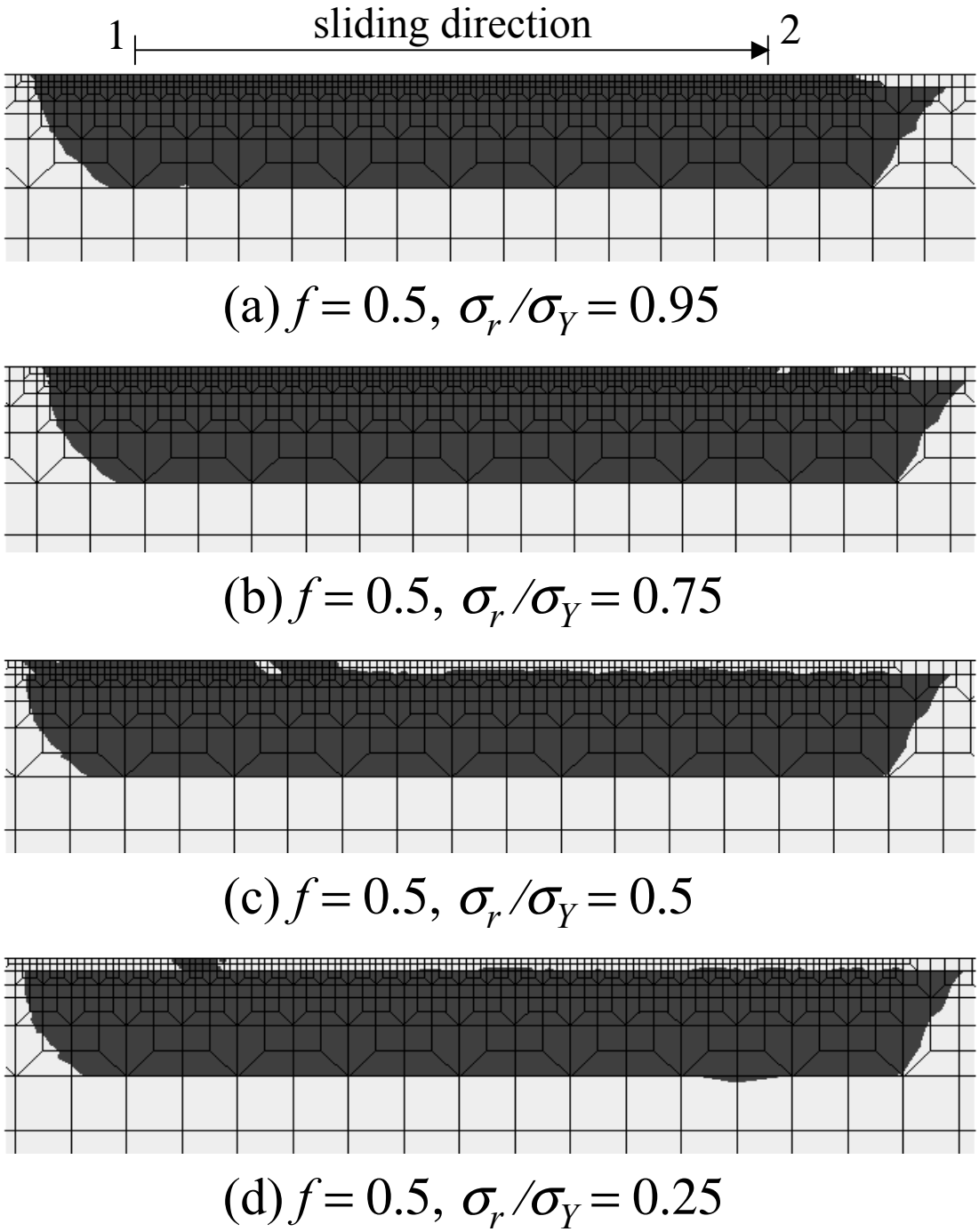

Figure 5.12 Comparison of plastic zones during sliding in a layered medium with f = 0.5: (a) $\sigma_r/\sigma_Y = 0.95$, (b) $\sigma_r/\sigma_Y = 0.75$, (c) $\sigma_r/\sigma_Y = 0.5$, and (d) $\sigma_r/\sigma_Y = 0.25$.

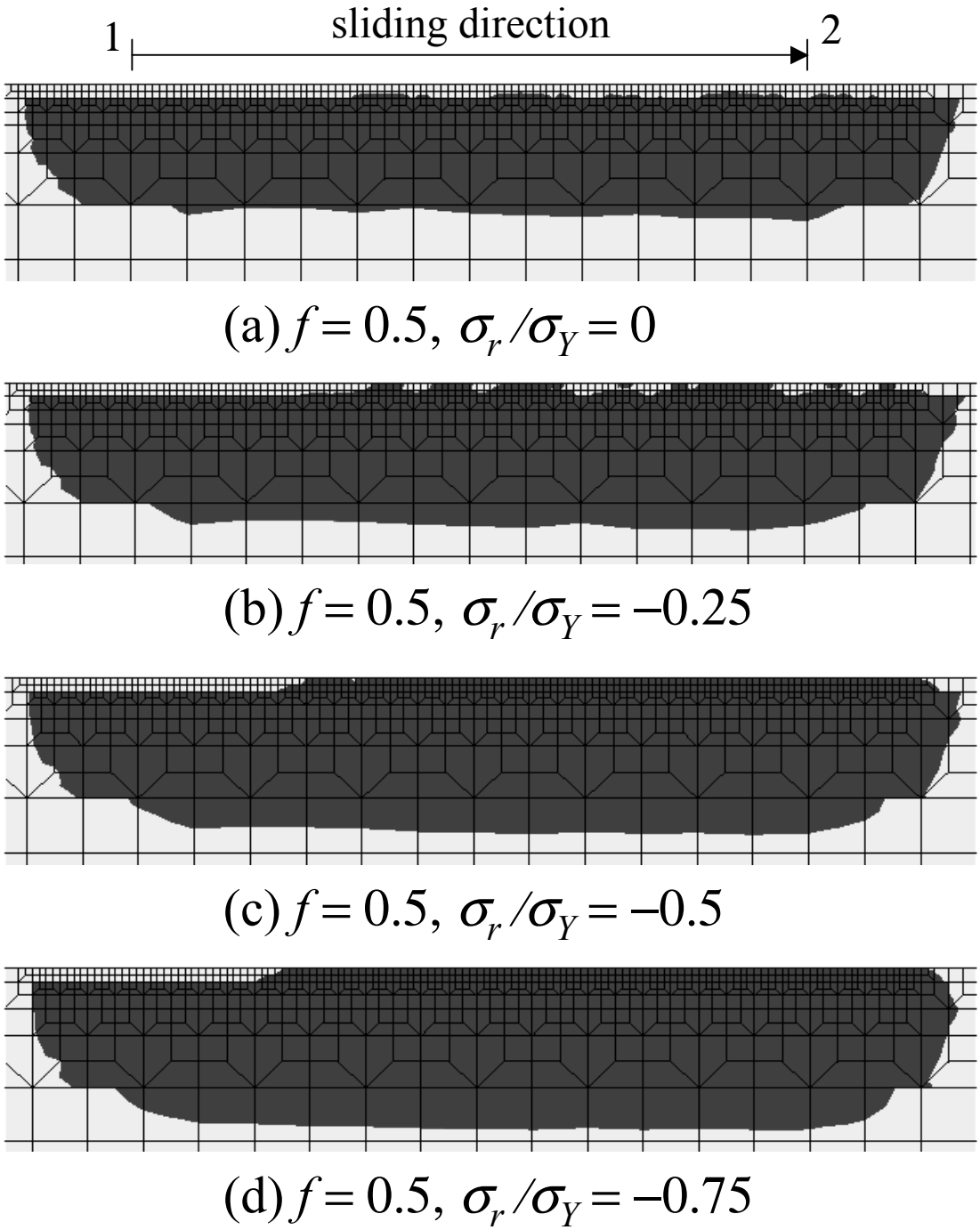

Figure 5.13 Comparison of plastic zones during sliding in a layered medium with f = 0.5: (a) $\sigma_r/\sigma_Y = 0$, (b) $\sigma_r/\sigma_Y = -0.25$, (c) $\sigma_r/\sigma_Y = -0.5$, and (d) $\sigma_r/\sigma_Y = -0.75$.

CHAPTER 6

HARDNESS ANALYSIS FOR ELASTIC-PLASTIC LAYERED MEDIA

6.1 Introduction

Hardness is a property characterizing the resistance of a material to indentation and wear. In traditional indentation tests, the applied normal load is of the order of hundreds to thousands of Newtons and the diameter of the indentation is of the order of micrometers to millimeters. Recently, hardness testing has evolved from microhardness to nanohardness measurement, where residual impressions have diameters of the order of micrometers or even nanometers, measured with high-power microscopes or atomic force microscopes. This is a result of the increasing use of layered media in various engineering applications where surface durability is of critical importance. Micro- and nano-indentation testing for layered media is an effective method of extracting information about the mechanical properties of thin surface layers. As a consequence, a large number of theoretical and experimental indentation studies have been performed to elucidate the effect of the surface layer on the mechanical response of layered media.

Pharr (1998) reviewed and discussed techniques for measuring mechanical properties by ultra-low load indentation techniques. Emphasis was given on the measurement of the elastic modulus and hardness using sharp indenters. One of the most widely used methods is that of Oliver and Pharr (1992), which expands on ideas developed by Loubet et al. (1984) and Doerner and Nix (1986). In this method, hardness and elastic modulus can be determined from load and displacement sensing in indentation

experiments. Lichinchi et al. (1998) used the finite element technique to study the stress-strain field in thin hard coatings subjected to nanoindentation loading. For titanium nitride coatings on high-speed steel, the substrate material was found to exhibit an effect on the hardness measurement for indentation depths greater than 15% of the film thickness. Pelletier et al. (2000) used the finite element method to analyze hardness measurement with a sharp pyramidal indenter, such as a Berkovich or Vickers indenter. The indenter tip radius was shown to exhibit a strong effect on the load-displacement response. A method was proposed to determine the tip radius of an equivalent conical indenter that was used in the finite element analysis as an approximation of the Berkovich indenter. Chen and Vlassak (2001) used the finite element method to investigate substrate and pileup effects on hardness and stiffness measurements of layered media. They defined a substrate effect factor and constructed a map that may be useful in the interpretation of indentation measurements when it is not possible to obtain sufficiently shallow indentations to avoid the influence of the substrate on the measurements. Martinez and Esteve (2001) studied nanoindentation of very hard and elastic thin layers, and reported that the hardness measured with a blunt indenter exhibited significant variation at small penetration depth.

The mechanical properties of a layered medium measured from indentation tests, such as hardness and elastic modulus, include the combined response of both the surface layer and the substrate materials. Bhattacharya and Nix (1988) studied the elastic and plastic deformation due to indentation of thin layers on relatively harder and softer substrates using the finite element method and derived semi-empirical relations for the hardness in terms of interference distance, layer thickness, and elastic-plastic material

properties of the layer and the substrate. King (1987) analyzed the normal contact problem of a layered isotropic elastic half-space using basis function and singular integral equation technique, and modified the relation for the effective elastic modulus of a layered medium, originally proposed by Doerner and Nix (1986).

The previous studies enable us the determination of the layer hardness and elastic modulus from the equivalent hardness and elastic modulus of the layered medium when the substrate properties are known, although in the model of Bhattacharya and Nix (1988) a relation between the hardness and yield strength of layer is required. Despite valuable insight into indentation mechanics and hardness measurement of layered media, there are several important issues requiring further analysis in order to determine the conditions under which the real hardness can be obtained. For example, if substrate properties are unknown, under what conditions can the layer hardness be approximated by the equivalent hardness? Another important issue is the minimum interference distance for a valid hardness measurement. Hence, the main objective of this study is to provide an analysis that gives answers to the previous issues. The critical interference distance to avoid the substrate effect was derived using the model of Bhattacharya and Nix (1988). A contact constitutive model, presented in a previous study (Komvopoulos and Ye, 2001) was used in conjunction with experimental results from other studies to derive the minimum interference distance for measuring the real material hardness. A general relation between hardness, yield strength, and elastic modulus, obtained from a finite element model, was used together with the model of Bhattacharya and Nix (1988) to obtain a scheme of extracting layer material properties. Example calculations are given to illustrate the appropriateness and predictability of the presented analytical scheme for

hardness measurement.

6.2 Finite Element Model

An axissymmetric finite element model was developed using the general-purpose finite element code ABAQUS to simulate indentation of a homogeneous or layered medium by a rigid sphere of radius *R*. Figure 6.1 shows the mesh of the finite element model, which consists of 218 eight-node isoparametric axissymmetric elements with a total of 677 nodes. The normalized dimensions of the mesh are $x/R = z/R = 8$. The nodes of the bottom boundary of the mesh were constrained in the *z*-direction and the nodes of the symmetry axis ($x = 0$) were constrained against the *x*-direction. A series of homogeneous half-spaces with different effective elastic modulus-to-yield strength ratio, E^*/s_Y ($E^* = \left[\left(1-n_1^2\right)/E_1 + \left(1-n_2^2\right)/E_2\right]^{-1}$, where n_1, n_2, and E_1, E_2 are the Poisson's ratios and elastic moduli of the half-space and rigid sphere) were analyzed. The materials were assumed to exhibit elastic-perfectly plastic behavior. The layer and substrate material properties used in the finite element model are listed in Table 6.1. Contact between the rigid sphere and the half-space medium was modeled with special contact elements, and the contact interface was assumed to be frictionless. Typically, an indentation simulation was completed in 5 time steps, each consisting of 100-500 increments. The computation time on an Intel Pentium III 550 workstation was between 2400 and 3600 CPU seconds.

6.3 Hardness Analysis

A theoretical treatment of the hardness of layered media is introduced in this section. The analysis yields the critical interference distance, above which the effect of

the substrate material on the equivalent hardness of the layered medium is significant, and the minimum interference distance, below which the occurrence of insufficient plastic deformation in the layer prevents the direct measurement of material hardness.

6.3.1 Critical Interference Distance to Avoid the Substrate Effect

If the mechanical properties of the substrate are unknown, the layer hardness can be approximated by the hardness measured from an indentation test performed on the layered medium, provided the indentation depth (interference distance) is sufficiently small to avoid the effect of the deformation of the substrate. The indentation hardness relations of Bhattacharya and Nix (1988) for relatively hard and soft surface layers can be used to determine the critical interference distance for the substrate effect to be insignificant.

For a layer harder than the substrate, the equivalent hardness, H_e, is given by (Bhattacharya and Nix, 1988)

$$\frac{H_e}{H_l} = \frac{H_s}{H_l} + \left(1 - \frac{H_s}{H_l}\right) \exp\left[- \frac{(H_l / s_l)}{(H_s / s_s)} \left(\frac{d}{h} \left(\frac{E_s}{E_l} \right)^{1/2} \right] \right], \tag{6.1}$$

where H is the hardness, h is the layer thickness, E is the elastic modulus, s is the yield strength, d is the interference distance between the indenter and the surface of the deformable medium, and subscripts l and s denote the layer and substrate material properties, respectively. Equation (6.1) can be rewritten as,

$$H_e = H_l e^{-\Delta} + H_s (1 - e^{-\Delta}), \tag{6.2}$$

where

$$\Delta \equiv \frac{(H_l / s_l)}{(H_s / s_s)}\left(\frac{d}{h}\right)\left(\frac{E_s}{E_l}\right)^{1/2}. \tag{6.3}$$

For the equivalent hardness to be close to the layer hardness, the contribution of the first term of Eq. (6.2) must be appreciably greater than that of the second term. Hence,

$$\frac{H_s(1-e^{-\Delta})}{H_l e^{-\Delta}} \le x\,, \tag{6.4}$$

where x is a tolerance parameter less than 1 (e.g., x = 10%) indicating that the contribution of the substrate material deformation to the hardness measurement is negligibly small. Then, the critical interference distance to avoid the substrate effect can be written as

$$\frac{d}{h} \le \ln(x\ \frac{H_l}{H_s}+1)\left(\frac{E_l}{E_s}\right)^{1/2}\frac{(H_s / s_s)}{(H_l / s_l)} \tag{6.5}$$

According to Eq. (6.5), the critical interference distance is a function of the tolerance parameter, elastic-plastic material properties of the layer and the substrate media, and layer thickness. Since for a layer harder than the substrate,

$$\left(\frac{E_l}{E_s}\right)^{1/2}\frac{(H_s / s_s)}{(H_l / s_l)} \ge 1, \tag{6.6}$$

Eq. (6.5) is satisfied if $d/h \le \ln(x+1)$. For $x << 1$, $\ln(x+1) \approx x$, and Eq. (6.5) can be approximated as

$$\frac{d}{h} \le x\,. \tag{6.7}$$

Thus, according to this empirical relation (Eq. (6.7)) the critical interference distance depends on the selected tolerance constant and hard layer thickness.

For a layer softer than the substrate, the effect of the substrate material

deformation on the equivalent hardness can be determined from relation (Bhattacharya and Nix, 1988),

$$\frac{H_e}{H_l} = \frac{H_s}{H_l} + \left(1 - \frac{H_s}{H_l}\right)\exp\left[-\frac{(s_l / E_l)}{(s_s / E_s)}\left(\frac{d}{h}\right)^2\right]. \tag{6.8}$$

Thus, the critical interference distance is given by

$$\left(\frac{d}{h}\right)^2 \le \ln(x\ \frac{H_l}{H_s} + 1)\frac{(s_s / E_s)}{(s_l / E_l)} \tag{6.9}$$

For a layer softer than the substrate,

$$\frac{(s_s / E_s)}{(s_l / E_l)} \le 1, \tag{6.10}$$

and $x\ \frac{H_l}{H_s} << 1$, Eq. (6.9) can be rewritten as,

$$\frac{d}{h} \le \sqrt{x\ \left(\frac{H_l}{H_s}\right)} \tag{6.11}$$

Although the critical interference distance can be determined from Eq. (6.5) (or Eq. (6.9)), the minimum interference distance to obtain the layer hardness cannot be obtained from this equation. According to Eq. (6.1) (or Eq. (6.8)), when the interference distance approaches zero, the measured hardness approaches the layer hardness. Since this is true only for a pyramidal indenter with infinitely sharp tip (i.e., zero tip radius of curvature), Eq. (6.1) (or Eq. (6.8)) cannot be used for shallow indentations, where the assumption of infinitely sharp indenter tip is not valid. Hence, it is necessary to obtain an analysis of material indentation by a finite tip radius indenter.

6.3.2 Relation Between Hardness, Yield Strength, and Elastic Modulus

For a spherical indenter and relatively small interference distance, the resulting

small plastic zone may yield a mean contact pressure that is not representative of the layer hardness. This is demonstrated by finite element simulation results shown in Figs. 6.2-6.4 for a homogeneous medium with effective elastic modulus-to-yield strength ratio E^*/s_Y = 10, 33, 100, and 200 indented by a rigid sphere. Figure 6.2 shows the dependence of the mean contact pressure, p_m, on representative strain $E^*d / s_Y r'$, where s_Y is the yield strength and r' is the radius of the truncated contact area. For all material properties, the mean contact pressure increases with representative strain to a peak value and then decreases, in agreement with the findings of Mesarovic and Fleck (1999), who observed a decrease of the mean contact pressure after rising to a value of about 3 times the yield strength for $E^*/s_Y \geq 250$. Figure 6.2 shows that the peak value of the normalized mean contact pressure depends on E^*/s_Y. This is consistent with the observation of Marsh (1964), who performed a series of indentation tests with various materials.

Figures 6.3 and 6.4 show the evolution of plasticity in the subsurface of homogeneous elastic-perfectly plastic half-space media with E^*/s_Y = 10 and 100, respectively. There are some similarities between the plastic zones in the two half-spaces. The general trend is for the plastic zone to expand radially as the indenter penetrates deeper in the medium (Figs. 6.3(a), 6.3(b), 6.4(a), and 6.4(b)). The plastic zone is initially contained in the subsurface surrounded by elastic material. Deeper indentations cause spreading of the plastic zone to the surface (Figs. 6.3(c), 6.3(d), 6.4(c), and 6.4(d)). However, a comparison of Figs. 6.3(a) and 6.4(d) shows that for a similar interference distance, the material with the higher E^*/s_Y value yields a much larger plastic zone. Moreover, the plastic zone of the material with lower E^*/s_Y occurs always below the

contact region, while the plastic zone of the material with higher E^*/s_Y spreads outside of the contact region after reaching the surface (Fig. 6.4(d)). The representative strain corresponding to the plastic zones shown in Figs. 6.3(d) and 6.4(d) is associated with the maximum value of the mean contact pressure. The representative strain and mean contact pressure for each plastic zone shown in Figs. 6.3 and 6.4 are given in Table 6.2. The maximum value of p_m/s_Y for $E^*/s_Y = 10$ and 100 is equal to 1.71 and 2.58, respectively.

Since the mean contact pressure depends on the representative strain (or interference distance), it is not straightforward to determine which is the interference distance (or strain) that yields the material hardness. A unique hardness value can be determined if the peak value of the mean contact pressure is set equal to the material hardness. This is consistent with the hardness definition of ductile materials, such as metals with typically $E^*/s_Y > 200$, for which full plasticity is more easily achieved, where the maximum contact pressure (hardness) is equal to $\sim 3s_Y$. However, as shown in Fig. 6.2, the peak contact pressure-to-yield strength ratio depends on the elastic-plastic material properties.

Before introducing the minimum interference distance for hardness measurement, it is instructive to examine the relation between hardness, yield strength, and elastic modulus of elastic-plastic homogeneous materials. Finite element results for the material hardness, H (assumed equal to the peak value of the mean contact pressure) are plotted in Fig. 6.5 and compared with experimental results obtained by Marsh (1964). The difference between simulation and experimental results is attributed to the Vickers indenter used in the experimental study and the constitutive relation adopted in the finite element simulations that may not be appropriate for the experimental materials. Since

shallow indentations are required for the determination of the minimum interference distance to obtain an accurate measurement of the layer hardness, a spherical indenter approximates more closely those used in this type of indentation tests. According to the best-fit line of the numerical data (with a correlation coefficient of 0.99), the material hardness is given by

$$\frac{H}{s_Y} = 0.90 + 0.37 \ln\left(\frac{E^*}{s_Y}\right), \qquad (10 \le E^*/s_Y \le 200). \tag{6.12}$$

As pointed out previously, for very thin layers, the interference distance (i.e., indention depth) must be sufficiently small in order to avoid the effect of the substrate material properties on the hardness measurement. However, if the indentation is too shallow, plastic deformation in the layer may be limited and the resulting mean contact pressure may not be representative of the layer hardness. Although mean contact pressure values can be obtained at any given indentation depth from the indentation load-depth curve, the mean contact pressure will not be equal to the layer hardness if the interference distance is not sufficient for the plastic zone in the layer to be fully developed. Thus, if the minimum interference distance is not reached, the layer hardness will be underestimated.

6.3.3 Minimum Interference Distance for Layer Hardness Measurement

A relation for the minimum interference distance required for the mean contact pressure to reach a value equal to the material hardness can be derived using Eq. (6.12) and the contact constitutive model of the normalized mean contact pressure and the representative strain for a spherical indenter in normal contact with a homogeneous medium derived in a previous study (Komvopoulos and Ye, 2001). According to this

analysis, elastic, elastic-plastic, and fully-plastic deformation regimes may occur. Clearly, interference distances corresponding to the elastic regime cannot be used to determine the hardness because deformation in this regime is purely elastic. Furthermore, in the fully-plastic regime the mean contact pressure is invariant. However, in view of the continuous transition from the elastic-plastic to the fully-plastic regime, the relation of the elastic-plastic regime given by

$$\frac{p_m}{s_Y} = 0.70 \ln\left(\frac{E^* d}{s_Y r'}\right) + 0.66, \qquad (1.78 \le E^* d / s_Y r' < 21), \qquad (6.13)$$

can be used to determine the interference distance for full plasticity. The representative strain, $E^* d / s_Y r'$, is also related to the normalized interference distance, d/R. By equating the mean contact pressure with the material hardness, the corresponding interference distance can be determined from the contact constitutive model (Eq. (6.13)). The number of independent variables can be reduced by using the hardness relation obtained from finite element simulations (Eq. (6.12)).

Because only shallow indentations are considered to obtain the minimum interference distance, the analysis can be simplified to that of a homogeneous half-space with layer material properties. Using Eqs. (6.12) and (6.13), the minimum interference distance is obtained as

$$\frac{d}{r'} = 1.41\left(\frac{s_Y}{E^*}\right)^{0.47} \qquad (6.14)$$

Hence, by introducing the indenter radius of curvature, the following relation must be satisfied in order for the real material hardness to be obtained,

$$\frac{d}{R} = \frac{2}{1+(r'/d)^2} \geq \frac{2}{1+0.50(E^*/s_Y)^{0.94}} \tag{6.15}$$

Equation (6.15) gives the minimum interference distance as a function of the indenter radius of curvature and effective elastic modulus-to-yield strength ratio . For relatively small values of E^*/s_Y (e.g., E^*/s_Y = 10), a deeper interference distance is needed for the mean contact pressure to reach a value equal to the material hardness (Fig. 6.2-6.4, Table 6.2). This is due to the increase of the material resistance to plastic flow with a decreasing E^*/s_Y. Equation (6.15) can be used to estimate the minimum interference distance if the elastic modulus and yield strength of the layer are known, and reflects the hardness dependence on geometry factors and material properties.

If the layer material properties are unknown, various indentation depths must be used to verify whether the minimum interference distance was reached. If the layer is too thin, there may be no indenter with sufficiently sharp tip to ensure that the minimum interference distance required to directly measure the layer hardness is less than the critical interference distance to avoid the substrate effect. In this case, the hardness of a very thin layer can be determined from the measured equivalent hardness using Eqs. (6.1) (or Eq. (6.8)) and (6.12).

From the variation of the hardness of the layered medium with the interference distance, it is possible to determine whether Eq. (6.1) or Eq. (6.8) describes the hardness of the layered medium. The compliance determined from the unloading portion of the indentation curve can be used to determine the value of $E_l/(1-\nu_l^2)$, because the effective elastic modulus of the layered medium is related to the initial unloading stiffness through $S \equiv dL/dd = 2rE_e^*$ (Sneddon, 1965), where the effective elastic modulus of a layered

medium, E_e^*, is given by (King, 1987)

$$E_e^* = \left[\left(1 - e^{-a\,h/r\sqrt{p}}\right) \frac{1-n_l^2}{E_l} + e^{-a\,h/r\sqrt{p}} \frac{1-n_s^2}{E_s} + \frac{1-n_i^2}{E_i} \right]^{-1}, \tag{6.16}$$

where a is a geometrical factor depending on the indenter shape, r is the radius of the projected contact area, and subscript i denotes the indenter material properties. However, the hardness of the layer cannot be calculated solely from either Eq. (6.1) or Eq. (6.8), because the yield strength of the layer is unknown, direct inversion of Eq. (6.1) or Eq. (6.8) is not possible. Therefore, Eq. (6.12) must be solved simultaneously with Eq. (6.1) or Eq. (6.8). According to Eq. (6.15), the interference distance must be greater than a minimum value that depends on the radius of curvature of the indenter tip and the layer material properties. Therefore, an arbitrary interference distance does not guarantee a valid hardness measurement. Instead, indentations for a series of interference distances must be performed in order to determine whether Eq. (6.1) or Eq. (6.8) should be used and to verify whether the real hardness of the layer was measured. Therefore, at each interference distance, Eqs. (6.1) (or Eq. (6.8)) and (6.12) are solved together, and the calculated hardness and yield strength of the layer, H_l^c and s_l^c, respectively, are obtained as functions of interference distance. (The term “calculated” is used to denote that the data do not necessarily correspond to the real layer material properties.) The calculated hardness (or mean contact pressure) increases with interference distance, reaching a peak value corresponding to the real material hardness, as shown in Fig. 6.2. If the calculated hardness versus interference distance curve increases continuously without reaching a maximum, then none of the data yields the material hardness. This would be the case of too shallow indentations, or too large radius of curvature of the indenter tip, to induce

sufficient plasticity.

6.4 Numerical Simulation Results

Numerical results are presented in this section to demonstrate the appropriateness of the developed analysis for hardness measurement of layered media and to validate the hardness measurement scheme presented. For relatively hard layer of known thickness and unknown substrate material properties, the equivalent hardness of the layered medium can be assumed to be equal to the layer hardness, provided the interference distance is such that to avoid the substrate effect (Eq. (6.7)). As an example, consider a rigid spherical indenter and E_l = 168 GPa, s_l = 13 GPa, E_s = 130 GPa, s_s = 2.67 GPa, and $n_l = n_s = 0.3$. Using Eq. (6.12), the layer hardness and the substrate hardness are found to be H_l = 24.5 GPa and H_s = 6.34 GPa, respectively. If the tolerance constant x is set equal to 10% and d/h is chosen to be 0.1, the equivalent hardness obtained from Eq. (6.1) is H_e = 23.2 GPa, which differs from the layer hardness by only 5%. Then, the minimum interference distance can be used either to verify whether the hardness of the layer was reached or to select the right indenter tip. Assuming a hard layer thickness equal to 100 nm, the interference distance for $x = 0.1$ is estimated to be less than 10 nm (Eq. (6.7)). To satisfy Eq. (6.15), $d/R \geq 0.28$; therefore, the indenter tip radius of curvature must be less than 35 nm.

A finite element simulation of a layered medium with a hard layer indented by a rigid sphere was performed to illustrate the hardness evaluation scheme presented in the previous section. The layer thickness and material properties used in this simulation were identical to those given in Table 6.1. It is assumed that these equivalent hardness data

were obtained from an indentation test performed on a layer of given thickness and unknown material properties deposited on a substrate with known material properties. Figure 6.6 shows the indentation load, L, versus interference distance, d, of the layered medium obtained from the finite element analysis. The value of $E_l/(1-n_l^2)$, determined from the elastic stiffness (S = 2.94 μN/nm) obtained from the slope of the unloading curve at maximum load and Eq. (6.16), was found to be equal to 179 GPa, which differs from the input value in the finite element model by only 3%. Figure 6.7(a) shows finite element results for the equivalent hardness (or mean contact pressure) versus interference distance. Since the ratio between the equivalent hardness of the layered medium and the substrate hardness is greater than 1, it is concluded that the layer is harder than the substrate. In Eqs. (6.1) and (6.12) (using layer material properties) the values of H_e, $E_l/(1-n_l^2)$, $E_s/(1-n_s^2)$, s_s, d, and h are known. The value of H_s can be obtained from Eq. (6.12) using substrate material properties. Then, Eqs. (6.1) and (6.12) are solved simultaneously to obtain H_l^c and s_l^c at different interference distances using an iteration procedure. Results for the ratio of calculated and real layer properties are plotted in Fig. 6.7(b) in terms of interference distance. Both the calculated hardness and yield strength of the layer increase with interference distance, reaching a peak value at d/R = 0.4. According to the scheme proposed earlier, the calculated hardness and yield strength at d/R = 0.4 are the real material properties of the layer. Compared to the layer yield strength inputted in the finite element model and the hardness calculated from Eq. (6.12) using the material properties inputted in the finite element model, the error is less than 5%. For the layer material properties given in Table 6.1, Eq. (6.15) yields that the interference distance

must be greater than $0.37R$ in order to obtain the real layer hardness, which is in fair agreement with the value predicted by the finite element simulation. Therefore, even for large plastic deformation and significant substrate effect, Eq. (6.15) can provide a fairly good estimate of the minimum interference distance required to obtain the real material hardness. Hence, this numerical experiment demonstrates the correctness of the proposed scheme.

The evolution of plasticity in the layer and substrate media of the previous simulation is shown in Fig. 6.8. At small interference distances (Figs. 6.8(a) and 6.8(b)) the plastic zone is confined in the layer and is similar to that obtained for a homogeneous medium (Figs. 6.3(a) and 6.3(b)). As the interference distance increases, plastic deformation initiates at the layer/substrate interface (Fig. 6.8(c)). Further penetration causes the plastic zone in the layer to grow toward the surface and the plastic zone in the substrate to expand downward and parallel to the interface (Figs. 6.8(d) and 6.8(e)). Eventually, the two plastic zones merge together (Fig. 6.8(f)). As can be seen in Fig. 6.8(f), the plastic zone in the substrate is comparable to that in the layer when $d/R = 0.4$, indicating that the substrate effect is significant.

6.5 Conclusions

A general hardness analysis for layered and homogeneous media was introduced that builds upon finite element simulation results and hardness relations derived in previous studies. In view of the presented results and discussion, the following main conclusion can be drawn.

(1) For the hardness of the layered medium to be close to that of the layer material, the interference distance must be less than a critical value that depends on the layer

thickness and elastic-plastic properties of the layer and substrate materials in order to avoid the effects of the substrate deformation.

(2) For sufficient plasticity to occur in the layer such that the mean contact pressure to reach a value close to the real hardness of a material, the interference distance must be larger than a minimum value, which is a function of the radius of the indenter tip, effective elastic modulus, and yield strength of the material.

(3) The dependence of hardness on yield strength and elastic modulus was elucidated in light of finite element simulation results. A numerical scheme to determine the layer hardness from a series of indentation data was proposed and its effectiveness was validated by numerical results for a layered medium with a hard surface layer.

Table 6.1. Thickness and properties of layer and substrate media of the finite element model

Medium	Layer	Substrate
Thickness, h/R	1	7
Elastic modulus, E (GPa)	168	160
Poisson ratio, n	0.3	0.3
Yield strength, s_l or s_s (GPa)	18.46	7

Table 6.2. Interference distance, equivalent strain, and mean contact pressure in Figs. 6.3 and 6.4.

E^*/s_Y	d/R	$E^* d/s_Y r'$	p_m/s_Y
10	0.072	1.93	1.12
	0.100	2.29	1.24
	0.200	3.33	1.50
	0.400	5.00	1.71
100	0.005	5.01	1.79
	0.007	5.93	1.91
	0.040	14.34	2.52
	0.059	17.48	2.58

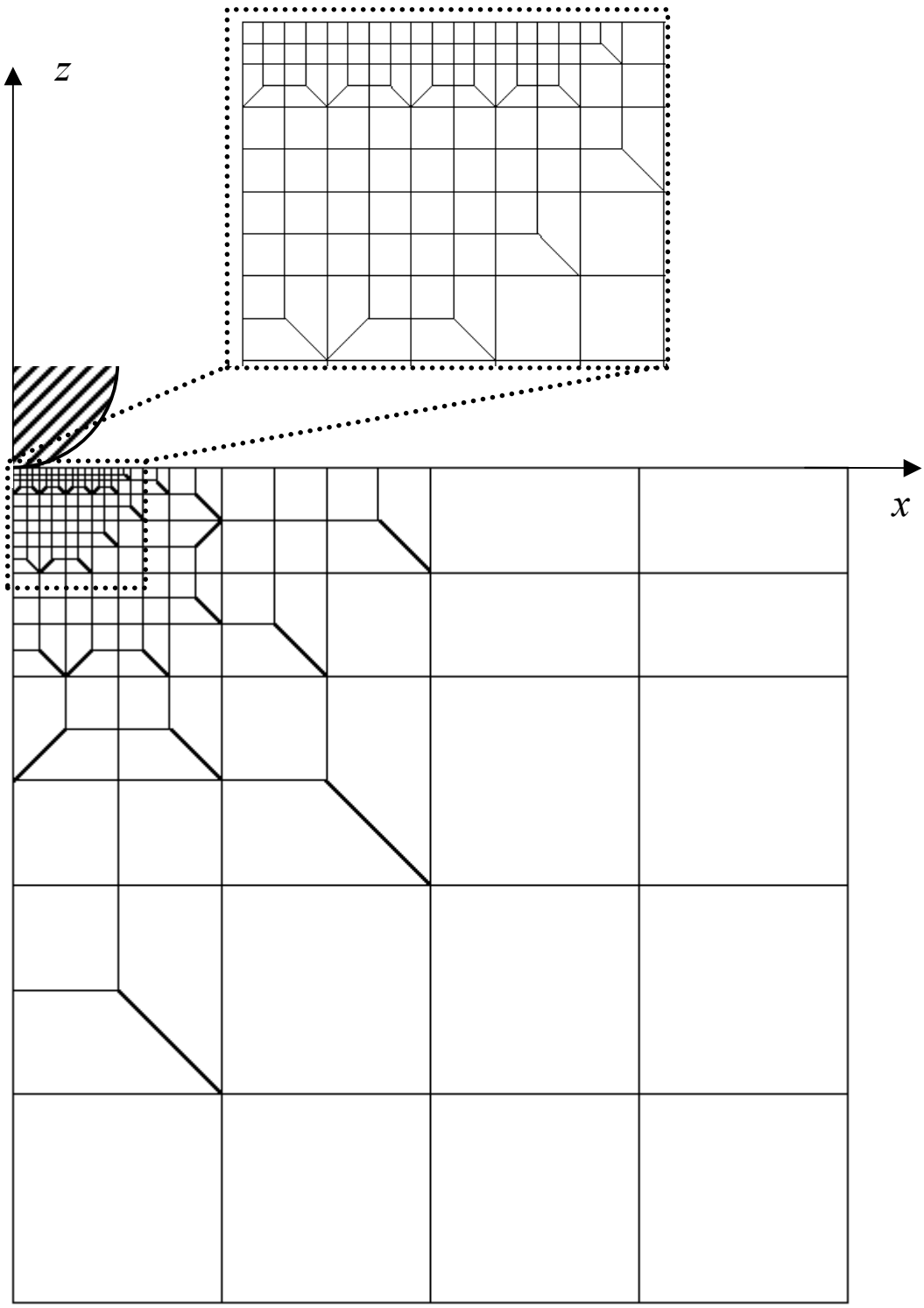

Figure 6.1 Axissymmetric finite element mesh used in indentation simulations of both homogeneous and layered media. (The inset of the figure shows the refinement of the mesh of the contact region.)

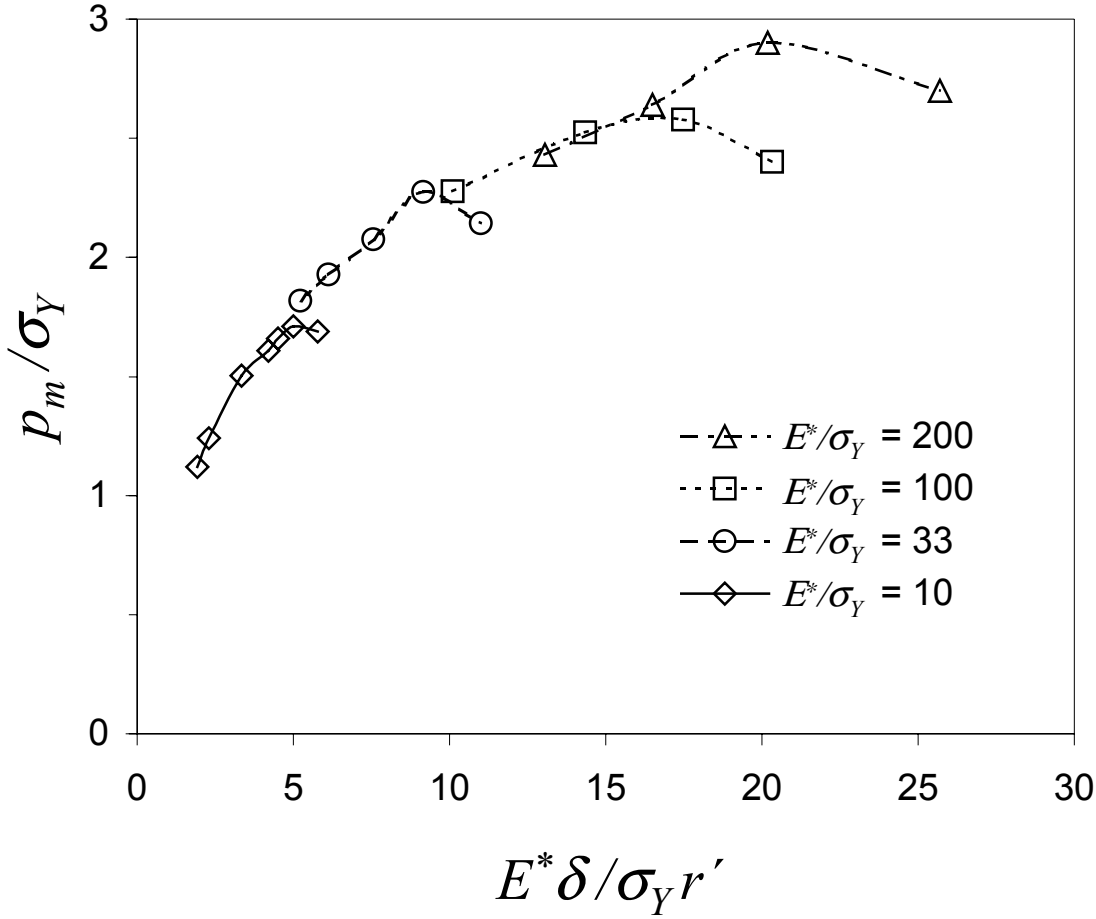

Figure 6.2 Normalized mean contact pressure versus representative strain for different material properties of homogeneous media.

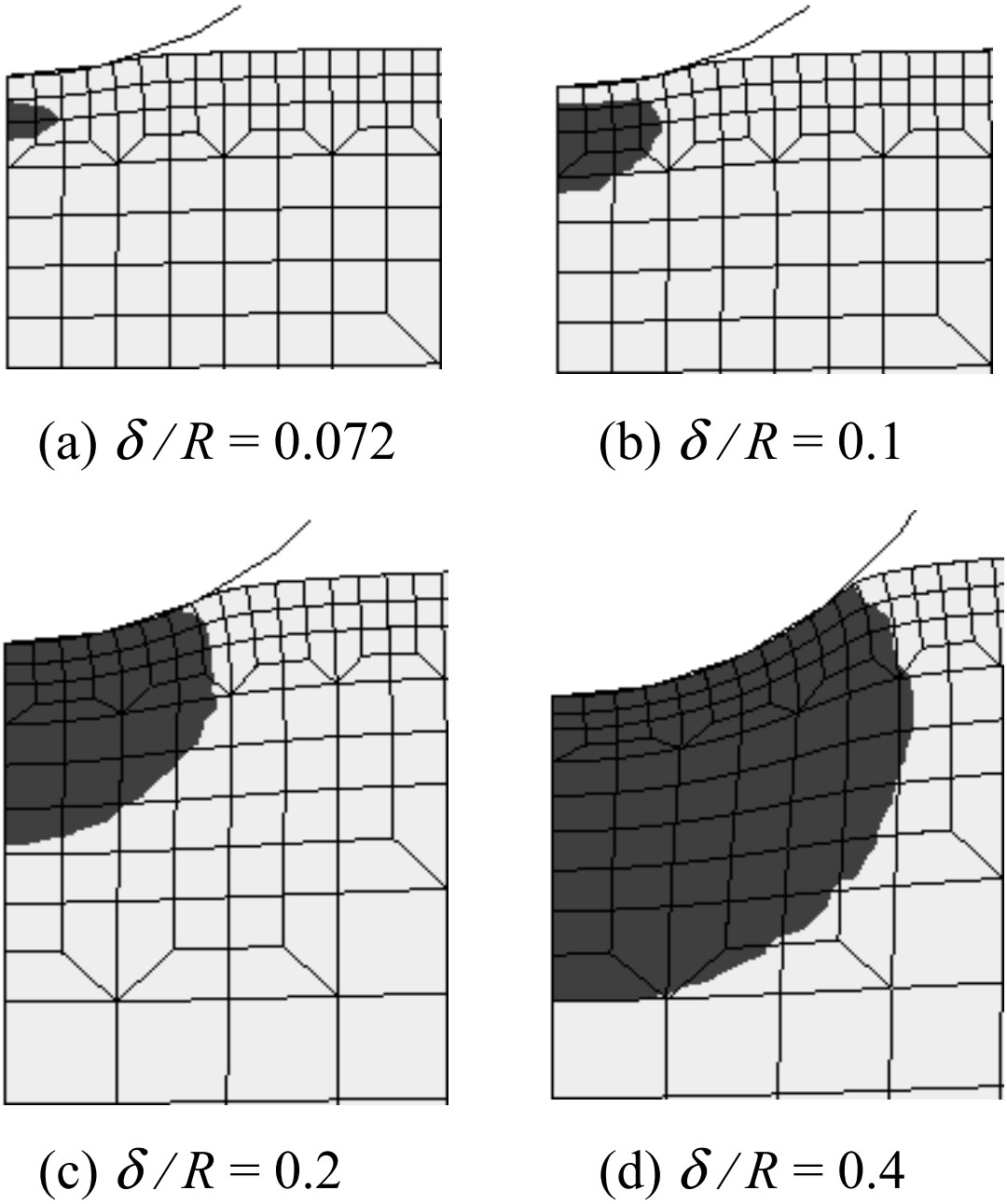

Figure 6.3 Plastic zone evolution in a homogeneous material with $E^*/\sigma_Y = 10$ indented by a rigid sphere: (a) $\delta/R = 0.072$, (b) $\delta/R = 0.1$, (c) $\delta/R = 0.2$, and (d) $\delta/R = 0.4$.

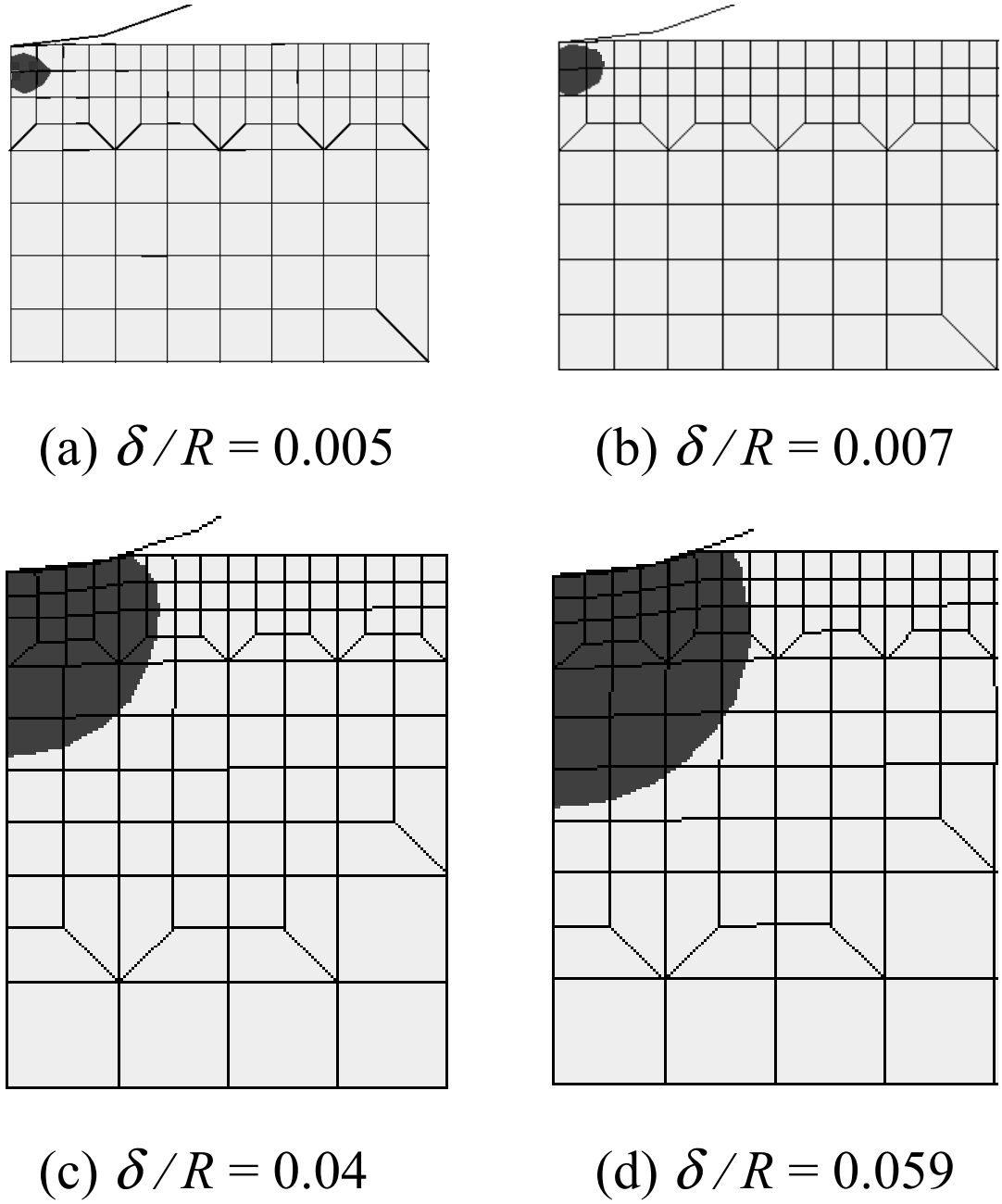

Figure 6.4 Plastic zone evolution in a homogeneous material with E^*/σ_Y = 100 indented by a rigid sphere: (a) δ/R = 0.005, (b) δ/R = 0.02, (c) δ/R = 0.04, and (d) δ/R = 0.059.

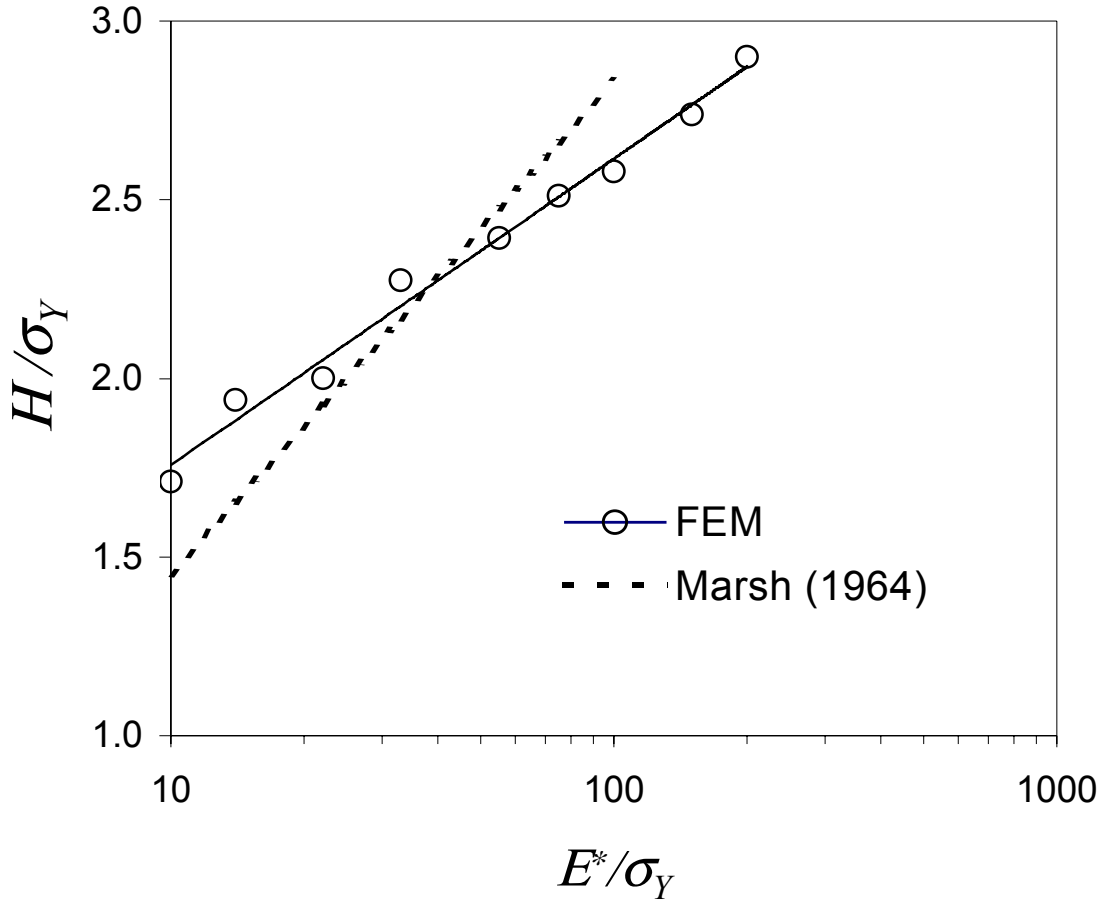

Figure 6.5 Comparison between finite element results and experimental data for the normalized hardness versus effective elastic modulus-to-yield strength ratio.

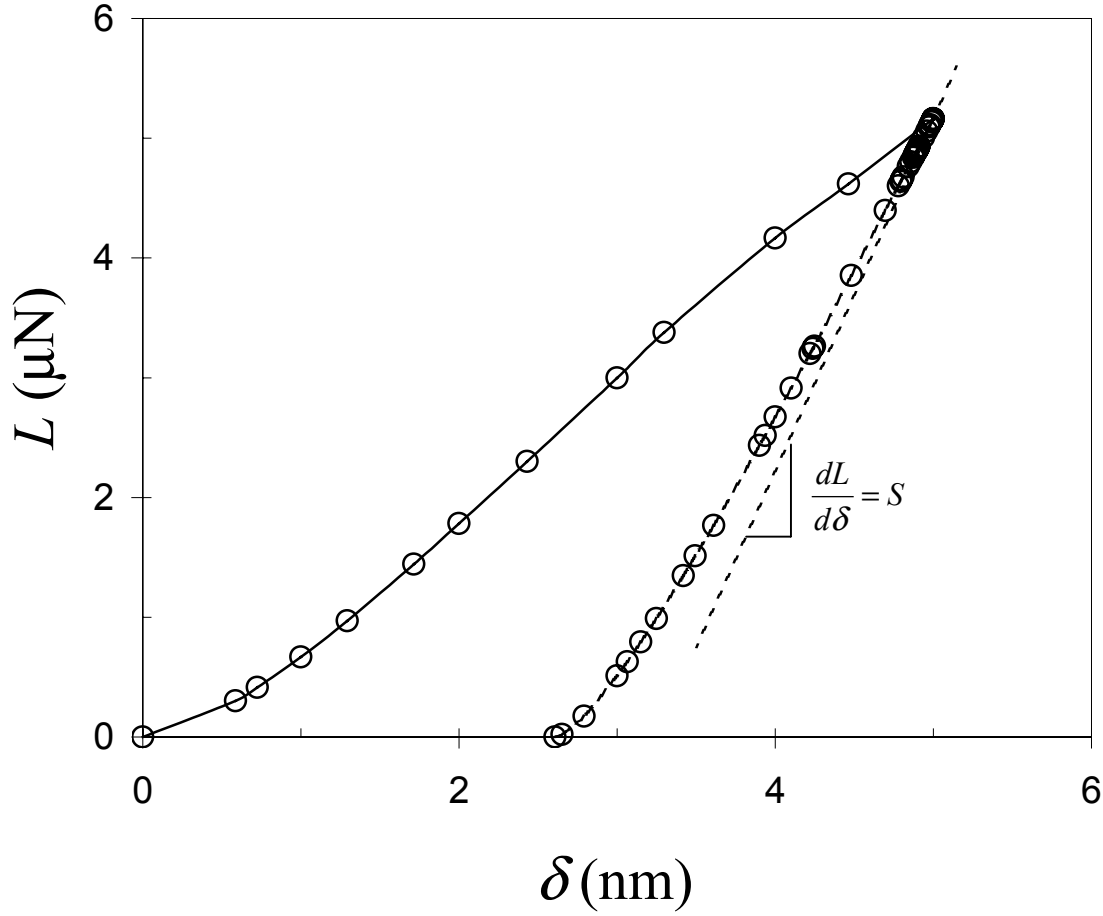

Figure 6.6 Indentation load versus interference distance for a layered medium with $E_l^*/\sigma_l = 10$.

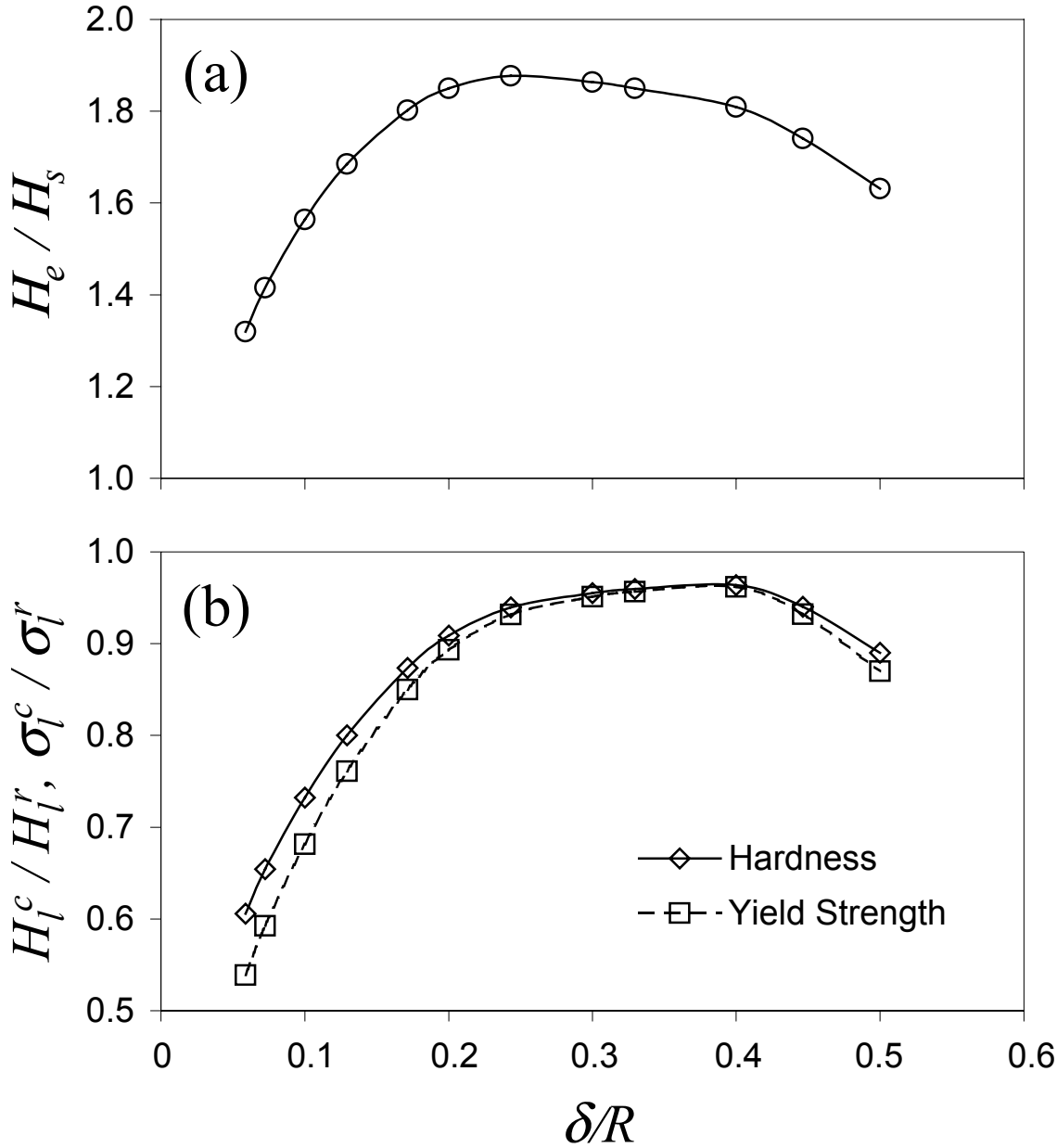

Figure 6.7 (a) Equivalent hardness of a layered medium normalized by the substrate hardness versus normalized interference distance, and (b) calculated layer hardness and yield strength normalized by corresponding real values versus normalized interference distance.

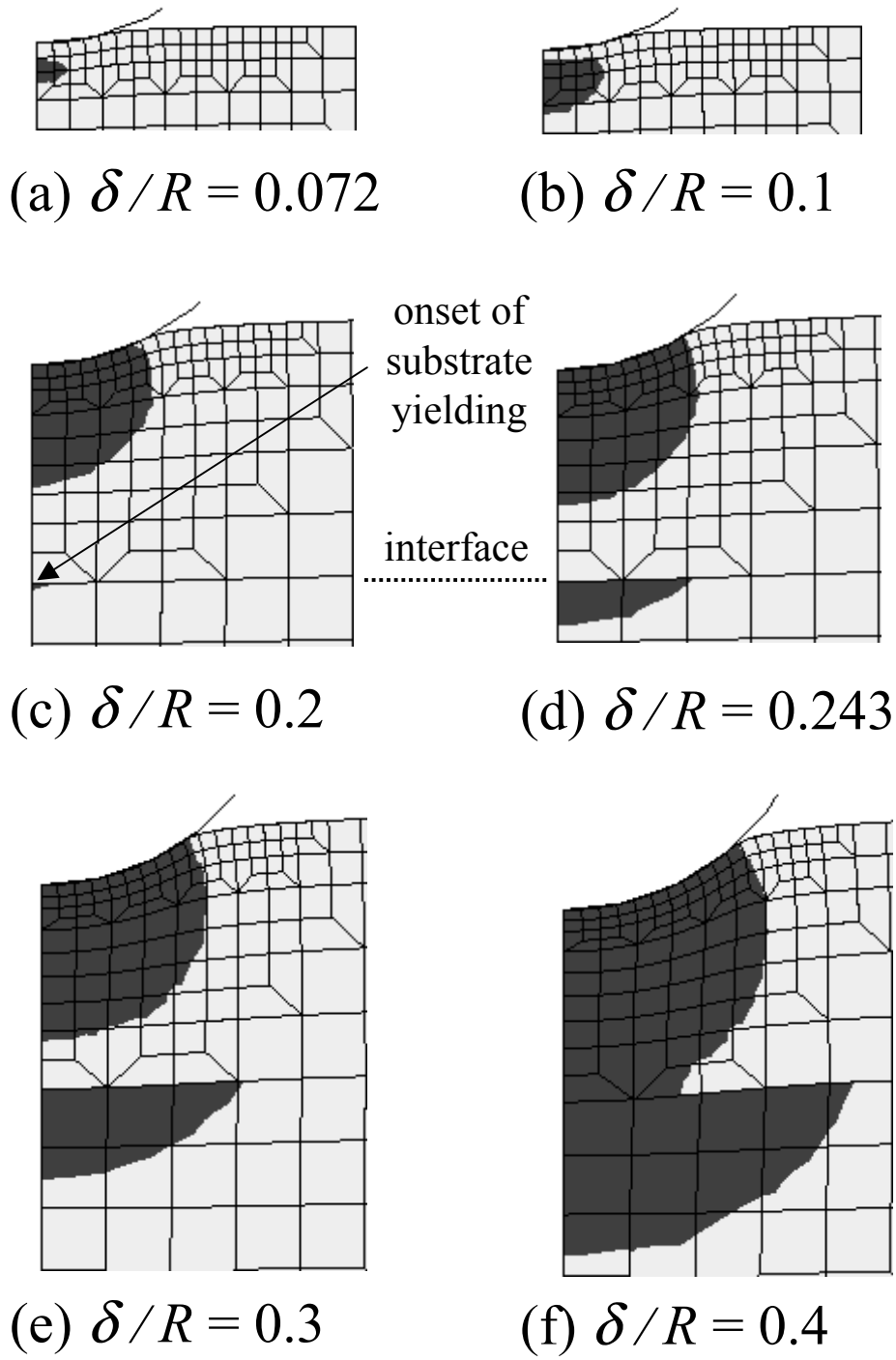

Figure 6.8 Plastic zone evolution in a layered medium with $E_l^*/\sigma_l = 10$: (a) $\delta/R = 0.072$, (b) $\delta/R = 0.1$, (c) $\delta/R = 0.2$, (d) $\delta/R = 0.243$, (e) $\delta/R = 0.3$, and (f) $\delta/R = 0.4$.

CHAPTER 7

CONCLUSIONS

Contact mechanics analyses for elastic-plastic layered media subjected to single- and multi-asperity contacts (fractal surfaces) have been performed in this dissertation. Based on the obtained results and discussions in Chapters 2-6, the following main conclusions can be drawn.

To understand the effect of surface topography on elastic-plastic contact (e.g., contact load and real contact area) of layered media, a three-dimensional contact model was developed to account for elastic, elastic-plastic, and fully plastic deformation at asperity microcontacts. The model uses constitutive relations for the mean contact pressure and real contact area versus a representative strain derived from a finite element model of a rigid sphere indenting an elastic-plastic half-space. The representative strain in the constitutive model is a local deformation parameter that depends on the mechanical properties of the contacting surfaces, local surface interference distance, and contact radius of truncated asperities. Numerical results were obtained for the head-disk contact interface characterized by fractal geometry. For a given surface topography, both the contact load and the real contact area were shown to increase monotonically with increasing maximum surface interference distance. The contact load was found to decrease with decreasing fractal dimension D and/or increasing fractal roughness G. This was attributed to the effect of fractal parameters on the load bearing surface area. It was demonstrated that the effect of the mechanical properties of the magnetic medium on the contact load and deformation behavior at the real contact area becomes more pronounced

with decreasing overcoat thickness.

Another objective of this work was to incorporate the actual surface topographies (characterized by fractal geometry) and elastic-plastic material properties of the different layers of a thin-film disk in a finite element model in order to investigate the subsurface stress/strain fields of normal contact at the head-disk interface. For the range of maximum surface interference examined, contact was found to consist mostly of isolated asperity microcontacts at a few regions of the contact interface, depending on characteristic surface topography parameters, such as fractal dimension D and fractal roughness G. Due to the dominant effect of high-frequency components in the surface profile on microcontact formation, the evolution of deformation in these regions exhibited similarities. This indicated that the analysis can be carried out over a contact segment of the surface profile containing all the contributing small wavelengths. The stress and strain fields were shown to be confined within the carbon overcoat and the magnetic layer. The asperity shape (or effective radius of curvature) controls plastic deformation in the overcoat and magnetic layer. For the ranges of overcoat thickness and material properties examined, the maximum tensile stress in the overcoat and the magnetic layer occurred at the surface and the interface, respectively. The results showed that plastic deformation and the likelihood of cracking due to a high tensile stress at the overcoat surface and the interface with the magnetic layer were both enhanced by decreasing overcoat thickness. Although stiffer and harder overcoats exhibit higher resistance to plastic deformation and surface cracking, they promote plasticity in the magnetic layer, at the interface with the overcoat. A compressive residual stress in the overcoat was found to exhibit a profound effect on the plastic flow resistance of the

overcoat; however, its effect on the deformation in the magnetic layer was secondary. The results revealed that an optimum compressive residual stress exists, which depends on the overcoat yield strength.

To investigate the simultaneous effects of elastic-plastic deformation and conduction of frictional heat in contacting solids, and the effects of material properties and thickness of the surface layer on the evolution of temperature, stress, and strain fields in elastic-plastic layered media, a three-dimensional thermomechanical finite element analysis for an elastic sphere sliding on an elastic-plastic layered medium was performed. Steady-state temperature distributions were reached at the layer surface and layer/substrate interface at sliding distances of 4-6 times the contact radius. For the range of parameters examined, the layer thickness exhibited a more pronounced effect on the temperature rise at the layer surface and layer/substrate interface than the layer thermal conductivity. It was confirmed that frictional heating coupled with shear surface traction in sliding contact may intensify the stress field in layered media significantly. The likelihood for yielding and cracking increased with decreasing layer thickness. The location of the maximum von Mises equivalent stress, maximum tensile stress, and maximum equivalent plastic strain was shown to depend on the layer thickness and the frictional heat conducted through the layer, which is controlled by the thermal conductivity of the layer material, coefficient of friction, contact interface compliance, and applied normal load.

In order to analyze the effect of the residual stress in the surface layer (overcoat) and coefficient of friction on the evolution of stress and strain fields, a three-dimensional finite element analysis for normal and sliding contact of elastic-plastic layered media was

performed. The maximum first principal stress in the surface layer increased (decreased) with tensile (compressive) residual stress. During indentation, the location of the maximum first principal stress in the layer shifted from the bulk to the surface of the layer as the residual stress changed from compressive to tensile. The magnitude of optimal residual stress in sliding contacts depends on the coefficient of friction. Higher coefficient of friction promotes plasticity and intensifies the maximum first principal stress in both the layer and substrate media. For sliding, the location of maximum plastic strain in the substrate is always at the interface between the layer and substrate. The location of maximum plastic strain in the layer shifted from the layer/substrate interface to the layer surface when the residual stress changed from compressive to tensile. During unloading, unmatched elastic relaxation between plastic and elastic regions in the substrate generates a higher maximum first principal stress than that during sliding. In the case of sliding and unloading, the maximum first principal stress in the substrate was found to occur always at the layer/substrate interface. The optimal residual stress was shown to depend on the type of contact (normal or sliding), coefficient of friction, and deformation mode of the overcoat, i.e., plastic deformation or cracking.

To ensure valid hardness measurement of layered media, an analytical treatment of indentation was introduced that uses finite element results. It was demonstrated that in order to avoid substrate effects and for the layer/substrate composite hardness to be close to that of the layer material, the interference distance must be less than an critical value that depends on the layer thickness and mechanical properties of the layer and substrate materials. In addition, the interference distance must be larger than a minimum value such that sufficient plasticity is induced in order for the mean contact pressure to reach

the actual hardness of a material. This minimum value is a function of the radius of indenter tip and the effective elastic modulus and yield strength of the material. The dependence of hardness on yield strength and elastic modulus was determined by finite element simulations. A new scheme to determine layer hardness from a series of indentation data was proposed and its effectiveness was validated by numerical simulation results.

In summary, the present work produced results that enhance the understanding of surface topography, thermo-mechanical traction, layer residual stress, and thickness and mechanical properties of surface layer on the contact deformation behavior of elastic-plastic layered media. The obtained results provide insight into the possible deformation mode of layered media and guidance to the design of more durable thin-film media for microelectromechanical systems and the head-disk interface of computer hard disks.

REFERENCES

Abermann, R., and Koch, R., 1980, "In situ determination of the structure of thin metal films by internal stress measurements: structure dependence of silver and copper films on oxygen pressure during deposition," *Thin Solid Films*, **66**, pp. 217- 232.

Alblas, J. B., and Kuipers, M., 1970, "On the Two Dimensional Problem of a Cylindrical Stamp Pressed into a Thin Elastic Layer," *Acta Mechanica*, **9**, pp. 292-311.

Aleksandrov, V. M., Babeshko, V. A., and Kucherov, 1966, "Contact Problems for an Elastic Layer of Slight Thickness," *Journal of Applied Mathematics and Mechanics*, **39**, pp. 124-142.

Anguiano, E., Pancorbo, M., and Aguilar, M., 1994, *Fractals in the Natural and Applied Sciences*, Novak, M. M., ed., Elsevier Science, New York, pp. 37-46.

Ausloos, M., and Berman, D. H., 1985, "A Multivariable Weierstrass-Mandelbrot Function," *Proceedings of the Royal Society (London)*, Series A, **400**, pp. 331-350.

Bai, M., Kato, K., Umehara, N., and Miyake, Y., 2000, "Nanoindentation and FEM Study of the Effect of INternal Stress on Micor/Nano Mechanical Property of Thin CN_x Films," *Thin Solid Films*, **377-378**, pp. 138-147.

Berry, M. V., and Lewis, Z. V., 1980, "On the Weierstrass-Mandelbrot Fractal Function," *Proceedings of Royal Society (London)*, Series A, **370**, pp. 459-484.

Bhattacharya, A. K., and Nix, W. D., 1988, "Analysis of Elastic and Plastic Deformation Associated with Indentation Testing of Thin Films on Substrates," *International Journal of Solids and Structures*, **24**, pp. 1287-1298.

Blackmore, D., and Zhou J. G., 1998a, "Fractal Analysis of Height Distributions of Anisotropic Rough Surfaces," *Fractals*, **6**, pp. 43-58.

Blackmore, D., and Zhou G., 1998b, "A New Fractal Model for Anisotropic Surfaces," *International Journal of Machine Tools & Manufacturing*, **38**, pp. 551-557.

Blok, H., 1937, "Theoretical Study of Temperature Rise at Surfaces of Actual Contact Under Oiliness Lubricating Conditions," *Proceedings General Discussion on Lubrication*, Institute of Mechanical Engineers (London), **2,** pp. 222-235.

Borodich, F. M., and Onishchenko, D. A., 1999, "Similarity and Fractality in the Modeling of Roughness by a Multilevel Profile with Hierarchical Structure," *International Journal of Solids and Structures*, **36**, pp. 2585-2612.

Chen, X., and Vlassak, J. J., 2001, "Numerical Study on the Measurement of Thin Film Mechanical Properties by Means of Nanoindentation," *Journal of Materials Research*, **16**, pp. 2974-2982.

Cho, S.-S., and Komvopoulos, K., 1997, "Thermoelastic Finite Element Analysis of Subsurface Cracking Due to Sliding Surface Traction," ASME *Journal of Engineering Materials and Technology*, **119**, pp. 71-78.

Ciavarella, M., Demelio, G., Barber, J. R., and Jang, Y. H., 2000, "Linear Elastic Contact of the Weierstrass Profile," *Proceedings of the Royal Society* (London), Series A, **456**, pp. 387-405.

Day, A. J., and Newcomb, T. P., 1984, "The Dissipation of Frictional Energy from the Interface of an Annular Disc Brake," *Proceedings Institution of Mechanical Engineers*, **198D**, pp. 201-209.

Doerner, M. F., and Nix, W. D., 1986, "A Method for Interpreting the Data From Depth-Sensing Indention Instruments," *Journal of Materials Research*, **4**, pp. 601-609.

Greenwood, J. A., and Williamson, J. B. P., 1966, "Contact of Nominally Flat Surfaces," *Proceedings of the Royal Society* (London), Series A, **295**, pp. 300-319.

Gupta, V., Bastias, P., Hahn, G. T., and Rubin, C. A., 1993, "Elastoplastic Finite-Element Analysis of 2-D Rolling-Plus-Sliding Contact With Temperature-Dependent Bearing Steel Material Properties," *Wear*, **169**, pp. 251-256.

Hamilton, G. M., 1983, "Explicit Equations for the Stresses Beneath a Sliding Spherical Contact," *Proceedings Institution of Mechanical Engineers Part C – Journal of Mechanical Engineering Science*, **197**, pp. 53-59.

Hamilton, G. M., and Goodman, L. E., 1966, "The Stress Field Created by a Circular Sliding Contact," *Journal of Applied Mechanics*, **88**, pp. 371-378.

Hardy, C., Baronet, C. N., and Tordion, G. V., 1971, "The Elastoplastic Indentation of a Half-Space by a Rigid Sphere," *International Journal for Numerical Methods in Engineering*, **3**, pp. 451-462.

Herr, W., and Broszeit, E., 1997, "Effect of an Annealing Process on the Tribological Properties of Sputtered Hard Coatings," *Surface and Coatings Technology*, **97**, pp. 669-674.

Hertz, H., 1882, "On the Contact of Elastic Solids," Miscellaneous Papers by H. Hertz, Macmillan, London, UK.

Hills, D. A., and Ashelby, D. W., 1982, "The Influence of Residual Stresses on Contact-Load-Bearing Capacity," *Wear*, **75**, pp. 221-240.

Huber, M. T., 1904, “Zur Theorie der Beruhrung Fester elasticher Korper,” *Annalen der Physik*, **14**, pp. 153-163.

Jaeger, J. C., 1942, “Moving Sources of Heat and the Temperature at Sliding Contacts,” *Proceedings Royal Society of NS Wales*, **76**, pp. 203-224.

Johnson, K. L., 1985, *Contact Mechanics*, Cambridge University Press, Cambridge, UK.

Ju, F. D., and Liu, J. C., 1988, “Parameters Affecting Thermomechanical Cracking in Coated Media Due to High-Speed Friction Load,” ASME *Journal of Tribology*, **110**, pp. 222-227.

Ju, Y., and Farris, T. N., 1997, “FFT Thermoelastic Solutions for Moving Heat Sources,” ASME *Journal of Tribology*, **119**, pp. 156-162.

Kamiya, S., Sato, M., and Saka, M., 1999, “Residual Stress Distribution in the Direction of the Film Normal in Thin Diamond Films,” *Journal of Applied Physics*, **86**, pp. 224-229.

Kato, K., Bai, M., Umehara, N., and Miyake, Y., 1999, “Effect of Internal Stress of CNx coating on its Wear in Sliding Friction,” *Surface and Coatings Technology*, **113**, pp. 233-241.

Kennedy, F. E., 1981, “Surface Temperatures in Sliding Systems – A Finite Element Analysis,” *ASME Journal of Lubrication Technology*, **103**, pp. 90-96.

Kennedy, F. E., 1984, “Thermal and Thermomechanical Effects in Dry Sliding,” *Wear*, **100**, pp. 453-476.

Kennedy, F. E., and Ling, F. F., 1974a, “Elasto-Plastic Indentation of a Layered Medium,” ASME *Journal of Engineering Materials and Technology*, **96**, pp. 97-103.

Kennedy, F. E., and Ling, F. F., 1974b, “Thermal, Thermoelastic, and Wear Simulation of a High-Energy Sliding Contact Problem,” ASME *Journal of Lubrication Technology*, **96**, pp. 497-507.

King, R. B., 1987, “Elastic Analysis of Some Punch Problems for a Layered Medium,” *International Journal of Solids and Structures*, **23**, pp.1657-1664.

Komvopoulos, K., 1988, “Finite Element Analysis of a Layered Elastic Solid in Normal Contact With a Rigid Surface,” ASME *Journal of Tribology*, **110**, pp. 477-485.

Komvopoulos, K., 1989, “Elastic-Plastic Finite Element Analysis of Indented Layered Media,” ASME *Journal of Tribology*, **111**, pp. 430-439.

Komvopoulos, K., 2000, “Head-Disk Interface Contact Mechanics for Ultrahigh Density Magnetic Recording,” *Wear*, **238**, pp. 1-11.

Komvopoulos, K., and Ye, N., 2001, "Three-Dimensional Contact Analysis of Elastic-Plastic Layered Media With Fractal Surface Topographies," ASME *Journal of Tribology*, **123**, pp. 432-640.

Kral, E. R., and Komvopoulos, K., 1996, "Three-Dimensional Finite Element Analysis of Surface Deformation and Stresses in an Elastic-Plastic Layered Medium Subjected to Indentation and Sliding Contact Loading," ASME *Journal of Applied Mechanics*, **63**, pp. 365-375.

Kral, E. R., Komvopoulos, K., and Bogy, D. B., 1995, "Finite Element Analysis of Repeated Indentation of an Elastic-Plastic Layered Medium by a Rigid Sphere, Part II: Subsurface Results," ASME *Journal of Applied Mechanics*, **62**, pp. 29-42.

Kulkarni, S. M., Rubin, C. A., and Hahn, G. T., 1991, "Elastoplastic Coupled Temperature-Displacement Finite Element Analysis of 2-Dimensional Rolling-Sliding Contact With a Translating Heat Source," ASME *Journal of Tribology*, **113**, pp. 93-101.

Larsson, J., Biwa, S., and Storåkers, 1999, "Inelastic Flattening of rough Surfaces," *Mechanics of Materials*, **31**, pp. 29041.

Leroy, J. M., Floquet, A., and Villechaise, B., 1989, "Thermomechanical Behavior of Multilayered Media – Theory," ASME *Journal of Tribology*, **111**, pp. 538-544.

Leroy, J. M., Floquet, A., and Villechaise, B., 1990, "Thermomechanical Behavior of Multilayered Media – Results," ASME *Journal of Tribology*, **112**, pp. 317-323.

Lichinchi, M., Lenardi, C., Haupt, J., and Vitali, R., 1998, "Simulation of Berkovich nanoindentation experiments on thin films using finite element method," *Thin Solid Films*, **312**, pp. 240-248.

Ling, F. F., and Lai, W. M., 1980, "Surface Mechanics of Layered Media," *Solid Contact and Lubrication*, Cheng, H. S., and Keer, L. M., eds., AMD-**39**, ASME, New York, pp. 27-50.

Loubet, J. L., Georges, J. M., Marchesini, O., and Meille, G., 1984 "Vickers Indentation Curves of Magnesium Oxide (MgO)**,"** *ASME Journal of Tribology*, **106**, pp. 43-48.

Lu, W., and Komvopoulos, K., 2000, "Implanted Argon Atoms as Sensing Probes of Residual Stress in Ultrathin Films," *Applied Physics Letters*, **76**, pp. 3206-3208.

Machlin, E. S., 1995, *Materials Science in Microelectronics, The Relationships between Thin Film Processing and Structure*, Giro Press, Croton-on-Hudson, NY.

Majumdar, A., and Bhushan, B., 1991, "Fractal Model of Elastic-Plastic Contact Between Rough Surfaces," ASME *Journal of Tribology*, **113**, pp. 1-11.

Majumdar, A., and Tien, C. L., 1990, "Fractal Charactaerization and Simulation of rough Surfaces," *Wear*, **136**, pp. 313-327.

Mandelbrot, B. B., 1983, *The Fractal Geometry of Nature*, Freeman, New York.

Marsh, D. M., 1964, "Plastic Flow in Glass," *Proceedings of the Royal Society* (London), Series A, **279**, pp. 420-435.

Martinez, E., and Esteve, J., 2001, "Nanoindentation Hardness Measurements Using Real-Shape Indenters: Application to Extremely Hard and Elastic Materials," *Applied Physics A (Materials Science Processing)*, **A72**, pp. 319-324.

Martinez, H. P., and Abermann, R., 1982, "Interaction of O_2, CO, H_2O, H_2 and N_2 with thin chromium films studied by internal stress measurements**,"** *Thin Solid Films,* **89**, pp. 133-138.

Mehregany, M., Tong, L., Matus, L. G., and Larkin, D. J., 1997, "Internal Stress and Elastic Modulus Measurements on Micromachined 3C-SiC Thin Films," *IEEE Transactions on Electron Devices*, **44**, pp. 74-79.

Meijers, P., 1968, "The Contact Problem of a Rigid Cylinder on an Elastic Layer," *Applied Scientific Research*, **18**, pp. 353-383.

Mesarovic, S. Dj., and Fleck, N. A., 1999, "Spherical Indentation of Elastic-Plastic Solids," *Proceedings of the Royal Society* (London), Series A, **455**, pp. 2707-2728.

Mounier, E., Juliet, P., Quesnel, E., and Pauleau, Y., 1995, "Dependence of Tribological Properties on Deposition Parameters for Nonhydrogenated Amorphous Carbon Films Produced by Magnetron Sputtering," *Surface and Coating Technology*, **77**, pp. 548-552.

Mounier, E., and Pauleau, Y., 1997, "Mechanisms of Intrinsic Stress Generation in Amorphous Carbon Thin Films Prepared by Magnetron Sputtering," *Diamond and Related Materials*, **6**, pp. 1182-1191.

Nix, W. D., 1989, "Mechanical Properties of Thin Films," *Metallurgical Transactions A,* **20A**, pp. 1989-2217.

Oliver, W. C., and Pharr, G. M., 1992, "An Improved Technique for Determining Hardness and Elastic Modulus Using Load and Displacement Sensing Indentation Experiments," *Journal of Materials Research,* **7**, pp. 1564-1583.

Pao, Y. C., Wu, T.-S., and Chiu, Y. P., 1971, "Bounds on the Maximum Contact Stress of an Indented Elastic Layer," *ASME Journal of Applied Mechanics*, **38**, pp. 608-614.

Pelletier, H., Krier, J., Cornet, A., and Mille, P., 2000, "Limits of Using Bilinear Stress-Strain Curve for Finite Element Modeling of Nanoindentation Response on Bulk Materials," *Thin Solid Films*, **379**, pp. 147-155.

Pharr, G. M., 1998, "Measurement of mechanical properties by ultra-low load indentation," *Materials Science & Engineering A (Structural Materials: Properties, Microstructure and Processing)*, **A253**, pp. 151-159.

Pulker, H. K., 1982, “Mechanical properties of optical films,” *Thin Solid Films*, **89**, pp. 191- 204.

Russ, J. C., *Fractal Surfaces*, Plenum Press, New York, 1994, p. 168.

Sackfield, A., and Hills, D. A., 1983, “A Note on the Hertz Contact Problem – A Correlation of Standard Formulas,” *Journal of Strain Analysis for Engineering Design*, **18**, pp. 195-197.

Scharf, T. W., and Barnard, J. A., 1997, “Nanotribology of Ultranthin a:SiC/SiC-N overcoats using a depth sensing nanoindentation multiple sliding technique,” *Thin Solid Films*, **308-309**, pp. 340-344.

Sneddon, I. N., 1965, “The Relation Between Load and Penetration in the Axisymmetric Boussinesq Problem for a Punch of Arbitrary Profile,” *International Journal of Engineering Science*, **3**, pp. 47-57.

Tabor, D., 1970, “The Hardness of Solids,” *Review of Physics in Technology*, **1**, pp. 145-179.

Tian, H., and Saka, N., 1991, “Finite Element Analysis of an Elastic-Plastic Two-Layer Half-Space: Normal Contact,” *Wear*, **148**, pp. 47-68.

Tian, X., and Kennedy, F. E., 1993, “Temperature Rise at the Sliding Contact Interface for a Coated Semiinfinite Body,” ASME *Journal of Tribology*, **115**, pp. 1-9.

Tian, X. F., and Kennedy, F. E., 1994, “Maximum and Average Flash Temperatures in Sliding Contacts,” ASME *Journal of Tribology*, **116**, pp. 167-174.

Van der Zwaag, S., and Field, J. E., 1982, “The Effect of Thin hard Coatings on the Hertzian Stress Field,” *Philosophical Magazine A*, **46**, pp. 133-150.

Vick, B., Golan, L. P., and Furey, M. J., 1994, “Thermal Effects Due to Surface Films in Sliding Contact,” ASME *Journal of Tribology*, **116**, pp. 238-245.

Wang, S. and Komvopoulos, K., 1994a, “A Fractal Theory of the Interfacial Temperature Distribution in the Slow Sliding Regime: Part I — Elastic Contact and Heat Transfer Analysis,” ASME *Journal of Tribology*, **116**, pp. 812-823.

Wang, S. and Komvopoulos, K., 1994b, “A Fractal Theory of the Interfacial Temperature Distribution in the Slow Sliding Regime: Part II — Multiple Domains, Elastoplastic Contacts and Applications,” ASME *Journal of Tribology*, **116**, pp. 824-832.

Wang, S. and Komvopoulos, K., 1995, “A Fractal Theory of the Temperature Distribution at Elastic Contacts of Fast Sliding Surfaces,” ASME *Journal of Tribology*, **116**, pp. 824-832.

Yan, W., and Komvopoulos, K., 1998, “Contact Analysis of Elastic-Plastic Fractal Surfaces,” *Journal of Applied Physics*, **84**, pp. 3617-3624.

Yu, C.-C., and Heinrich, J. C., 1986, “Petrov-Galerkin Methods for the Time-Dependent Convective Transport Equation,” *International Journal for Numerical Methods in Engineering*, **23**, pp. 883-901.

Zhong, D., Sutter, E., Moore, J. J., Mustoe, G. G. W., Levashov, E. A., and Disam, J., 2001, “Mechanical Properties of Ti-B-C-N Coatings Deposited by Magnetron Sputtering,” *Thin Solid Films*, **398-399**, pp. 320-325.